Study of Low Energy Electron Anti-neutrinos at Super-Kamiokande IV

Dissertation Submitted to

Tsinghua University

in partial fulfillment of the requirement

for the degree of

Doctor of Philosophy

in

Physics

by

ZHANG Haibing

Dissertation Supervisor: Professor CHEN Shaomin

May 2012

Abstract

Detecting thermal neutrons produced in the inverse beta decay reaction is of importance in the study of low energy neutrino physics. A forced trigger scheme has been implemented in Super-Kamiokande IV to search for the 2.2 MeV γ resulting from neutron captures on free protons. A comprehensive study of neutron tagging in pure water is presented for the first time. The neutron tagging efficiency is found to be $(19.3 \pm 1.0)\%$, which is well verified with an Am/Be source. The accidental background probability evaluated from real data is $(1.0 \pm 0.1)\%$ per 500 μs of data.

Neutron tagging method is applied to identify the low energy $\bar{\nu}_e$ via a coincident detection of the prompt e^+ and the delayed 2.2 MeV γ. We employ this new technique to search for two $\bar{\nu}_e$ signals of extraterrestrial origin: the supernova relic neutrino and possible $\bar{\nu}_e$ from the Sun.

No events are found for both signals in 960 days of Super-Kamiokande IV data. The 90% CL upper limits on the total flux are set. For the supernova relic neutrinos, the flux upper limit is ~ 6 times the model prediction. And for the solar $\bar{\nu}_e$, the flux upper limit is 4.5×10^{-4} of the total ^{8}B ν_e flux.

Model independent upper limits are also presented for $\bar{\nu}_e$ flux with 1 MeV energy bins. In the energy range 13.3 MeV $< E_{\bar{\nu}_e} <$21.3 MeV, the obtained limits are currently world's best.

In addition, we have successfully observed clear neutron capture signals in the atmospheric neutrino data. Implication of improving proton decay search sensitivity by rejecting atmoshperic neutrino backgrounds via neutron tagging is also discussed.

Contents

List of Figures

List of Tables

List of Abbreviations

AFT	After Trigger
DAQ	Data Acquisition
DSNB	Diffuse Supernova Neutrino Background
FC	Fully Contained
FV	Fiducial Volume
HE	High Energy
IBD	Inverse Beta Decay
ID	Inner Detector
LE	Low Energy
MC	Monte Carlo
OD	Outer Detector
PMT	Photomultiplier Tube
SFP	Spin-Flavor Precession
SHE	Special High Energy
SK or Super-K	Super-Kamiokande
SLE	Super-Low Energy
SRN	Supernova Relic Neutrino
SSM	Standard Solar Model
TOF	Time of Flight

Acknowledgements

This dissertation would never have been possible without many people's support and assistance, both personally and professionally. First, I would like to thank my advisor, Shaomin Chen. He introduced me into the exciting field of neutrino physics and offered me the opportunity to work at the Super-Kamiokande experiment. He has always been supportive and understanding during the entire course of my graduate study. In many ways he is also a very good friend, too. I believe he is simply the nicest supervisor one can ask for.

I'm grateful to many of the Super-Kamiokande collaborators. I have learned a lot on both physics and the Super-Kamiokande experiment from Masayuki Nakahata. As the convener of the low-energy group, Nakahata-sensei's capable and insightful leadership has ensured the team to operate efficiently and consistently. I benefited greatly from discussions with Michael Smy, Mark Vagins, Masato Shiozawa, John Learned, Yusuke Koshio and Yasuo Takeuchi. Special appreciation goes to Henry Sobel, the impact of whose invaluable support and encouragement to me can never be overestimated. Part of the data analysis is done with interactions with Kirk Bays, who explained to me many of the cuts in great detail via numerous emails.

Living in another country is difficult for me. Luckily, there have been many nice people in Kamioka and they made my life much easier in Japan. I appreciate the assistance of the Kamioka Observatory stuff. I enjoyed the company of the students Motoyasu Ikeda, Takashi Iida, Takaaki Yokozawa, Koh Ueno, Patrick de Periom, and Koun Choi. In particular, I would like to thank Roger Wendell. He is the one I had the most conversations with when I stayed in Kamioka.

Back at Tsinghua, I would like to thank Yuanning Gao for teaching me particle physics. I always fell lucky to have met Yang Heng, who was Shaomin's Master student during my second to fourth year of graduate. We traveled together, worked together and had many stimulating late night talks. He is the best friend and colleague one can ever expect and I wish we could work together again someday.

Finally, I would like to offer my gratitude to my family. I could never have reached this far without their support, caring and love.

Chapter 1

Introduction

Water Cherenkov detectors, such as Kamiokande, IMB and most noticeably Super-Kamiokande (SK), have led to numerous scientific contributions, e.g. discovery of neutrinos from the core-collapse supernova [1, 2], discovery of neutrino mass by oscillation of atmospheric neutrinos [3], determination of solar neutrino mixing parameters [4] and best limits on proton decay [5]. Through these achievements, water Cherenkov detectors have proven to be one of the very effective neutrino and nucleon decay detectors. It has been realized that the scientific capability of SK can be enhanced if neutrons can be observed as well. For instance, a delayed-coincidence detection of positron and neutron capture may allow an identification of low energy anti-neutrinos via the inverse beta decay (IBD) reaction chain

$$\begin{aligned} \bar{\nu}_e + p &\rightarrow e^+ + n, \\ n + p &\rightarrow d + \gamma\,(2.2\ \mathrm{MeV}), \end{aligned} \tag{1.1}$$

where the positron will be detected immediately and is referred to as the primary event, while the neutron will be thermalized and eventually be captured on protons, releasing a 2.2 MeV γ after ~200 μs average time, and is therefore referred to as the delayed event. In addition, the sensitivity of proton decay searches can be improved by reducing potential atmospheric neutrino backgrounds accompanied by neutrons.

In this thesis, we comprehensively study for the first time neutron tagging in a large water Cherenkov detector by searching for a 2.2 MeV γ and explore new physics opportunities facilitated by this new technique. The primary focus of this thesis is to search for $\bar{\nu}_e$'s from extraterrestrial sources. Candidates include the long-sought-after supernova relic neutrinos (SRN), which is also known as the diffuse supernova neutrino background (DSNB), and possible solar $\bar{\nu}_e$'s resulting from some exotic generation mechanisms. An implication on background rejection for proton decay searches is also discussed. In this chapter, a brief review is given for general neutrino properties, the physics of SRN and solar $\bar{\nu}_e$, as well as the previous experimental results.

1.1 Neutrino Properties

Neutrinos are electrically neutral particles of spin 1/2. There are at least three generations of light neutrinos, ν_e, ν_μ and ν_τ, corresponding to the leptons, e, μ, and τ. The interactions of neutrinos are well described by the standard electroweak theory based on the $SU(2)_L \times U(1)_Y$ gauge model. One of the peculiarities for neutrinos is that weak interactions couple only to left-handed [1] neutrinos, or to right-handed anti-neutrinos. The charged weak current that couples a ν_e to an electron has the $V - A$ form

$$j^\mu_{\text{weak}} \propto \overline{\nu_e}\gamma^\mu(1-\gamma^5)e = 2\overline{\nu_{eL}}\gamma^\mu e_L, \tag{1.2}$$

where the presence of $1-\gamma^5$ projects out the left chirality component of ν_e. The right chirality component ν_R either does not exist (as in the Standard Model) or interacts extremely weakly, i.e. sterile. The lepton flavor is conserved in the weak interactions. A neutrino of flavor $\alpha(\alpha = e, \mu, \tau)$, ν_α, always couple to a charged lepton l with the same flavor, l_α.

An open question regarding the nature of neutrinos is whether they are Dirac or Majorana particles. To put it in another way, are neutrinos their own antiparticles? The massive Dirac field consists of two independent Weyl fields: a left-handed component ψ_L and a right-handed one ψ_R. In case of the Majorana field, the right-handed component is just a particle-antiparticle conjugation [2] of the left-handed one,

$$\psi_R = (\psi_L)^c \equiv C\overline{\psi_L}^{\mathrm{T}}, \tag{1.3}$$

where C is the particle-antiparticle conjugation matrix, $C = i\gamma_2\gamma_0$. Evidently, a Majorana field satisfies

$$\psi = \psi_L + \psi_R = \psi_L + (\psi_L)^c = \psi^c, \tag{1.4}$$

---

[1] Here it does not mean helicity -1 but rather left chirality. Only at the massless limit, chirality and helicity coincides. It's customary to call the left chirality component of a field left-handed. For massive neutrinos, the chirality is not a conserved quantum quantity. A neutrino created with left chirality can develop a small fraction of right chirality component of the order m_ν/E_ν [6].

[2] A more common term encountered in the literature is the charge conjugation. But it's pointed out in Ref. [6] that charge conjugation, by definition, would turn a left-handed neutrino into a left-handed anti-neutrino, which does not exist.

which means that Majorana particles are their own antiparticles. Distinction between neutrinos and anti-neutrinos was first established in Davis's radiochemical experiment. The experiment found that the reaction $\bar{\nu}_e + {}^{37}\mathrm{Cl} \to {}^{37}\mathrm{Ar} + e^-$ did not occur while $\nu_e + {}^{37}\mathrm{Cl} \to {}^{37}\mathrm{Ar} + e^-$ did. However, this does not disprove the Majorana nature of neutrinos. Because in this experiment the anti-neutrinos coming from reactors are dominantly right-handed, while standard weak interactions require left-handed neutrinos for the process $\nu_e + {}^{37}\mathrm{Cl} \to {}^{37}\mathrm{Ar} + e^-$ to occur. It should be noted that the Dirac and Majorana description of neutrinos can have different phenomenological consequences only if neutrinos are massive. Because in the massless limit, ψ_L and ψ_R are decoupled and ψ_L in both descriptions obeys the Weyl equation while ψ_R has no weak interactions. The most promising way to find out if neutrinos are Majorana particles is to search for neutrinoless double beta ($0\nu\beta\beta$) decay, the rate of which is proportional to neutrino masses. If the $0\nu\beta\beta$ decay is observed, no matter what diagrams are responsible, it will imply neutrinos are Majorana particles.

1.1.1 Neutrino Masses and Mixings

Neutrinos are massless in the Standard Model (SM). Experimentally, up to now all direct measurements of the neutrino mass give negative results. The absolute mass of the electron neutrino can be measured by observing β decays. The best limit on electron neutrino mass, obtained by measuring the end-point of the electron spectrum in Tritium decay, is [7]

$$m_{\nu_e} < 2.3\,\mathrm{eV} \quad (95\%\ \mathrm{CL}). \tag{1.5}$$

The mass of the muon neutrino can be determined from momentum analysis of pion decay $\pi^+ \to \mu^+\nu_\mu$. The mass of tau neutrino is derived by fitting the visible energy vs invariant mass in tau decays $\tau^- \to 2\pi^- + \pi^+ + \nu_\tau$ and $\tau^- \to 3\pi^- + 2\pi^+ + \nu_\tau(+\pi_0)$. The upper limit on the masses of ν_μ [8] and ν_τ [9] are

$$m_{\nu_\mu} < 0.17\,\mathrm{MeV} \quad (90\%\ \mathrm{CL}), \tag{1.6}$$

$$m_{\nu_\tau} < 18.2\,\mathrm{MeV} \quad (95\%\ \mathrm{CL}). \tag{1.7}$$

Massive neutrinos play an important role in the evolution of the universe and consequently constrains on absolute neutrino masses can be derived from cosmology. A latest analysis [10] of WMAP and SDSS data yields the limit on the sum of neutrino masses:

$$\sum m_\nu < 0.44\,\mathrm{eV} \quad (95\%\ \mathrm{CL}). \tag{1.8}$$

However, there are compelling evidences from neutrino oscillation experiments that neutrinos have tiny but nonzero masses. How could the nonzero neutrino mass be accommodated in particle theories? We shall briefly examine this issue in the context of the Standard Model and some simplest extensions. For more thorough discussions, we defer to the literatures, see e.g. Refs. [11, 12, 13]. In the Standard Model, neutrinos can not have Dirac masses as other fermions do because of the absence of right-handed neutrinos ν_R. Neutrinos can not have Majorana masses involving only left-handed neutrinos ν_L, either. Because the Majorana mass term is of the form

$$-\mathcal{L}^{\mathrm{M}} = \frac{1}{2} m \nu_L^T C \nu_L + \text{h.c.}, \tag{1.9}$$

which has $I_3 = 1$ and $Y = -2$. But the SM does not have any weak isospin triplet Higgs field with $Y = 2$, so there is no way to construct a renormalizable Lagrangian which can generate a Majorana mass. It is possible, however, to construct a composite Higgs operator out of two Higgs doublets that has the correct quantum number. The Majorana neutrino mass can be generated from the lepton number violating term

$$-\mathcal{L}_5 = \frac{g}{\mathcal{M}} (L_L^T \tau_2 \phi) C (\phi^T \tau_2 L_L) + \text{h.c.}, \tag{1.10}$$

where g is a dimensionless coupling, $\mathcal{M}$ is a constant with dimension of mass, $L_L = (\nu_L, l_L)^{\mathrm{T}}$ is the lepton $SU(2)_L$ doublet, ϕ is the Higgs doublet and τ_2 is the second Pauli matrix. After symmetry breaking, $\mathcal{L}_5$ generates the mass term

$$-\mathcal{L}^{\mathrm{M}} = \frac{1}{2} \frac{g v^2}{\mathcal{M}} \nu_L^T C \nu_L + \text{h.c.}, \tag{1.11}$$

where v is the vacuum expectation value of the Higgs field. From this expression one can readily identify the Majorana mass

$$m = \frac{g v^2}{\mathcal{M}}. \tag{1.12}$$

Although $\mathcal{L}_5$ respects SM symmetries, it's not acceptable in the SM because it contains dimension five operators, which is not renormalizable. However, such nonrenormalizable operators could be some manifestation of new physics at a high energy scale characterized by $\mathcal{M}$, which is analogous to the effective nonrenormalizable Fermi theory of weak interactions. From Eqn. (1.12), it is clear that m could be made small if $\mathcal{M}$ is large.

Alternatively, one can extend the Standard Model by adding right-handed neutrinos ν_R. In principle, there is nothing prevents the existence of ν_R, which is a $SU(2)_L$ singlet and has hypercharge $Y = 0$. In this case, neutrinos can have Dirac masses through the same Higgs mechanism that generates masses for chargecd fermions. In this scenario, however, there is no explanation of the smallness of mass for neutrinos compared to that for charged leptons and quarks. Note that Majorana mass term involves only ν_R is also allowed by the symmetries of the SM. So the general mass term for one generation, in the framework of the SM with the addition of ν_R, can be written as

$$\begin{aligned} -\mathcal{L}^{\mathrm{D+M}} &= m_D \overline{\nu_R} \nu_L + \frac{1}{2} m_R \nu_R^T C \nu_R + \text{h.c.} \\ &= \frac{1}{2} N_L^T C M N_L + \text{h.c.}, \end{aligned} \tag{1.13}$$

where $N_L = (\nu_L, (\nu_R)^c)^{\mathrm{T}}$ is a column of left-handed chiral fields and M is the mass matrix

$$M = \begin{pmatrix} 0 & m_D \\ m_D & m_R \end{pmatrix} \tag{1.14}$$

Diagonalization of (1.13), in the limit $m_D \ll m_R$, gives the mass eigenvalues

$$m_1 \simeq \frac{m_D^2}{m_R}, \quad m_2 \simeq m_R, \tag{1.15}$$

for mass eigenstates ν_1 and ν_2, which are Majorana neutrinos. Interestingly, ν_1 is very light, provided that $m_D \ll m_R$. It is ν_R being heavy that makes ν_1 light. This is the famous *see-saw* mechanism that provides a very plausible explanation for the smallness of the neutrino mass [14]. Note that m_1 has the same structure as the Majorana mass (1.12) obtained with the effective Lagrangian $\mathcal{L}_5$, if m_R is identified as the high-energ mass scale $\mathcal{M}$. This is not a surprise, since it is generally believed that the small neutrino mass is connected to new physics at a high energy scale. Therefore, neutrino mass is particularly important in particle physics.

Neutrino Oscillation in Vacuum

Neutrinos being massive means that there exists a spectrum of neutrino mass eigenstates ν_i, each with mass $m_i (i = 1, 2, 3)$. The flavor state $\nu_\alpha (\alpha = e, \nu, \tau)$ can be expressed as a superposition of mass eigenstates,

$$|\nu_\alpha\rangle = \sum_i U_{\alpha i}^* |\nu_i\rangle, \tag{1.16}$$

where U is the neutrino mixing matrix. If U is not diagonal, ν_α is a mixture of ν_i. As a neutrino of flavor α at creation propagates, different mass components evolve differently, leading to an observable effect known as neutrino oscillation, i.e. the probability of finding ν_α in the original state (or any other flavor state) oscillates with time.

The massive neutrino states ν_i are eigenstates of the free Hamiltonian and the time evolution is simply

$$|\nu_i(t)\rangle = e^{-iE_i t}|\nu_i\rangle. \tag{1.17}$$

From Eqn. (1.16), the time evolution of the flavor state ν_α is then

$$|\nu_\alpha(t)\rangle = \sum_i U^*_{\alpha i} e^{-iE_i t}|\nu_i\rangle \tag{1.18}$$

The amplitude of finding the neutrino at the time t in a flavor state ν_β is

$$\begin{aligned} A_{\nu_\alpha \to \nu_\beta}(t) = \langle \nu_\beta | \nu_\alpha(t)\rangle &= \sum_i U^*_{\alpha i} e^{-iE_i t}\langle \nu_\beta|\nu_i\rangle \\ &= \sum_i \sum_j U^*_{\alpha i} U_{\beta j} e^{-iE_i t}\langle \nu_j|\nu_i\rangle \\ &= \sum_i U^*_{\alpha i} U_{\beta i} e^{-iE_i t}. \end{aligned} \tag{1.19}$$

The transition probability is given by

$$P_{\nu_\alpha \to \nu_\beta}(t) = \left|A_{\nu_\alpha \to \nu_\beta}(t)\right|^2 = \sum_i \sum_j U^*_{\alpha i} U_{\beta i} U_{\alpha j} U^*_{\beta j} e^{-i(E_i - E_j)t}. \tag{1.20}$$

For relativistic neutrinos, $E_i = \sqrt{p^2 + m_i^2} \simeq p + m_i^2/2p \simeq p + m_i^2/2E$. Thus, the transition probability can be approximated by

$$P_{\nu_\alpha \to \nu_\beta}(t) = \sum_i \sum_j U^*_{\alpha i} U_{\beta i} U_{\alpha j} U^*_{\beta j} e^{-i\frac{\Delta m^2_{ij}}{2E}t}, \tag{1.21}$$

where $\Delta m^2_{ij} = m_i^2 - m_j^2$. In neutrino oscillation experiments, the measured quantity is usually the distance L travelled by neutrinos instead of the time

t. For relativistic neutrinos, $t \simeq L$, and one finds [3]

$$\begin{aligned} P_{\nu_\alpha \to \nu_\beta}(L) &= \sum_i \sum_j U^*_{\alpha i} U_{\beta i} U_{\alpha j} U^*_{\beta j} \exp\left(-i \frac{\Delta m^2_{ij} L}{2E}\right) \\ &= \delta_{\alpha\beta} - 4 \sum_{i>j} \mathrm{Re}(U^*_{\alpha i} U_{\beta i} U_{\alpha j} U^*_{\beta j}) \sin^2\left(\frac{\Delta m^2_{ij} L}{4E}\right) \\ &\quad + 2 \sum_{i>j} \mathrm{Im}(U^*_{\alpha i} U_{\beta i} U_{\alpha j} U^*_{\beta j}) \sin\left(\frac{\Delta m^2_{ij} L}{2E}\right). \end{aligned} \tag{1.22}$$

To simplify the discussion, we shall consider a special case of two flavor oscillation $\nu_e \to \nu_\mu$. The two-neutrino description is an adequate approximation in treating data from a number of neutrino oscillation experiments. In this case, there is only one squared-mass difference $\Delta m^2 = m_2^2 - m_1^2$ and the mixing matrix U takes the form

$$U = \begin{pmatrix} \cos\theta & \sin\theta \\ -\sin\theta & \cos\theta \end{pmatrix}. \tag{1.23}$$

From Eqn. (1.22), it follows that the transition probability of $\nu_e \to \nu_\mu$ is simply

$$\begin{aligned} P_{\nu_e \to \nu_\mu} &= \sin^2 2\theta \, \sin^2\left(\frac{\Delta m^2 L}{4E}\right) \\ &= \sin^2 2\theta \, \sin^2\left(1.27 \frac{\Delta m^2(\mathrm{eV}^2) L(\mathrm{m})}{E(\mathrm{MeV})}\right). \end{aligned} \tag{1.24}$$

It is clear from (1.24) that the neutrino oscillation can take place only if both the mass spliting Δm^2 and the mixing angle θ are nonzero. Indeed, it is the observation of neutrino oscillation that leads to the conclusion that neutrinos are massive and they mix.

Neutrino Oscillation in Matter

When propagating through matter, neutrinos acquire extra interaction potential energy due to the coherent forward scattering [15], which can significantly modify their propagation [16]. This is the famous MSW effect. For

---

[3] This derivation is done in the plane-wave approximation, which may raise some theoretical concerns. For example, applying energy-momentum conservation will lead to the conclusion that neutrino oscillation can not happen at all. However, it can be shown , in the framework of quantum field theory, such inconsistency can be reconciled and the transition probability (1.22) is correct [13].

neutral unpolarized medium, the effective potentials are given by

$$V_e = V_{\mathrm{CC}} + V_{\mathrm{NC}}, \qquad V_\mu = V_\tau = V_{\mathrm{NC}}, \tag{1.25}$$

with the charged-current and neutral-current potentials,

$$V_{\mathrm{CC}} = \sqrt{2} G_F N_e, \qquad V_{\mathrm{NC}} = -\frac{\sqrt{2}}{2} G_F N_n, \tag{1.26}$$

where N_e and N_n are the number densities of electron and neutron, respectively. For anti-neutrinos, the matter potentials change sign.

In vacuum, the time-evolution equation in the mass eigenstate basis is

$$i\frac{d}{dt}\begin{pmatrix} \nu_1 \\ \nu_2 \end{pmatrix} = \begin{pmatrix} E_1 & 0 \\ 0 & E_2 \end{pmatrix}\begin{pmatrix} \nu_1 \\ \nu_2 \end{pmatrix}. \tag{1.27}$$

This gives the evolution equation in flavor basis

$$\begin{aligned} i\frac{d}{dt}\begin{pmatrix} \nu_e \\ \nu_\mu \end{pmatrix} &= U \begin{pmatrix} E_1 & \\ & E_2 \end{pmatrix} U^\dagger \begin{pmatrix} \nu_e \\ \nu_\mu \end{pmatrix} & (1.28) \\ &= \begin{pmatrix} -\frac{\Delta m^2}{4E}\cos 2\theta & \frac{\Delta m^2}{4E}\sin 2\theta \\ \frac{\Delta m^2}{4E}\sin 2\theta & \frac{\Delta m^2}{4E}\cos 2\theta \end{pmatrix}\begin{pmatrix} \nu_e \\ \nu_\mu \end{pmatrix}, & (1.29) \end{aligned}$$

where a common diagonal element is omitted since it modifies the common phase of the neutrino states and hence has no effect on neutrino oscillations. To derive the neutrino evolution equation in matter, one has to add the matter-induced potentials to the diagonal elements of the Hamiltonian in Eqn. (1.29). Neglecting again a common term due to NC interactions, the neutrino evolution equation in matter is given by

$$i\frac{d}{dt}\begin{pmatrix} \nu_e \\ \nu_\mu \end{pmatrix} = \begin{pmatrix} -\frac{\Delta m^2}{4E}\cos 2\theta + \sqrt{2} G_F N_e & \frac{\Delta m^2}{4E}\sin 2\theta \\ \frac{\Delta m^2}{4E}\sin 2\theta & \frac{\Delta m^2}{4E}\cos 2\theta \end{pmatrix}\begin{pmatrix} \nu_e \\ \nu_\mu \end{pmatrix}. \tag{1.30}$$

In general, N_e varies along the neutrino trajectory and the evolution equation (1.30) must be solved numerically. We shall consider a simple case where matter density is constant. The Hamiltonian in Eqn. (1.30) can be diagonalized by the mixing matrix

$$U_{\mathrm{M}} = \begin{pmatrix} \cos\theta_{\mathrm{M}} & \sin\theta_{\mathrm{M}} \\ -\sin\theta_{\mathrm{M}} & \cos\theta_{\mathrm{M}} \end{pmatrix}, \tag{1.31}$$

with θ_{M} given by

$$\tan 2\theta_{\mathrm{M}} = \frac{\frac{\Delta m^2}{2E}\sin 2\theta}{\frac{\Delta m^2}{2E}\cos 2\theta - \sqrt{2} G_F N_e}. \tag{1.32}$$

The effective squared-mass difference in matter is

$$\Delta m^2_{\mathrm{M}} = \sqrt{(\Delta m^2 \cos 2\theta - 2\sqrt{2}EG_F N_e)^2 + (\Delta m^2 \sin 2\theta)^2}. \tag{1.33}$$

In analogy to the vacuum case, the oscillation probability of $\nu_e \to \nu_\mu$ is given by

$$P_{\nu_e \to \nu_\mu} = \sin^2 2\theta_{\mathrm{M}} \sin^2 \left(\frac{\Delta m^2_{\mathrm{M}} L}{4E} \right) \tag{1.34}$$

From Eqn. (1.32), one can see the most striking characteristic of matter effect is that there is a resonance when

$$\sqrt{2}G_F N_e = \frac{\Delta m^2}{2E} \cos 2\theta. \tag{1.35}$$

When the MSW condition (1.35) is satisfied, mixing in matter is maximal ($\theta_{\mathrm{M}} = 45°$) even if the vacuum mixing angle θ is small. The matter enhanced neutrino oscillation plays a crucial role in solving the solar neutrino problem that will be discussed in section 1.3. Note that once the mixing angle is fixed, the MSW effect is sensitive to the sign of Δm^2. In the context of full three flavor oscillations, this feature can be employed to solve the long-standing neutrino mass hierarchy problem, i.e. whether m_3 is heavier than m_1 or not, provided that the mixing angle θ_{13} is nonzero.

What We Have Learned from Neutrino Oscillations?

Assuming three generations of Dirac neutrinos, the mixing matrix U can be parameterized by three mixing angles θ_{12}, θ_{23} and θ_{13} and one possible CP-violating phase δ. In case of Majorana neutrinos, there are two additional Majorana phases, which have no significance in neutrino oscillation experiments. As seen from the previous discussions, neutrino oscillations are only sensitive to the difference of mass squared. It is conventional to define two independent mass splittings $\Delta m^2_{21} = m^2_2 - m^2_1$ and $\Delta m^2_{31} = m^2_3 - m^2_1$ in neutrino oscillation analysises. Many experiments have been devoted to measure the neutrino mixing parameters and mass differences. Recent global analysises [17, 18] of existing neutrino oscillation data imply

$$\begin{aligned}
\Delta m^2_{21} &\simeq 7.6 \times 10^{-5}\mathrm{eV}^2, && (1.36)\\
\sin^2\theta_{12} &\simeq 0.31, && (1.37)\\
|\Delta m^2_{31}| &\simeq 2.4 \times 10^{-3}\mathrm{eV}^2, && (1.38)\\
\sin^2\theta_{23} &\simeq 0.5. && (1.39)
\end{aligned}$$

These parameters have been determined with fairly good accuracy (for Δm^2_{31}, only the absolute value is known). The small mixing angle θ_{13} is now a focus of neutrino physics research. In 2011, the T2K, MINOS and Double Chooz collaborations announced indications of nonzero θ_{13} [19, 20, 21]. Very recently, a conclusive result has been released by the Daya Bay collaboration [22], which finds

$$\sin^2 2\theta_{13} = 0.092 \pm 0.016 \pm 0.005. \tag{1.40}$$

From an experimental point of view, a nonzero θ_{13} is very important because it opens up the possibility to search CP violations in the lepton sector and to determine the neutrino mass hierarchy (the one with $\Delta m^2_{31} > 0$ is called normal hierarchy, otherwise inverted hierarchy) exploiting matter effects.

1.1.2 Neutrino Magnetic Moments

Neutrinos do not have electric charge, but they may have dipole magnetic moments arising from quantum loops (see Fig. 1.1). In the Standard Model, similar quantum effects contribute to the anomalous magnetic moment of a charged fermion. Dirac and Majorana neutrinos exhibit distinctive electromagnetic properties. A massive Dirac neutrino will in general have a magnetic moment. On the other hand, based on general grounds such as CPT invariance, the magnetic moment of a Majorana neutrino vanishes [11, 23]. However, Majorana neutrinos can have nonzero transition magnetic moments between different flavors which can induce an anti-neutrino flux from the Sun (see section 1.3.2).

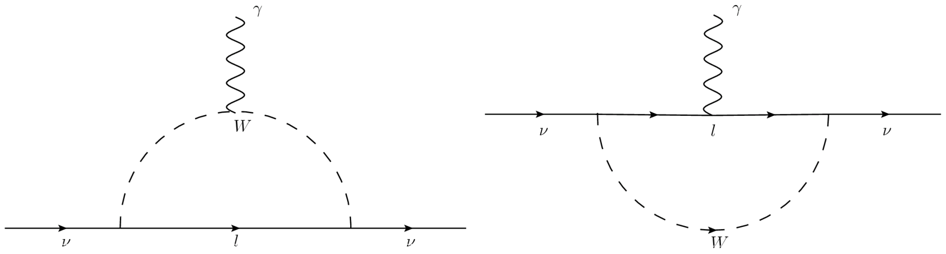

Figure 1.1: One-loop radiative contribution to the magnetic moment of a Dirac neutrino.

Consider first Dirac neutrinos in a minimal extension of the Standard Model with the introduction of right-handed neutrinos, one-loop Feynman diagrams contributing to the neutrino magnetic moments yield [24, 11, 25]

$$\mu^D_{ij} = \frac{eG_F}{8\sqrt{2}\pi^2}(m_i + m_j)\sum_l f(a_l)U_{lj}U^*_{li}, \tag{1.41}$$

where $m_i (i = 1, 2, 3)$ is the neutrino mass, U is the neutrino mixing matrix and

$$f(a_l) \approx \frac{3}{2}\left(1 - \frac{1}{2}a_l\right), \tag{1.42}$$

with $a_l = m_l^2/m_W^2 (l = e, \mu, \tau)$. From Eqn. (1.41), the diagonal magnetic moment of Dirac neutrinos, at the leading order in a_l, are given by

$$\mu_{ii}^D = \frac{3eG_F m_i}{8\sqrt{2}\pi^2} \approx 3.2 \times 10^{-19} \left(\frac{m_i}{1\mathrm{eV}}\right) \mu_B, \tag{1.43}$$

where the unitarity of the mixing matrix U is used. For $i \neq j$, the leading term of $f(a_l)$ sums up to zero. Therefore, the transition moments come only from the next leading order of $f(a_l)$ and thus are suppressed by a factor of $a_l = m_l^2/m_W^2$ with respect to diagonal moments.

For Majorana neutrinos, additional Feynman diagrams should be considered [26, 11]. As mentioned above, the diagonal magnetic moments of Majorana neutrinos vanish identically, $\mu_{ii}^M = 0$. The transition magnetic moments, at the one-loop level, is given by [12](see also [26, 11]),

$$\mu_{ij}^M = \frac{3eG_F}{16\sqrt{2}\pi^2}(m_i + m_j) \sum_l i\mathrm{Im}\,(a_l U_{lj} U_{li}^*), \tag{1.44}$$

The interpretation of Eqn. (1.44) simplifies if CP invariance is assumed. If the relative CP ν_i and ν_j is even, $U_{lj}U_{li}^*$ is real and thus μ_{ij}^M vanishes. On the other hand, if the relative CP is odd, $U_{lj}U_{li}^*$ is pure imaginary and μ_{ij}^M is antisymmetric, i.e. $\mu_{ji}^M = -\mu_{ij}^M$.

The neutrino magnetic moment derived within the Standard Model is proportional to the neutrino mass, which is known to be very small and thus imposes natural suppression on the magnitude of the neutrino magnetic moment. Beyond the Standard Model, it is possible to construct larger neutrino magnetic moment. For example, in the left-right symmetric model with right-handed neutrino interactions, the neutrino magnetic moment is proportional to the lepton mass instead of the neutrino mass, resulting in a much larger magnetic moment [27, 28, 29]. In another model which introduces a $SU(2)_L$–singlet charged scalar particle, the magnetic moment for Dirac neutrinos can be as large as $\mu_\nu \simeq 10^{-10}\mu_B$ [30]. More discussions on models beyond the Standard Model that generate large neutrino magnetic moments can be found in Refs. [11, 12]. On the other hand, model-independent considerations place strong limit on the magnetic moments of Dirac neutrinos ($\mu_\nu^D \lesssim 10^{-15}\mu_B$) while the bounds on magnetic moments of Majorana neutrinos are weaker than present experimental limit [31]. In view of the large variety of predictions, we shall keep an open mind regarding the magnitude of the magnetic moments of neutrinos.

The electromagnetic properties of neutrinos can be studied by direct laboratory measurements. For example, neutrino magnetic moments can manifest themselves through the additional contribution to the ν–e scattering cross section:

$$\left(\frac{d\sigma}{dT}\right)_{\text{EM}} = \frac{\pi\alpha^2}{m_e^2}\left(\frac{1}{T}-\frac{1}{E_\nu}\right)\left(\frac{\mu_\nu}{\mu_B}\right)^2, \tag{1.45}$$

where E_ν is the incident neutrino energy and T is the electron recoil energy; in case of long baseline experiments (e.g. solar), the observable μ_ν is the effective value including mixing effects [32]. Many searches have been conducted to look for distortion of the recoil electron spectrum in solar, reactor and accelerator neutrino data. The current best limit obtained is by the GEMMA experiment and is [33],

$$\mu_\nu < 3.2 \times 10^{-11}\mu_B \quad (90\%\ \text{CL}). \tag{1.46}$$

Constrains on the neutrino magnetic moments can also be derived from astrophysical objects. Nonzero neutrino magnetic moments would allow for an enhanced rate of plasmon decay $\gamma \to \nu\bar{\nu}$, which would increase the core mass of red giants at the helium flash by $\delta M_C = 0.015 M_\odot \mu_\nu / 10^{-12}\mu_B$. By comparing the predicted δM_C with observations, a stronger limit on the neutrino magnetic moment is obtained [34]:

$$\mu_\nu < 3 \times 10^{-12}\mu_B \quad (3\sigma\ \text{CL}). \tag{1.47}$$

Note that there is a vast gap between present experimental bounds on neutrino magnetic moments and prediction (1.43) of the minimal extension of the Standard Model. Detection of a large neutrino magnetic moment near the current experimental limit will signify new physics beyond the Standard Model.

1.2 Supernova Relic Neutrinos

A detection of neutrinos from supernovae provides a unique tool to probe stellar interiors and study neutrino properties. Much has already been learned from the handful of events from SN 1987A. It is expected that knowledge on supernova and neutrinos will be greatly advanced with next detection of Galactic supernova explosion. Unfortunately, core-collapse supernova explosion is very rare in our galaxy, $\lesssim 3$ per century (see e.g. [35, 36]). However, neutrinos emitted from all past core-collapse supernovae should cumulate to form the supernova relic neutrino flux, which might be detectable in SK and future neutrino detectors. Detection of SRN will provide invaluable information on supernova neutrino emission, global core-collapse supernova rate and neutrino properties. Although all flavors of neutrinos are emitted from core-collapse supernovae, we focus on $\bar{\nu}_e$, which is most likely to be detected at water Cherenkov detectors (see section 1.4).

1.2.1 Supernova Neutrinos

Supernova explosions occur at the final stages of evolution of isolated massive stars. For historical reasons, supernovae are classified into different types based on their spectroscopic characteristics and properties of the light curve, as shown in Fig. 1.2. Supernovae can also be divided into two categories according to the mechanism that triggers the explosion. Type Ia supernovae are believed due to the thermonuclear disruption of white drafts, while Type Ib, Ic and II supernovae are generated by the collapse of the core of massive stars ($M \gtrsim 8M_\odot$). From the point of view of neutrino physics, core-collapse supernovae are more interesting, because they can produce all types of copious neutrinos.

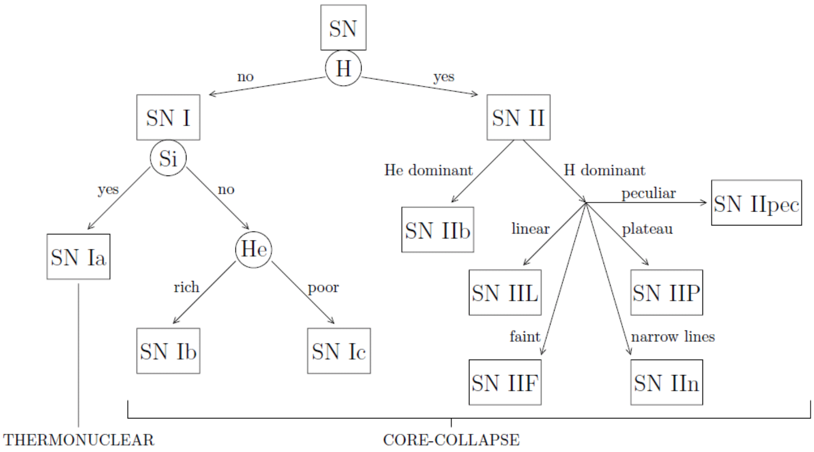

Figure 1.2: The classification scheme of supernovae [13].

During a core-collapse explosion, about 99% of the gravitational binding energy liberated by the collapse is carried away by neutrinos, leaving behind a neutron star or a black hole. The current understanding of core-collapse explosion and neutrino emission is briefly outlined below [13, 37, 38].

1. *Photodisintegration and neutronization* In the iron core of a massive star at its last stage of evolution, the gravitational force is sustained by

the pressure of degenerate relativistic electrons. At the very high temperature and densities that exists in the core, the photodisintegration of iron nuclei

$$\gamma +^{56}\mathrm{Fe} \to 13\alpha + 4n - 124.4\,\mathrm{MeV}, \tag{1.48}$$

and the electron capture of nuclei

$$e^- + N(Z, A) \to N(Z-1, A) + \nu_e, \tag{1.49}$$

occur, leading to a reduction of pressure support and triggering a rapid collapse of the core. In this so-called capture phase, only ν_e's are emitted and can escape freely from the core, since the mean free path is much longer than the radius of the core. However, the amount of emitted neutrinos are negligible compared to the later phases.

2. *Neutrino trapping* In the inner part of the core, the collapse is homologous (i.e. the velocity roughly proportional to the radius). On the other hand, the material outside of some point collapse supersonically in quasi-free fall with velocity proportional to the inverse square of the radius. When the density of the inner part of the core exceeds $10^{11} - 10^{12}\,\mathrm{g\,cm^{-3}}$, electron neutrinos begin to be trapped in the core, driven by the coherent scattering off nuclei. There exists a characteristic surface with radius

$$R_\nu \approx 1.0 \times 10^7\,\mathrm{cm}\left(\frac{E_\nu}{10\,\mathrm{MeV}}\right), \tag{1.50}$$

   which defines the neutrinosphere. Neutrinos produced at $R > R_\nu$ can freely escape from the core, while neutrinos produced inside can only diffuse out like the photons from the photosphere of normal stars.

3. *Core bounce and neutrino emission* The homologous collapse continues until the inner core reaches the nuclear density ($\sim 10^{14}\,\mathrm{g\,cm^{-3}}$). The repulsive nuclear forces halt the collapse and drive a shock wave outwards into the in-falling outer core. As the shock propagates into the outer core dissociating nuclei into free protons and neutrons, a huge number of electron neutrinos are produced through electron capture $e^- + p \to n + \nu_e$. Furthermore, since the cross section of coherent scattering is proportional to the square of mass number ($\sigma_{\mathrm{coh}} \propto A^2$), the previously trapped ν_e's now decouple from the matter. Such a sudden liberation of electron neutrinos is called a prompt electron neutrino burst or neutronization burst. The peak luminosity exceeds 10^{53} erg s^{-1}, but the total energy emitted is of the order of 10^{51} erg due to the short duration timescale ($\sim$ a few ms).

At about the same time, neutrinos of all flavors emerge thermally in the hot post-bounce region via processes such as the electron-positron annihilation

$$e^- + e^+ \to \nu + \bar{\nu}, \tag{1.51}$$

and the nucleon-nucleon bremsstrahlung

$$N + N \to N + N + \nu + \bar{\nu}. \tag{1.52}$$

In addition, ν_e and $\bar{\nu}_e$ are produced by the charged-current interactions, $e^- + p \to n + \nu_e$ and $e^+ + n \to p + \bar{\nu}_e$.

4. *Delayed explosion* When propagating outwards, the shock loses energy by photodisssociation of nuclei ($\sim 1.7 \times 10^{51}$ erg to disintegrate 0.1 $M_\odot$ iron) and neutrino emission behind the shock front. So only for special combinations of physical parameters, e.g. the progenitor star is relatively small ($\sim 10\, M_\odot$) and the equation of state is soft enough, the shock is able to expel the envelope of the star, generating the prompt explosion on the time scale of ~10 ms. In more realistic cases, the shock stalls after losing a fair amount of energy. A supernova explosion can still be achieved through the neutrino-heating mechanism, in which the shock is revived by the energy deposition of neutrinos. This neutrino-driven mechanism can delay the timescale of the explosion up to ~1 second, and is referred to as the delayed explosion mechanism, which is believed more likely.

5. *Remnant of the star* The duration of thermal neutrino emission is of the order of 10 seconds. Eventually, the protoneutron star cools and turns into a neutron star or a black hole, depending on its mass and initial metallicity.

The total amount of gravitational binding energy released in a supernova explosion is estimated to be

$$E_{\mathrm{bind}} \sim \frac{3}{5}\frac{GM_{\mathrm{NS}}^2}{R_{\mathrm{NS}}} \sim 3 \times 10^{53} \left(\frac{M_{\mathrm{NS}}}{1.4\, M_\odot}\right)^2 \left(\frac{R_{\mathrm{NS}}}{10\,\mathrm{km}}\right)^{-1} \mathrm{erg}, \tag{1.53}$$

where M_{NS} and R_{NS} are the typical mass and the radius of a neutron star. Only a small fraction (~1%) of the total energy is radiated kinetically; the rest are carried away by neutrinos. It's generally believed that each flavor of the six neutrinos and anti-neutrinos carries away approximately the same amount of energy, since most neutrinos are emitted in pairs (see Eqn. (1.51) and (1.52)). The total energy derived from SN 1987A data is consistent with the estimation in (1.53) [39]. A recent improved analysis of SN 1987A data finds the best fit of total energy to be 2.2×10^{53} erg [40], which is also close to expectations. In numerical simulations, however, the equipartition of luminosity is still controversial. Although some simulations find the luminosities are indeed nearly equal for all flavors (see e.g. Ref. [41]), significant deviations are also seen in other simulations, e.g. a factor of 2 difference between ν_x and $\bar{\nu}_e$ luminosities [42]. We remark that in the existing literature, there is still no consistent picture of neutrino luminosities and spectra. The simulation done in Ref. [41] succeeded in obtaining an delayed explosion, but it lacked some relevant neutrino processes. On the other hand, although the simulation in Ref. [42] did include the relevant neutrino processes, it only reached 150 ms, when the bulk of neutrinos have not been emitted. This ambiguity seriously complicates the calculation of SRN flux, as will be discussed in section 1.2.2.

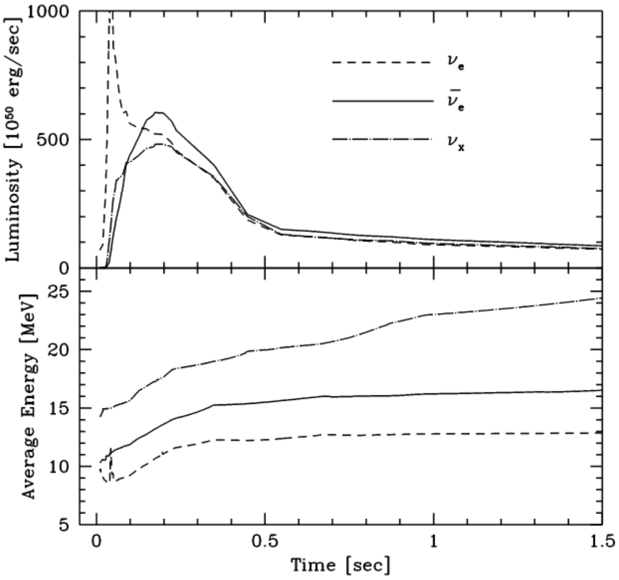

Figure 1.3: Time evolution of neutrino luminosity and average energy obtained with a numerical simulation of supernova explosion [41]. The dashed line represents ν_e, solid line indicates $\bar{\nu}_e$ and dot-dashed line is for ν_μ, $\bar{\nu}_\mu$, ν_τ, $\bar{\nu}_\tau$, which are collectively denoted as ν_x.

Fig. 1.3 shows the time evolution of neutrino luminosity and average energy in the first 1.5 seconds obtained with a numerical simulation of supernova explosion [41]. The involved model is for a progenitor star of about $\sim 20\, M_\odot$ which explodes by the delayed explosion mechanism. The strong peak on ν_e spectrum in Fig. 1.3 corresponds to the neutronization burst.

Note also that there is a “hump” in the neutrino luminosity curve due to the accretion of matter on the protoneutron star. The neutrino energy during the hump is low because the dense matter above the neutrinosphere is opaque to high energy neutrinos. In case of a prompt explosion, the envelope would be expelled in $\mathcal{O}(10)$ ms after the core bounce and there would be no hump in the luminosity curve and the neutrino spectrum would be harder. The detection of neutrinos from SN 1987A in the Large Magellanic Cloud (at a distance of ∼50 kpc) by Kamiokande II [1] and IMB [2] experiments confirms the basic understanding of supernova explosion. The detected number of events (11 for Kamokande II and 8 for IMB), however, is too small to derive a solid conclusion about the explosion mechanism. A future detection of a nearby neutrino burst , e.g. a supernova at the Galactic center, by the Super-Kamiokande detector will reveal clearly the signatures in the time evolution of the delayed explosion mechanism.

Fig. 1.3 (lower panel) also suggests the following hierarchy of average neutrino energy

$$\langle E_{\nu_e} \rangle < \langle E_{\bar{\nu}_e} \rangle < \langle E_{\nu_x} \rangle \,. \tag{1.54}$$

The average energy of neutrinos reflects the temperature of matter around the neutrinosphere, inside which thermal equilibrium is established. Neutrinos emitted from a deeper and hotter layer (corresponds to a smaller neutrinosphere) have higher energies. The ν_x's only experience the neutral current interactions , hence the corresponding neutrinosphere for ν_x is smallest among all neutrino species. On the other hand, although both ν_e and $\bar{\nu}_e$ undergo the charged current as well as neutral current interactions, the neutrinosphere for $\bar{\nu}_e$ is smaller than that for ν_e because the protoneutron star is neutron rich. The energy hierarchy (1.54) is a fairly robust prediction of the current supernova theory, but it is not easy to derive quantitatively the time-integrated average energies without detailed numerical simulations. The average neutrino energies for all flavors obtained in [41, 43] are roughly

$$\begin{aligned} \langle E_{\nu_e} \rangle &\simeq 13\,\mathrm{MeV} \\ \langle E_{\bar{\nu}_e} \rangle &\simeq 16\,\mathrm{MeV} \\ \langle E_{\nu_x} \rangle &\simeq 23\,\mathrm{MeV} \end{aligned} \tag{1.55}$$

In the literature, the energy spectrum of supernova neutrinos of each flavor is usually approximated by the Fermi–Dirac (FD) distribution with a zero potential (see e.g. [44])

$$\frac{dN}{dE} = L \frac{120}{7\pi^4} \frac{E^2}{T^4} \frac{1}{e^{E/T}+1}, \tag{1.56}$$

where $T \simeq \langle E \rangle /3.1514$ is the effective neutrino temperature and L is the total luminosity. However, the neutrino emission in a supernova burst is not perfectly thermal because the interaction cross sections $\propto E^2$ so that the neutrinosphere radius vary even for the same species of neutrinos. Fig. 1.4 shows the energy spectrum of $\bar{\nu}_e$ obtained from a numerical supernova simulation [41], where both the low- and high-energy range are suppressed compared to a pure FD distribution. This feature can be accommodated by using a "pinched" FD distribution [45, 42]

$$\frac{dN}{dE} = L \frac{1}{F(\eta)} \frac{E^2}{T^4} \frac{1}{e^{E/T-\eta}+1}, \tag{1.57}$$

where η is a pinching parameter and $F(\eta) = dx\, x^3/(e^{x-\eta}+1)$ is a normalization factor. In this case, the average energy depends on both T and η, and up to second order, $\langle E/T \rangle \approx 3.1514 + 0.1250\eta + 0.0429\eta^2$. Another popular way to parametrize the neutrino spectrum is [42, 46]

$$\frac{dN}{dE} = L \frac{(1+\beta)^{1+\beta}}{\Gamma(1+\beta)\overline{E}^2} \left(\frac{E}{\overline{E}}\right)^{\beta} e^{-(\beta+1)E/\overline{E}}, \tag{1.58}$$

with $\overline{E}$ being the average energy and β a parameter related to the width of the spectrum.

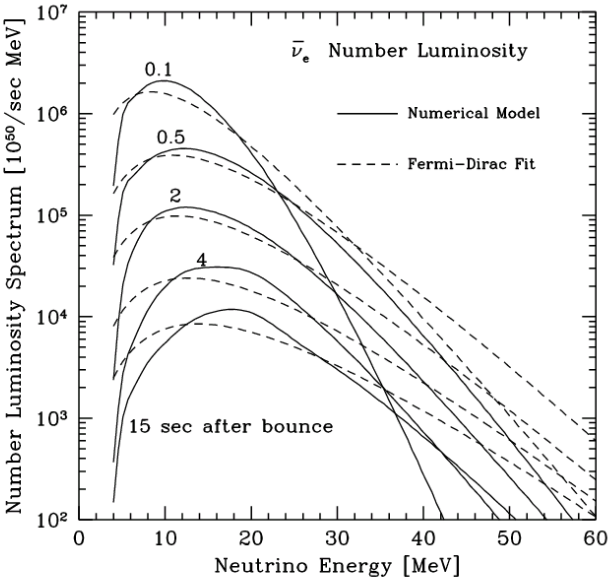

Figure 1.4: Energy spectrum of ν_e of the numerical model in Ref. [41]. The dashed lines are for FD fits with zero chemical potential.

1.2.2 Supernova Relic Neutrinos

Supernova relic neutrino has been the focus of many theoretical studies, dating back more than forty years. The predicted SRN flux in early papers, however, have very large uncertainties (see [47] and references therein). Since mid-1990s, more detailed and realistic calculations of SRN flux emerge [48, 49, 50, 51, 44, 52, 53, 54, 55, 56]. The SRN flux is a convolution of core-collapse supernova rate with the neutrino emission per supernova, taking into account the redshift effects. The present differential number flux of SRN at Earth is given by [47, 57]

$$\frac{d\phi}{dE_\nu}(E_\nu) = c\int_0^\infty R_{\rm SN}(z)(1+z)\frac{dN[E_\nu(1+z)]}{dE_\nu}\left|\frac{dt}{dz}\right| dz, \tag{1.59}$$

where $R_{\rm SN}$ is the core-collapse supernova rate at redshift z; dN/dE_ν is the number spectrum emitted by one supernova explosion, where a neutrino received at energy E_ν was emitted at a higher energy $E_\nu(1+z)$; the relation between the cosmic time t and the redshift z is given by the Friedmann equation as

$$\frac{dz}{dt} = -H_0(1+z)\sqrt{(\Omega_{\rm m}(1+z)^3 + \Omega_\Lambda)}, \tag{1.60}$$

with H_0 being the Hubble constant; $\Omega_{\rm m}$ and Ω_Λ are the cosmic matter density and cosmological constant, respectively. Essentially all theoretical predictions of SRN flux follow from (1.59), with variations in the modeling of core-collapse supernova rate, neutrino emission and possibly the choice of cosmological parameters. As noted in [48, 44], the SRN flux is insensitive to the cosmology model. With an appropriate choice, the SRN flux can be made independent of the cosmological parameters [53, 55]. In any case, the uncertainty due to the cosmology models can be neglected. The distinctive features of each SRN model reside in the derivation of core-collapse supernova rate and the choice of neutrino emission models, which we will examine in more details below.

Rate of Core-collapse Supernovae

Over the last two decades, understanding of the supernova rate and its time dependence has been steadily improved. In the first detailed calculation of SRN flux by Totani and Sato [48], the supernova rate is estimated from the abundance of oxygen, which is produced chiefly in Type II supernovae, and it's assumed to be constant over time. In their second paper [49], a standard model of galaxy evolution based on the population synthesis method was used to derive the supernova rate. Later Malaney [50] proposed a model for the evolution of cosmic gas, from which the supernova rate is determined. At about the same time, Hartmann and Woosley [51] published their SRN model where the time dependence of the supernova rate was evaluated based on the cosmic chemical evolution. In another model by Kaplinghat *et al.* [44] the supernova rate was calculated using the metal enrichment history under the assumption that the supernova rate tracks the metal enrichment rate. In recent SRN models [53, 54, 55, 56], the supernova rate was derived directly from the cosmic star formation history. The supernova rate is expected to be proportional to the star formation rate (SFR) since the lifetime of massive stars is much shorter than the cosmological time scale. The precision on SFR has been greatly improved by direct measurements based on emission of massive stars (see e.g. Ref. [58]), which enables a fairly accurate determination of the core-collapse supernova rate.

The SFR is usually derived from measurements of living massive stars (see Ref. [47] for details). When converting observables to SFR, one has to assume that the distribution of stellar masses at formation follows an initial mass function (IMF). The widely adopted Salpeter IMF scales as $\phi(m) \propto m^{-2.35}$ for stellar mass between $0.1\,M_\odot$ and $100\,M_\odot$ [59]. Fig. 1.5 shows the SFR density $\dot{\rho}_*(z)$ (in units $M_\odot\,\mathrm{Mpc}^{-3}\,\mathrm{year}^{-1}$) derived from various indicators, which are scaled to a Salpeter IMF. A general consistency is clearly seen, especially for redshift $z \lesssim 1-2$, which is most relevant for the SRN prediction [57]. Note that the SFR is about ten times larger at $z = 1$ than at present, $z = 0$. In the literature, several parameterizations of $\dot{\rho}_*(z)$ exist, see e.g. [53, 54, 58]. For $z \lesssim 1$, $\dot{\rho}_*(z)$ can be approximated by

$$\dot{\rho}_*(z) = \dot{\rho}_0(1+z)^\beta, \tag{1.61}$$

where $\dot{\rho}_0$ is a normalization factor and $\beta \approx 3$ [58].

For a given SFR, the core-collapse supernova rate is calculated as

$$R_{\mathrm{SN}(z)} = \dot{\rho}_*(z)\frac{\int_8^{50}\phi(m)dm}{\int_{0.1}^{100}m\phi(m)dm}. \tag{1.62}$$

The mass limits (in units $M_\odot$) in the integrals of (1.62) are the values adopted in Ref. [54]; different values are used by other authors, see e.g. [52, 53, 55]. It has been pointed out by those authors, however, the upper mass bounds are not important as long as they are large. The lower mass threshold in the upper integral, on the other hand, is more profound. It was generally believed that the minimum stellar mass that leads to a core-collapse is about $8\,M_\odot$. Recent studies find the minimum mass has converged to $8 \pm 1 M_\odot$ [60], which leads to about 10% uncertainties in R_{SN} [54]. It should be noted that

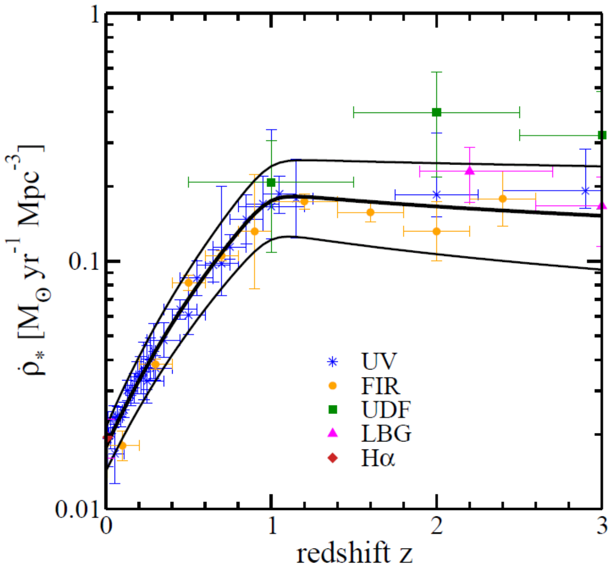

Figure 1.5: Redshift evolution of SFR density [54]. Data points represent measurements using various techniques, scaled to a Salpeter IMF. Curves show the parameterization (thick) and adopted uncertainty range (thin) in Ref. [54].

$R_{\rm SN}$ predicted in this way depends weekly on the IMF because the effects of the IMF between $\dot{\rho}_*(z)$ and the integrals are largely canceled out [54].

Ref. [54] compared the predicted $R_{\rm SN}$ with the direct observations and found good agreements. Together with other cross-checks, the authors concluded that the uncertainties associated with $R_{\rm SN}$ is fairly small, which translates into a variation of ±40% in the SRN event spectrum. It's worth noting that $R_{\rm SN}$ derived in these models include all core collapses. The collapse of stars with stellar mass $8M_\odot \lesssim M \lesssim 25M_\odot$ leads to an explosion and produces a neutron star; stars with $25M_\odot \lesssim M \lesssim 40M_\odot$ also result in (weaker) explosions but produce black holes via fallback; for $M \gtrsim 40M_\odot$, the collapse leads to direct black hole formation without an explosion, i.e. a failed supernova [61]. Recent studies show that neutrino emission from a black hole-forming collapse is more energetic than that from a neutron star-forming one (see [56] and references therein). This will lead to a harder SRN spectrum, which is easier to detect.

Supernova Neutrino Emission

While the supernova rate has been known with rather good accuracy and the precision will continuously improve in future, uncertainties on supernova neutrino emission remain quite large. Neither the total luminosity of each flavor of neutrino nor the exact functional form of the energy spectrum is well known, see section 1.2.1. Neutrino mixings make the situation more complicated.

The neutrino emission for each flavor is characterized by the total luminosity L_ν and neutrino temperature T_ν if the neutrino spectrum is perfectly thermal (see Eqn. (1.56)). An additional parameter, usually dictated by the numerical simulation, is needed if one uses Eqn. (1.57) or (1.58). The total luminosity is often taken as $L_\nu = E_{\text{bind}}/6 \simeq 5\times 10^{52}$ erg assuming equipartition [52, 55, 54], or adopted from numerical simulations [48, 49, 50, 51, 44, 53, 56]. The choice of neutrino temperature also heavily relies on numerical simulation results. In typical scenarios, $T_{\bar{\nu}_e} \simeq 5$ MeV and $T_{\nu_x} \simeq 8$ MeV. Based on theoretical arguments, experimental results of SN 1987A data and SK 2003 SRN limit, $T_{\bar{\nu}_e} < 4$ MeV or $T_{\bar{\nu}_e} > 8$ MeV is disfavoured [54], where $T_{\bar{\nu}_e}$ is the effective neutrino temperature including neutrino mixing effects. In principle, the neutrino emission spectrum dN/dE_ν in Eqn. (1.59) should integrate over progenitor masses that lead to core-collapse supernovae. However, it has been shown that neither the neutrino temperature nor the binding energy of the neutron star depends sensitively on the mass of the progenitor [51, 62]. Hence, using a single neutrino spectrum is a valid approximation, as often done in the literature.

Neutrino oscillations also play an important role in predicting SRN flux. The observed $\bar{\nu}_e$ spectrum $\phi_{\bar{e}}$ is a linear combination of $\bar{\nu}_e$ and $\bar{\nu}_x$ at production, i.e.

$$\phi_{\bar{e}} = \bar{p}\phi^0_{\bar{e}} + (1-\bar{p})\phi^0_{\bar{x}}, \tag{1.63}$$

where $\phi^0_{\bar{e}}$ and $\phi^0_{\bar{x}}$ are original fluxes for $\bar{\nu}_e$ and $\bar{\nu}_x$, respectively; $\bar{p}$ is the total $\bar{\nu}_e$ survival probability including both oscillation effects in the star and Earth matter [63]. Presence of a $\bar{\nu}_x$ component will make the spectrum harder, since the temperature of $\bar{\nu}_x$ is higher than $\bar{\nu}_e$. The Earth matter effect on SRN flux is estimated to be small [64]. Inside the star, MSW-enhanced neutrino mixings is rather complex, crucially depends on the progenitor density profile, the neutrino mass hierarchy and the magnitude of θ_{13} (see Ref. [63] for details). Recently it has been realized that collective flavor conversions induced by neutrino-neutrino interactions can cause spectral swaps [65, 66]. Furthermore, as described earlier, the initial neutrino spectra are not well understood. Therefore, we stress that a full quantitative treatment of neutrino mixing effects for SRN is impractical. SRN models [53, 56] that take into count explicitly neutrino oscillation effects depend on numerical simulations and mixing parameters, which is not universally applicable. Alternatively, one can use an effective spectrum to account for the mixing effects, which is the approach of model [54] (see discussions of HBD09 below).

SRN models

We now introduce in some detail several specific SRN models and predictions. Early models will not be assessed in this thesis due to the lack of accuracy in the supernova rate and the omission of neutrino mixing. The models of the following are representative and reflect some new developments on this subject.

- Ando, Sato and Totani [53] (Ando LMA)
  This is the first model that takes into account neutrino oscillation in the calculation of SRN flux. The supernova rate is inferred from SFR assuming a Salpeter IMF. The initial neutrino spectra are based on numerical simulations in Ref. [41]. Neutrino mixings are included under the assumption of normal hierarchy. The oscillation probability for $\bar{\nu}_e$ is treated as the vacuum oscillation, which is actually inappropriate. In a latter paper by Ando and Sato [64], neutrino oscillations are treated more rigorously for both normal and inverted hierarchy. In case of inverted hierarchy, the observed spectrum is almost completely due to $\bar{\nu}_x$ if the conversion is adiabatic, leading to a even harder spectrum than in normal hierarchy.

- Lunardini [56] (Failed SN)
  The main point of this model is that it treats separately the neutrino spectra from neutron star-forming core-collapses (NSFCs) and black hole-forming ones (BHFCs). The observed $\bar{\nu}_e$ spectrum is written as

  $$\phi_{\bar{e}} = f_{\mathrm{NS}}\phi_{\bar{e}}^{\mathrm{NSFC}} + (1 - f_{\mathrm{NS}})\phi_{\bar{e}}^{\mathrm{BHFC}}, \tag{1.64}$$

  where f_{NS} is the fraction of NCFCs. Evidently, the calculation of the SRN spectrum from (1.64) introduces additional uncertainties associated with f_{NS} and the neutrino spectra from BHFCs. For the evaluation in this thesis, we choose parameters that maximize the observable SRN flux. Since neutrinos emitted from NSFCs are more energetic, the observable $\bar{\nu}_e$ spectrum might be further hardened. In turn, observation of SRN can provide information on the rate of BHFCs, which is difficult to study otherwise.

- Horiuchi, Beacom and Dwek [54] (HBD 6 MeV)
  In this model, the core-collapse supernova rate is derived from most up-to-date SFR data. The authors find that the uncertainties on the

> supernova rate is already fairly small, allowing to study the supernova neutrino emission in more details. The $\bar{\nu}_e$ spectrum per supernova is approximated by the Fermi-Dirac distribution (1.56), where $T_{\bar{\nu}_e}$ is interpreted as the effective temperature including neutrino mixing effects. The SRN flux predicted in this way is characterized entirely by the total luminosity $L_{\bar{\nu}_e}$ and the effective temperature $T_{\bar{\nu}_e}$. One might consider that using the Fermi-Dirac distribution to represent $\bar{\nu}_e$ spectrum after neutrino mixing is an oversimplification. Even if the initial spectra can be approximated by Fermi-Dirac distributions, in general it does not hold that the superimposition of two spectra with different $T_{\bar{\nu}_e}$ still follows the Fermi-Dirac distribution. However, such "fine points" are probably washed out by the redshift integral, detector resolution, etc. Besides, the expected rate at SK is only 1.2-5.6 events yr^{-1} in the range of 10-26 MeV. Details of the neutrino spectrum can not be resolved with such small statistics. Therefore, despite of the uncertainties in neutrino spectrum, we consider this model as a main guidance since it provides a general and simple framework to extract physical information from SRN observations. For evaluation in this thesis, the adopted effective neutrino temperature is 6 MeV.

Fig. 1.6 shows the $\bar{\nu}_e$ flux spectra predicted by some SRN models, which peak at below 10 MeV due to redshift. Although the total flux predicted by various models span a fairly wide range, the shape of the spectra is quite similar, especially above 10 MeV.

1.3 Anti-neutrinos from the Sun

The Sun is an intense source of neutrinos produced in thermonuclear reactions that are thought to power the Sun. There are two groups of nuclear reactions occurring in the Sun: the main proton-proton chain (*pp* chain) and the sub-dominant Corbon-Nitrogen-Oxygen cycle (CNO cycle). The main result of both the *pp* chain and the CNO cycle is a fusion of hydrogen into helium:

$$4p + 2e^- \rightarrow {}^4\mathrm{He} + 2\nu_e + 26.73\,\mathrm{MeV}. \tag{1.65}$$

Fig. 1.7 shows the solar neutrino spectra predicted by the Standard Solar Model (SSM). Uncertainties on theoretical predictions of neutrino flux come mainly from the surface composition of the Sun and nuclear reaction cross sections [67]. The 1σ theoretical uncertainties on solar neutrino flux is also shown in Fig. 1.7.

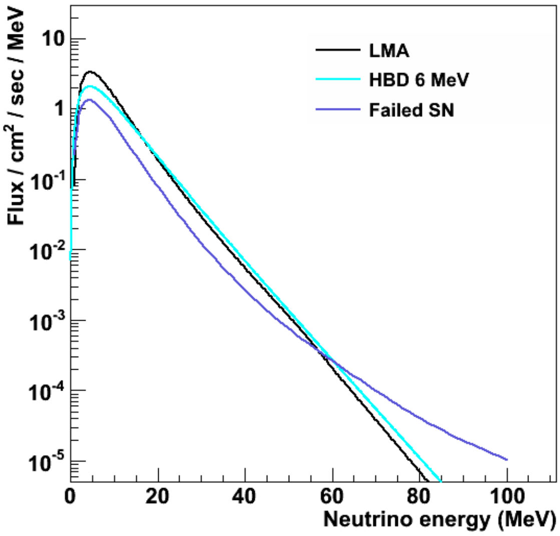

Figure 1.6: Model predictions of the SRN flux.

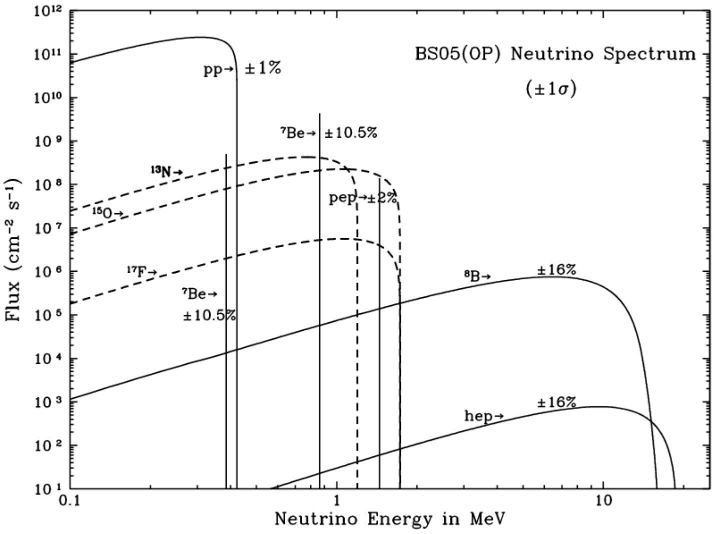

Figure 1.7: Spectra of solar neutrinos from the *pp* and CNO chains, predicted by the SSM BS05(OP). Figure taken from Ref. [68].

1.3.1 The Solar Neutrino Problem and the MSW-LMA Solution

Solar neutrinos were originally conceived as a unique tool to investigate the Sun's interior. For over 40 years, a large amount of solar neutrino data have been accumulated by various types of detectors. However, a deficit of solar neutrinos relative to the SSM prediction was observed in all early solar neutrino experiments Homestake, Kamiokande, Gallex/GNO and SAGE. For a long time, the discrepancy between the observed solar neutrino flux and the SSM prediction was referred to as *the solar neutrino problem*.

The standard solar model is very successful at describing many other aspects of the Sun (e.g. the results from helioseismology). In addition, since different neutrino experiments are sensitive to neutrinos produced by different reactions in the *pp* chain, there's no apparent way to solve the solar neutrino problem by modifying the astrophysical prediction. The problem may lie in our understanding of neutrinos. A number of particle physics solutions were proposed to reconcile the SSM prediction with data. It turns out the solar neutrino problem can be naturally explained in terms of neutrino oscillation. The neutrino oscillation solution became more plausible after the discovery of neutrino oscillation in atmospheric neutrino data by Super-Kaimiokande in 1998.

The oscillations of solar neutrinos can be enhanced in the Sun by the MSW effect (see section 1.1.1). The solar neutrino data before Super-Kamiokande can be fit with the small mixing angle (SMA), large mixing angle (LMA) and low Δm^2 (LOW) MSW enhanced oscillations and the vacuum oscillation (VO). This situation was cleared up with the results from SK and SNO, which were complemented by KamLAND.

Super-Kamiokande measured the solar ^{8}B neutrino flux with unprecedented precision. There is no indication of seasonal variation in oscillation probability and hence VO is disfavored. The recoil electron energy spectrum is flat, which disfavors SMA. SNO measured the total active neutrinos from the Sun via the NC reaction and found a good agreement with the SSM prediction. Therefore, SNO results provided a decisive proof that solar ν_e's do change to the other flavors of neutrinos (ν_μ, ν_τ). Combined SK and SNO data indicate that LMA is a better solution to the solar neutrino problem. The LMA oscillation scenario was then confirmed by KamLAND using reactor neutrinos.

The neutrino oscillation probability from MSW-LMA prediction varies with neutrino energy. The vacuum oscillation dominates for $E_\nu \lesssim 1$ MeV. For $E_\nu \gtrsim 5$ MeV, the oscillation is independent of neutrino energy due to MSW resonance enhancement. Data in both low energy region (*pp* neutrino) and high energy region (^{8}B neutrino) are consitent with the MSW-LMA oscillation. Data in the intermediate region are eagerly awaited to further test the characteristic transition of the MSW-LMA prediction. The new measurements of ^{7}Be and *pep* neutrinos from Borexino are also in good agreement with the MSW-LMA prediction (see Fig. 1.8). In sum, the MSW-LMA os-

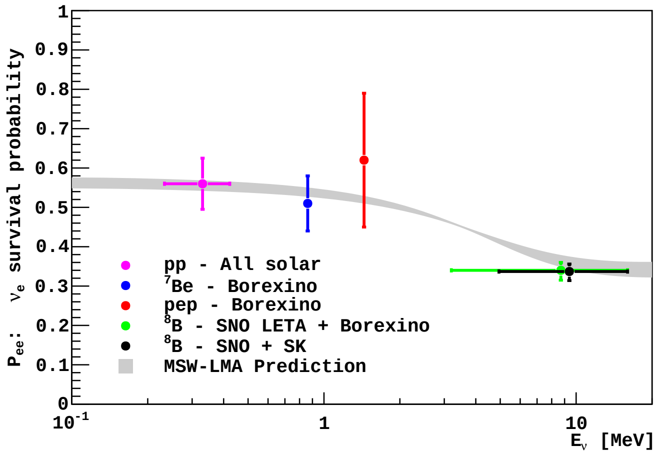

Figure 1.8: Sloar ν_e survival probability as a function of energy [69].

cillation fits all available solar neutrino data and is the present best solution to the solar neutrino problem.

1.3.2 Neutrino Spin-flavor Precession and $\bar{\nu}_e$ Generation

A nonzero neutrino magnetic moment (see section 1.1.2) gives rise to spin precession in a magnetic field, leading to $\nu_{e_L} \to \nu_{e_R}$. Since light right-handed neutrinos are sterile, they will escape detection. Historically, such mechanism was investigated in attempting to explain the solar neutrino depletion [70]. Although it has now been established that the solar neutrino deficit is due to MSW-LMA neutrino oscillations, neutrino magnetic moment can still play a role at a subdominant level. Most interestingly, if neutrinos have transition magnetic moments and neutrinos are Majorana particles, the combined effects of neutrino oscillation and spin-flavor precession may result in an observable $\bar{\nu}_e$ flux from the sun.

It is instructive to consider first the ordinary spin-precession for a Dirac neutrino, which can have a diagonal magnetic moment. The evolution equation in a transverse magnetic filed B and in the presence of a matter potential V_e, is given by

$$i\frac{d}{dt}\begin{pmatrix} \nu_{e_L} \\ \nu_{e_R} \end{pmatrix} = \begin{pmatrix} V_e & \mu B \\ \mu B & 0 \end{pmatrix}\begin{pmatrix} \nu_{e_L} \\ \nu_{e_R} \end{pmatrix}, \tag{1.66}$$

where μ is the magnetic moment. For simplicity, assuming constant matter density and constant B, solving Eqn. (1.66) gives the transition probability

$$P_{\nu_{e_L}\to\nu_{e_R}} = \frac{(2\mu B)^2}{V_e^2+(2\mu B)^2}\sin^2\left(\frac{1}{2}\left[V_e^2+(2\mu B)^2\right]^{1/2}t\right). \tag{1.67}$$

In case of $V_e = 0$, i.e. in vacuum, the amplitude is unity and complete $\nu_{e_L}\to\nu_{e_R}$ can take place. The conversion probability is suppressed by the matter potential V_e.

If transition magnetic moments exist, spin-flavor precession (SFP) $\nu_{e_L}\to\nu_{\mu_R}$ can occur. Considering two flavors of Dirac neutrinos, the evolution equation is governed by a four-dimensional Hamiltonian [71, 72, 73, 25],

$$i\frac{d}{dt}\begin{pmatrix}\nu_{e_L}\\ \nu_{\mu_L}\\ \nu_{e_R}\\ \nu_{\mu_R}\end{pmatrix} = \begin{pmatrix}-c_2\delta+V_e & s_2\delta & \mu_{ee}B & \mu_{e\mu}B\\ s_2\delta & c_2\delta+V_\mu & \mu_{\mu e}B & \mu_{\mu\mu}B\\ \mu_{ee}B & \mu_{\mu e}B & -c_2\delta & s_2\delta\\ \mu_{e\mu}B & \mu_{\mu\mu}B & s_2\delta & c_2\delta\end{pmatrix}\begin{pmatrix}\nu_{e_L}\\ \nu_{\mu_L}\\ \nu_{e_R}\\ \nu_{\mu_R}\end{pmatrix}, \tag{1.68}$$

where $c_2 = \cos 2\theta$, $s_2 = \sin 2\theta$, and $\delta = \Delta m^2/4E$. As noted above, the matter potentials suppress $\nu_{e_L}\to\nu_{e_R}$ conversion. However, in addition to MSW resonances, the matter potentials can generate resonant spin-flavor precession, which can be identified by equating terms along the diagonal in Eqn. (1.68). There is a resonance in the $\nu_{e_L}\leftrightarrows\nu_{\mu_R}$ channel for

$$V_e = \frac{\Delta m^2}{2E}\cos 2\theta. \tag{1.69}$$

Note that this resonance condition is different from that of the MSW resonance (1.35), because of the neutral-current contribution to V_e. There is also a resonance in the $\nu_{\mu_L}\leftrightarrows\nu_{e_R}$ channel for

$$V_\mu = -\frac{\Delta m^2}{2E}\cos 2\theta. \tag{1.70}$$

This resonance, however, requires too large a N_n which does not exist in the Sun. In practice, these resonances can lead to the disappearance of active left-handed neutrinos into sterile right-handed ones.

If neutrinos are Majorana particles, they have no diagonal magnetic moments and only one transition magnetic moment $\mu_{e\mu} = -\mu_{\mu e} \equiv \mu$. The Majorana nature means that the right-handed states are not sterile, but interact as active anti-neutrinos. The evolution equation for Majorana neutrinos becomes

$$i\frac{d}{dt}\begin{pmatrix}\nu_{e_L}\\ \nu_{\mu_L}\\ \bar{\nu}_{e_R}\\ \bar{\nu}_{\mu_R}\end{pmatrix} = \begin{pmatrix}-c_2\delta+V_e & s_2\delta & 0 & \mu B\\ s_2\delta & c_2\delta+V_\mu & -\mu B & 0\\ 0 & -\mu B & -c_2\delta-V_e & s_2\delta\\ \mu B & 0 & s_2\delta & c_2\delta-V_\mu\end{pmatrix}\begin{pmatrix}\nu_{e_L}\\ \nu_{\mu_L}\\ \bar{\nu}_{e_R}\\ \bar{\nu}_{\mu_R}\end{pmatrix}, \tag{1.71}$$

There are also two spin-flavor resonances, one in the $\nu_{e_L} \leftrightarrows \bar{\nu}_{\mu_R}$ channel for

$$V_e + V_\mu = \frac{\Delta m^2}{2E} \cos 2\theta, \tag{1.72}$$

and the other in the $\nu_{\mu_L} \leftrightarrows \bar{\nu}_{e_R}$ channel for

$$V_e + V_\mu = -\frac{\Delta m^2}{2E} \cos 2\theta. \tag{1.73}$$

For $\cos 2\theta > 0$, only the first resonance can be realized in the Sun where $N_n \simeq N_e/6$. Experimentally, the resultant $\bar{\nu}_{\mu_R}$'s are difficult to observe since they only participate in neutral-current interactions, given that solar neutrinos are below 20 MeV.

Now, if we combine the actions of oscillations and SFP, for Majorana neutrinos, an interesting phenomenon occur: emergence of solar $\bar{\nu}_e$. To achieve this, there are essentially two ways that can be schematically shown as

$$\nu_{e_L} \xrightarrow{\text{osc.}} \nu_{\mu_L} \xrightarrow{\text{SFP}} \bar{\nu}_{e_R}, \tag{1.74}$$

$$\nu_{e_L} \xrightarrow{\text{SFP}} \bar{\nu}_{\mu_R} \xrightarrow{\text{osc.}} \bar{\nu}_{e_R}. \tag{1.75}$$

In practice, only the processes (1.75) is important [74]. The combined probability for $\nu_{e_L} \to \bar{\nu}_{e_R}$ conversion, in the context of MSW-LMA oscillations, is worked out in Ref. [74] as

$$P(\nu_{e_L} \to \bar{\nu}_{e_R}) \simeq 1.8 \times 10^{-10} \sin^2 2\theta \left[\frac{\mu}{10^{-12}\mu_B} \frac{B_\perp(0.05R_\odot)}{10\,\text{kG}} \right], \tag{1.76}$$

where $B_\perp$ is the traverse magnetic field in the region where the production of solar ^{8}B neutrinos are maximum. Sufficient large μ and $B_\perp$ may lead to a solar $\bar{\nu}_e$ flux observable at SK. In turn, studies of solar $\bar{\nu}_e$ will provide a probe of the magnetic moment μ and the stregth of the magnetic field in the Sun.

1.4 Super-Kamiokande as an Anti-neutrino Detector

The inverse beta decay reaction (1.1) has a unique signature given by the close temporal and spatial correlation between the positron and neutron events, which is employed by liquid scintillator detectors, such as KamLAND and Borexino, to identify low energy $\bar{\nu}_e$. Unfortunately, this didn't work through

SK-I to III because the 2.2 MeV γ resulting from neutron captures on free protons is not energetic enough to make a trigger.

In 2004, Beacom and Vagins proposed to modify SK by adding gadolinium compound [75], neutron capture on which yields a gamma cascade with a total energy $\sim$8 MeV. These relatively high energy γ-rays should be readily seen in SK whose trigger threshold is $\sim$5 MeV. However, a number of technical issues (e.g. effects of Gd on materials and environment, upgrading water system to recirculate Gd solution) have to be settled before this idea can finally be realized in SK. In the second approach [76], a new trigger logic is introduced to force the DAQ system to take 500 μs data without a trigger threshold following each primary event above the so-called special high energy (SHE, see section 2.4.3) trigger ($\sim$10 MeV). A search of 2.2 MeV γ emitted from neutron capture on free proton is then performed offline exploiting the spatial and temporal correlation between the primary event and the 2.2 MeV γ. Fig. 1.9 illustrates the detection scheme of anti-neutrinos for both approaches. In the 2.2 MeV γ case, the temporal and spatial differences between the primary e^+ and delayed γ are $\sim$200 μs and $\sim$20 cm, respectively.

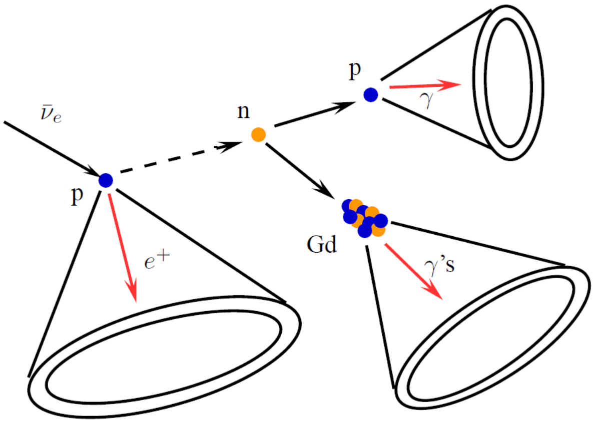

Figure 1.9: Illustration of the detection scheme of anti-neutrinos in SK-IV.

Following a successful demonstration of detecting neutron capture on free protons in SK-III [77], the forced trigger scheme has been incorporated into the SK DAQ system to record neutron capture events since the start of SK-IV in 2008. The time structure of the primary event (SHE trigger) and the delayed event (AFT trigger, see section 2.4.3) is illustrated in Fig. 1.10. Neutron tagging opens up a window to anti-neutrino physics in a large water Cherenkov detector. Note that at high energies, both neutrinos and anti-neutrinos can induce neutrons through various interactions (see chapter 8).

So we will content ourselves with $\bar{\nu}_e$ search via the IBD reaction for $E_{\bar{\nu}_e}$ well below 100 MeV.

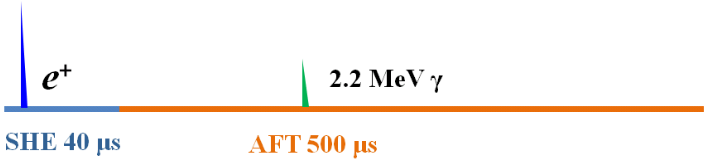

Figure 1.10: Illustration of the time structure of the primary event and the delayed event.

Fig. 1.11 shows the relevant cross sections for neutrino interactions in water. The IBD reaction has much larger cross section than the other channels, especially in the energy range $\lesssim$ 30 MeV. Actually, for the SRN search, event rate due to the IBD reaction dominates the other channels by two orders of magnitude [48]. So in the first approximation, SK observes the $\bar{\nu}_e$ component of SRN flux only through the IBD reaction. Note also in the energy range 10–20 MeV, the cross section for the inverse beta decay reaction is two orders of magnitude greater than the elastic scattering process $\nu_e + e^- \to \nu_e + e^-$. Therefore, the inverse beta decay reaction can also be a probe to the very small solar $\nu_e \to \bar{\nu}_e$ conversion probability.

Fig. 1.12 (a) shows fluxs of SRN and electron (anti)neutrinos from other sources at SK site. The flux of reactor $\bar{\nu}_e$ is overwhelmingly large below ~8 MeV. Atmospheric $\bar{\nu}_e$'s become dominant above ~30 MeV. Solar neutrinos are not a big concern, since they are not $\bar{\nu}_e$'s but ν_e's. Therefore, taking into account the detector resolution, there is a detection window 10–30 MeV for the search of extraterrestrial $\bar{\nu}_e$'s.

In practice, several backgrounds exist in the relevant energy range that may hinder the detection, e.g. decay electrons or positrons from invisible muons (atmospheric $\nu_\mu/\bar{\nu}_\mu$ below Cherenkov threshold). These backgrounds will be discussed in details in chapter 9. It suffices to mention here that most background events are not accompanied by neutrons. So the majority of irreducible backgrounds in the SK previous study can be eliminated with neutron tagging.

Although the neutron tagging efficiency is relatively low in SK-IV (see chapter 6), this disadvantage is compensated by its large target mass. In addition, liquid scintillator detectors suffer greatly from atmospheric neutral current background [79], which is much more modest in SK because the neutral current γ-rays can be distinguished from electrons (see section 9.6). In conclusion, SK-IV can serve as a competitive low energy anti-neutrino detector.

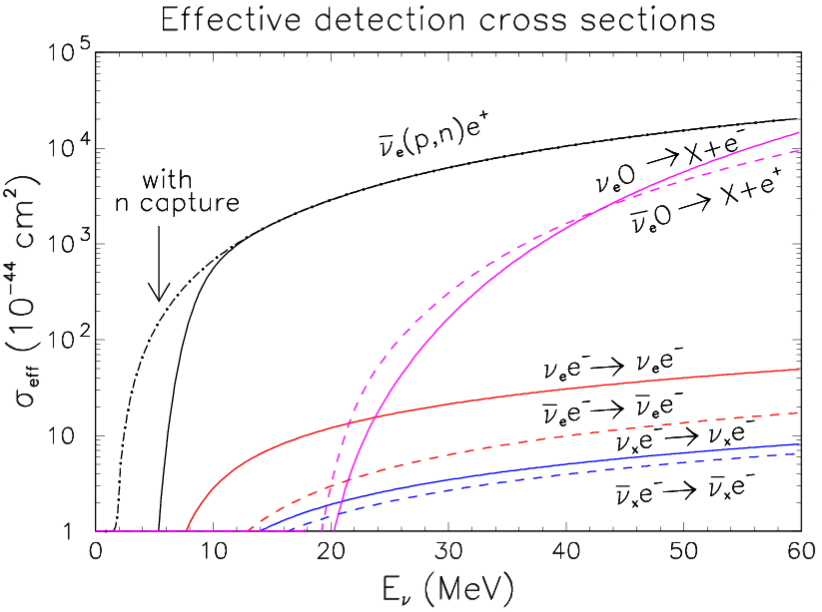

Figure 1.11: Effective cross sections for neutrino interactions in water, including the SK energy resolution and threshold effects. Figure from Ref. [78].

1.5 Previous Experimental Searches

A number of searches for SRN and solar $\bar{\nu}_e$ have been conducted using various detection techniques. Until now, all the searches are negative and upper limits are set. We summarize previous experimental results in the following. Here, energy refers to neutrino energy and all limits are set at the 90% confidence level.

SNO

SNO is a Cherenkov detector using heavy water to detect $\bar{\nu}_e$'s via

$$\bar{\nu}_e + d \rightarrow e^+ + n + n. \tag{1.77}$$

The coincidence of a positron with two neutrons allows SNO to search for $\bar{\nu}_e$ with very low background. Using the SNO phase I data, the integral limit on the flux of solar $\bar{\nu}_e$ in the energy range 4–14.8 MeV is found to be $\phi_{\bar{\nu}_e} \leq 3.4 \times 10^4\,\mathrm{cm}^{-2}\,\mathrm{s}^{-1}$, which corresponds to 0.81% of the SSM ^{8}B ν_e flux [80]. While no result on the $\bar{\nu}_e$ component of SRN is reported, SNO also performs a direct search of the ν_e component of SRN primarily through

$$\nu_e + d \rightarrow p + p + e^-. \tag{1.78}$$

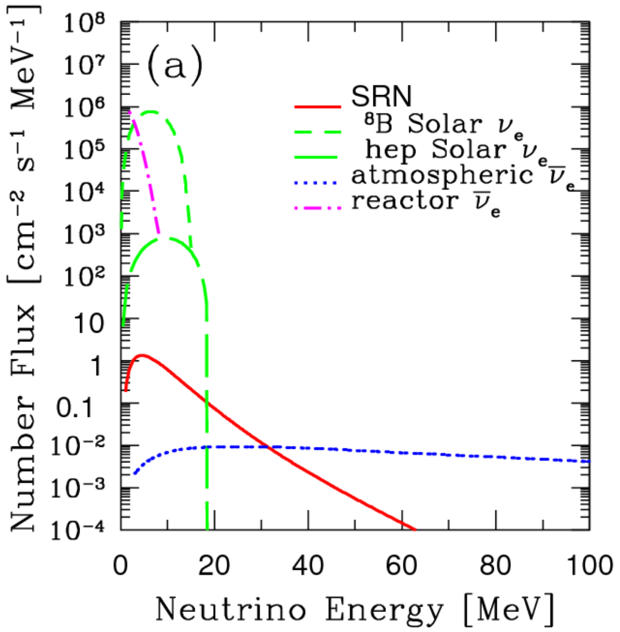

Figure 1.12: Fluxs of SRN (Ando03) and electron (anti)neutrinos from other sources at SK site [57].

An upper limit of 70 cm^{-2} s^{-1} is set for the ν_e component of SRN flux in the energy range 22.9–36.9 MeV [81].

KamLAND and Borexino

Both KamLAND and Borexino are liquid scintillator detectors, which search $\bar{\nu}_e$'s via the inverse beta decay reaction. KamLAND searches both SRN and solar $\bar{\nu}_e$ in the energy range 8.3–30.8 MeV using 4.54 kton·year data. The upper limit on solar $\bar{\nu}_e$ flux is 90 cm^{-2} s^{-1} above 8.3 MeV, corresponding to 5.3×10^{-5} conversion probability which is the current best limit on solar $\bar{\nu}_e$ flux. Assuming Ando LMA model, the upper limit for SRN is found to be 139 cm^{-2} s^{-1} [79].

Borexino has obtained an upper limit for solar $\bar{\nu}_e$ flux of 760 cm^{-2} s^{-1}, which corresponds to a limit on $\nu_e \rightarrow \bar{\nu}_e$ conversion probability of 1.3×10^{-4} [82].

Super-Kamiokande-I/II/III

In 2003, the Super-Kamiokande collaboration reported a very stringent limit on SRN flux based on SK-I data, which reads [83]:

$$\phi_{\bar{\nu}_e}(E_{\bar{\nu}_e} > 19.3\,\mathrm{MeV}) < 1.2\,\mathrm{cm}^{-2}\,\mathrm{s}^{-1}. \tag{1.79}$$

The analysis threshold is then lowed to 17.3 MeV, mainly due to improvement on the spallation cut. Combining with SK-II/III data, the new limit becomes somewhat less constraining [84]:

$$\phi_{\bar{\nu}_e}(E_{\bar{\nu}_e} > 17.3\,\mathrm{MeV}) < 2.8 - 3.0\,\mathrm{cm}^{-2}\,\mathrm{s}^{-1}. \tag{1.80}$$

Note that the SK limit is already encouragingly close to theoretical predictions. Indeed, adding neutron tagging capability is mainly motivated by the search of SRN.

A search of solar $\bar{\nu}_e$ was also conducted in the energy range 8–20 MeV (visible energy) using SK-I data. This search is obscured by the huge spallation background and a rather poor limit of 0.8% was set on the $\nu_e \to \bar{\nu}_e$ conversion probability [85].

Chapter 2

Super-Kamiokande Detector

2.1 Detection Methodology

A charged particle that passes through a medium emits Cherenkov light when it moves faster than the speed of light in that medium, i.e.

$$v_{\text{particle}} > c/n(\lambda) \tag{2.1}$$

where c is the speed of light in vacuum, n is the index of refraction and λ is the wavelength of the photon. The refraction index n in general decreases slightly with increasing λ and is ∼1.33 for pure water. Formula (2.1) defines the minimum energy to generate Cherenkov radiation for a particle with mass m as

$$E_{\text{thr}} = \frac{m}{\sqrt{1-(1/n)^2}}. \tag{2.2}$$

Cherenkov photons are emitted in a cone with opening angle defined by

$$\cos\theta_C = \frac{1}{\beta n(\lambda)} \tag{2.3}$$

For ultra-relativistic particles ($\beta \approx 1$), $\theta_C \approx 42^\circ$. The number of photons emitted per unit wavelength per unit length of radiator is given by

$$\frac{d^2N}{d\lambda dx} = \frac{2\pi z^2\alpha}{\lambda^2}\left(1 - \frac{1}{\beta^2 n^2(\lambda)}\right) \tag{2.4}$$

where z is particle charge in unit of e, α is the fine structure constant. In the SK detector, Cherenkov photons are detected by photomultiplier tubes whose typical sensitivity ranges from 300 nm to 600 nm. Integrating (2.4) over λ gives

$$\frac{dN}{dx} = 2\pi z^2 \sin^2\theta_C \int_{\lambda_1}^{\lambda_2} \frac{d\lambda}{\lambda^2} = 760\, z^2 \sin^2\theta_C \,\text{photons/cm} \tag{2.5}$$

For an ultra-relativistic particle with unit charge, about 340 Cherenkov photons are emitted per cm. Note the energy loss due to Cherenkov radiation is rather small compared to the collision loss. Take $\lambda = 400$ nm, for example, the radiated energy is $E_{\rm rad} = \frac{dN}{dx} \times hc/\lambda \approx 1 \times 10^{-3}\,\text{MeV/cm}$, while the minimum ionization of a charged particle in water is about 2 MeV/cm.

2.2 Detector Overview

Super-Kamiokande is a water Cherenkov detector located under Mt.Ikenoyama in Gifu Prefecture, Japan. The mean overburden is 1000 m of rock, or 2700 meter-water-equivalent, reducing the comic ray muon rate to ∼2 Hz. The SK detector consists of a cylindrical stainless-steel tank with a diameter of 39.3 m and a height of 41.4 m. A PMT support structure of thickness 55 cm divides the tank into two optically isolated volumes: an inner detector (ID) and an outer detector (OD). The ID has dimensions 33.8 m (diameter) by 36.2 m (height) and is viewed by 11,146 inward-facing 50 cm PMTs giving ∼40% photo coverage. The OD is instrumented with 1185 outward-facing 20 cm PMTs. A schematic view of the SK detector is shown in Fig. 2.1.

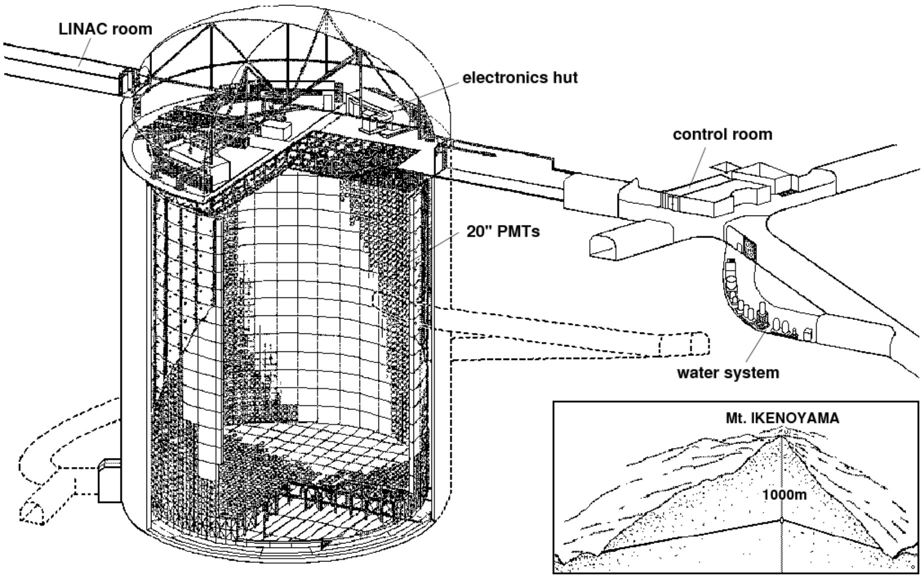

Figure 2.1: Schematic view of the Super-Kamiokande detector.

The OD volume has a thickness of ∼2 m, serving as an active veto for incoming charged particles and a passive shield for neutron and γ rays from surrounding rock. To further reduce ambient background, it is required that the event vertex should be at least 2 m away from the ID wall, defining the fiducial volume (FV) used for data analysis as 22.5 kton.

2.3 Photomultiplier Tubes (PMTs)

The 50 cm PMT was originally developed by the Hamamatsu Photonics Company and Kamiokande collaborators for use in the Kamiokande experiment. The model (Hamamatsu R3600) used in SK was improved in order to get better timing resolution and have better separation from dark current for single photoelectron [86]. Fig. 2.2 shows the structure of the 50 cm PMT. The photocathode material is bialkali (Sb-K-Cs) which has a sensitive region of 300-600 nm and the quantum efficiency peaks at 360-400 nm, as shown in Fig. 2.3. A good time resolution is critical to have better vertex resolution for low energy events. For single photoelectron the transit time spread is about 2.2 ns. The desired 1 p.e. peak can be clearly seen in Fig. 2.4, where the peak close to zero ADC count is due to the dark current.

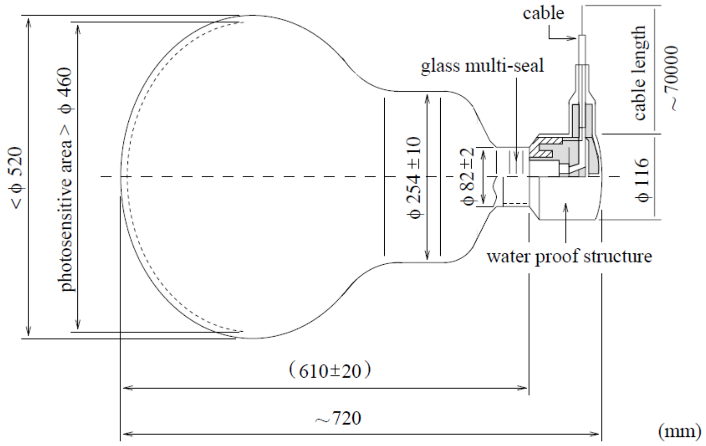

Figure 2.2: Schematic view of the 50 cm PMT.

The 50 cm PMTs are operated with a gain of 10^7 at a supply of high voltage ranging from 1700 to 2000 V. To minimize the geomagnetic field effect on PMTs, 26 sets Helmholtz coils are arranged in SK tank to reduce the geomagnetic filed down to 50 mG. The average dark noise rate at 0.25 pe threshold is about 3.5 kHz for SK-I. After the accident in 2001 when half of the PMTs were destroyed from the shock wave induced by a single PMT implosion, all ID PMTs are protected by acrylic covers and FRP cases. Although the acrylic covers have good transparency, the dark noise in SK-IV

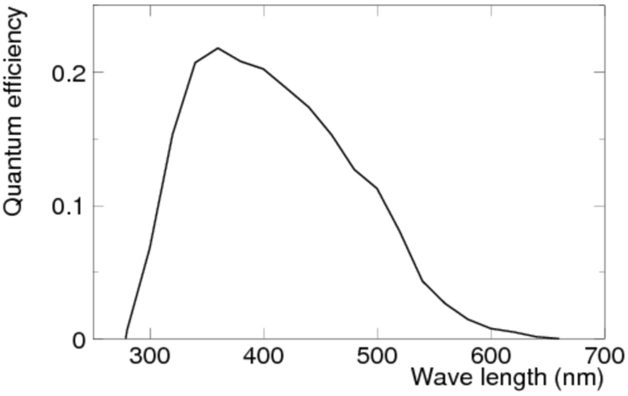

Figure 2.3: The quantum efficiency of the 50 cm PMT as a function of wavelenth.

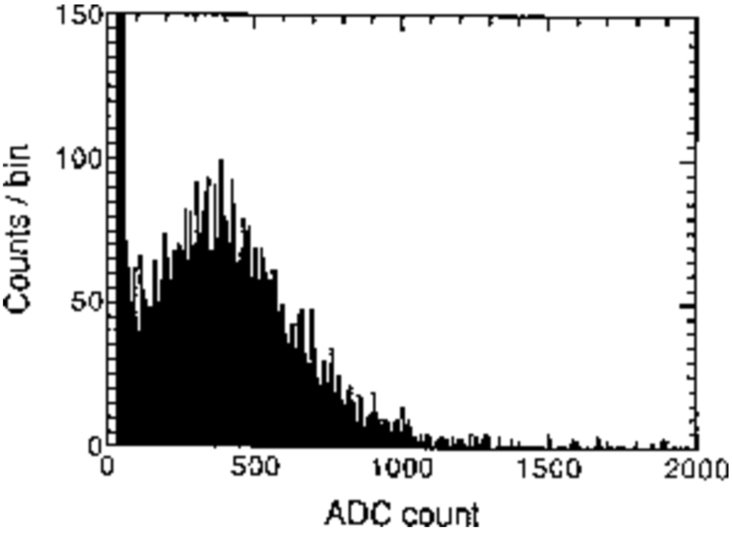

Figure 2.4: Single photoelectron pulse height distribution.

is increased compared to SK-I due to additional radioactivities from the FRP cases.

2.4 Electronics and Data Acquisition System

In August 2008, the SK electronics and data acquisition (DAQ) system were upgraded. The new system has a larger charge dynamic range and can handle a larger event rate. In addition, every hit is recorded and all hit data are filtered with software trigger, where complex triggers can be implemented. The new electronics and DAQ can enhance the physics of the SK experiment.

2.4.1 Electronics

PMT signals are processed by the newly developed front-end electronics QBEE (QTC Based Electronics with Ethernet). The primary functions of QBEE are to record the integrated charge and arrival timing of each PMT signal and send data to online PCs. Signals from 24 PMTs are fed to one QBEE board. Table 2.1 lists the basic specification of QBEE. Compared to the previous one, the new electronics has a larger charge dynamic range and better data transfer capability.

Table 2.1: Specification of QBEE [87].

Number of Inputs	24
Processing speed of QTC	about 900 ns/cycle
Number of ranges	3 (small, medium, large)
Discriminator	-0.3 to -14 mV (small range)
Charge dynamic range	0.2 to 2500 pC
Charge resolution	about 0.2 pC (small range)
Charge linearity	$< 1\%$
Timing resolution	0.3 ns (2 pC input) $<$0.2 ns ($>$ 10 pC input)
Power consumption	< 1 W/ch

A new custom application-specific integrated circuit (ASIC), the high-speed charge-to-time converter (QTC), is developed for the PMT charge measurement [88]. The ASIC detects PMT signals and issues output timing signals whose width represents the integrated charge of the PMT signal. This ASIC has a wide dynamic range for charge measurements by offering three gain ranges (small, medium, large). Each QTC chip has three inputs and eight QTC chips are assembled in one QBEE board. The output of QTC is processed by the multi-hit Time-to-Digital converter (TDC) called ATM-3 [89]. The TDC measures the width of QTC output pulse by detecting the leading and trailing edges.

Digitized data of the width and arrival timing are sent from TDC to a FPGA called Data Sort Mapping (DSM). DSM makes for each hit a 6-byte cell containing charge, timing and input channel information. Outputs from DSM are sent to another FPGA, where the data are sorted and stored in a FIFO memory. The stored data are then sent to a network interface card when a request is received from the card. The capability of data transfer from QBEE to online PCs is improved by using Ethernet. The throughput is measured to be 11.8 MB/s per QBEE board.

2.4.2 Data Acquisition System

Fig. 2.5 shows the block diagram of the new DAQ system. Data from about 500 QBEE boards are sent to 20 front-end PCs as TCP packets. The frond-end PCs sort received data in time order and send them to 10 Merger PCs via 10-Gigabit Ethernet. In the Merger PCs, data blocks from 20 frond-end PCs in the same time region are sent to one process for event building. There are 40 event building processes running in parallel on 10 Merger PCs. Data from the front-end PCs are merged and sorted in time order again and scanned by the software trigger. Via Gigabit Ethernet, triggered events are sent to an Organizer PC where all data blocks are sorted in time order and written to the disk for further analysis.

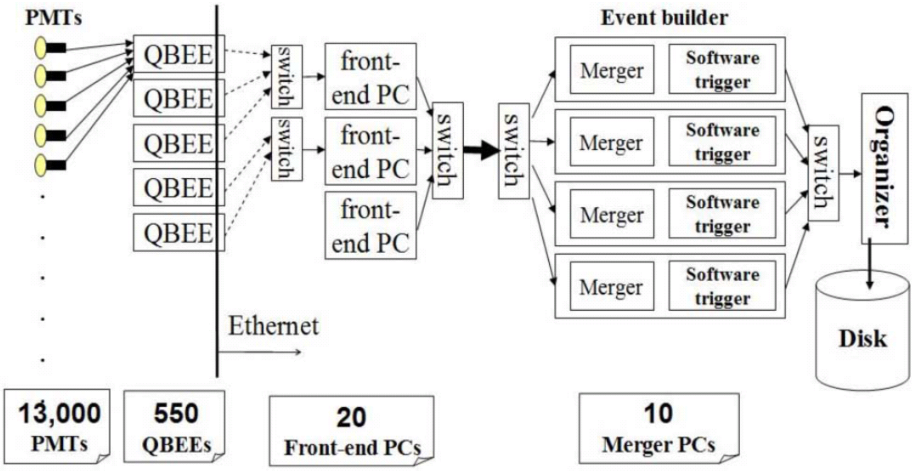

Figure 2.5: Block diagram of the data acquisition system for SK-IV [87].

The new DAQ system has been running stably 24 hours/day since its installation in September 2008. The increased throughput of the DAQ system enables SK to handle higher trigger rate, which is critical for detecting lower energy events. The new DAQ system can process data without loss up to 12 kHz trigger rate, which is much higher than the 4 kHz limit of the previous system. The new DAQ system also performs well for high rate bursts such as a nearby supernova neutrino explosion. The expected number of events from a supernova burst at the galactic center ($\sim$8.5 kpc away) at SK is about 10000. Tests show that the new DAQ system can process data without loss up to 6 millions events in the 10-second time window. The bottleneck of the new DAQ system is the disk writing speed of the Organizer PC, which has a limit of about 50 MB/s.

2.4.3 Trigger

In the previous DAQ system, a hardware trigger (HITSUM) was implemented based on the number of PMT hits within a 200 ns time window. There were four types of major triggers: high energy (HE), low energy (LE), super-low energy (SLE) and outer detector trigger (OD) [90]. In addition, several external triggers were prepared for the calibration purpose. In the new DAQ system, the software trigger simulates the HITSUM trigger by counting the number of hits in a 200 ns sliding window. The trigger thresholds for SLE, LE, HE, OD are 34, 47, 50 and 22 hits, respectively.

The event width is 1.3 μs in SK-I/II/III. Events with LE/HE trigger in SK-IV have a width of 40 μs, ranging from -5 μs to 35μs. The wider event width is ideal for catching possible pre-activity (e.g. prompt γ-ray) and post-activity (e.g. decay electron). The width of SLE-only events in SK-IV is 1 μs. Two new triggers are added in SK-IV primarily for the SRN study. A special high energy (SHE) trigger is issued if the number of ID hits exceeds 70, which corresponds to $\sim$10 MeV. If a SHE triggered event has no OD trigger, an After Trigger (AFT) is then issued to take 500 μs data without trigger threshold following that event. The combination of SHE and AFT trigger is used to detect the prompt positron and delayed 2.2 MeV γ resulted from the inverse beta decay reaction. The SHE threshold was lowered from 70 hits to 58 hits in September 2011 to study lower energy events that are accompanied by neutrons.

2.4.4 Monitoring System

A variety of tools are used to monitor the detector performance. A process called the “slow control” monitor watches the status of the HV systems and the temperatures of electronics crates. A histogram making process checks the data stream and make various distributions to check the PMT status and event trigger rates. The data transfer and offline data process are also monitored by a set of sophisticated software.

As part of the online monitor system, a new online display program is developed by the author of this thesis to visualize SK events in real time. The primary goals of this program are to provide visual investigations of the detector status and understandings of the physics of various events. A screenshot of the new event display is shown in Fig. 2.6. Graphical events fly on the big head-on screen at the rate about 1 Hz in the control room serve as the most direct and efficient way for shifters to monitor the DAQ system and the working status of PMTs in the detector.

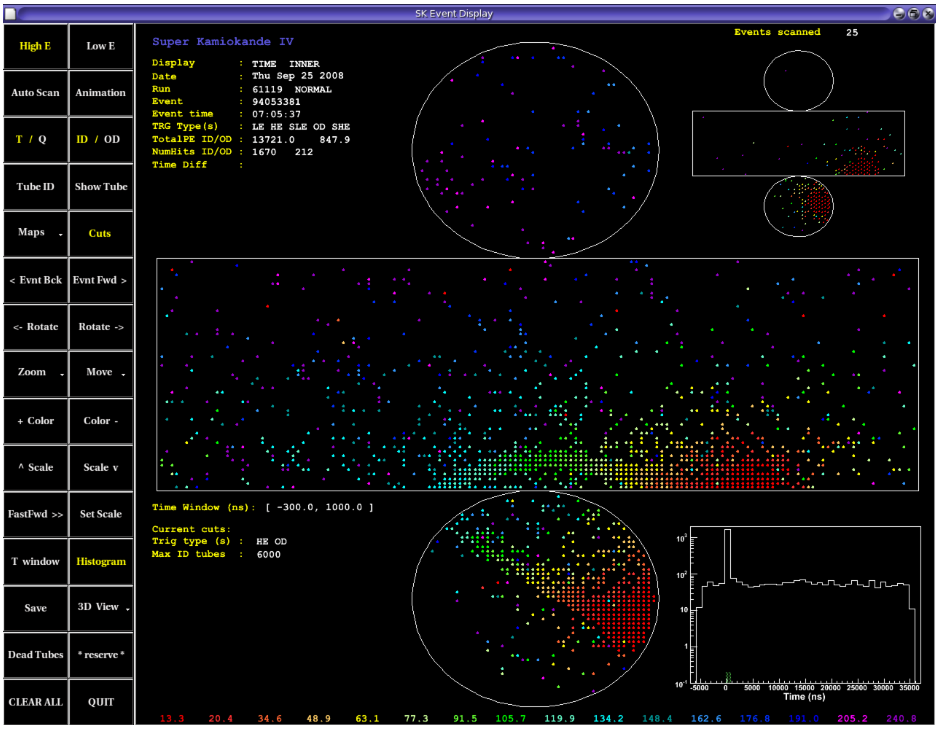

```
Super Kamiokande IV
Display       : TIME  INNER
Date          : Thu Sep 25 2008
Run           : 61119  NORMAL
Event         : 94053381
Event time    : 07:05:37
TRG Type(s)   : LE HE SLE OD SHE
TotalPE ID/OD : 13721.0    847.9
NumHits ID/OD : 1670   212
Time Diff     :
```

```
Time Window (ns):  [ -300.0, 1000.0 ]

Current cuts:
Trig type (s)  :  HE OD
Max ID tubes   :  6000
```

Figure 2.6: A screenshot of the new online event display.

2.5 Water and Air Purification Systems

To maximize the water transparency and minimize backgrounds arising from the natural radioactivity, the 50 ktons of purified water in the SK tank is continuously recirculated at the rate about 60 ton per hour through a multi-step purification system. A schematic view of the water purification system is shown in Fig. 2.7. The various process stages are described as follows:

- 1 μm filter:
  Removes dust and particles.
- Heat exchanger:
  Cool the water to reduce PMT dark noise and growth of bacteria.
- Cartridge polisher:
  Removes heavy ions.
- UV sterilizer:
  Kills bacteria.
- Rn-less air dissolve tank:
  Dissolve Rn-reduced air into the water to increase radon removal efficiency of the vacuum degasifier.
- Reverse osmosis:
  Further removes contaminants heavier than 100 molecular weight.
- Vacuum degasifier:
  Remove dissolved gases such as radon and oxygen from the water.
- Ultra filter:
  Remove small particles down to the size of 10 nm in diameter.
- Membrane degasifier:
  Further remove dissolved radon and oxygen gas.

Radon levels in the mine are relatively high, which typically reach 2000 Bq m^{-3} during the warm season and is about 200 Bq m^{-3} in the cold season. To reduce radon background, purified air is supplied to the experimental area from outside. Fresh air is continuously pumped in at approximately 10 m^3 min^{-1}, keeping the radon levels in the experimental area around 40 Bq m^{-3} throughout the year. Another super-radon-free-air system, as shown in Fig. 2.8, is used to keep the radon level less than a few mBq m^{-3} in the air between the top of water and the cover of the tank.

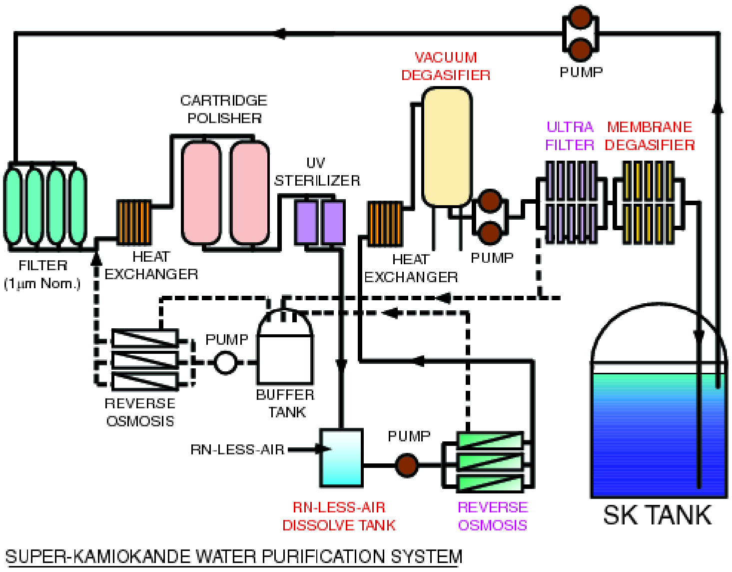

Figure 2.7: The water purification system at SK.

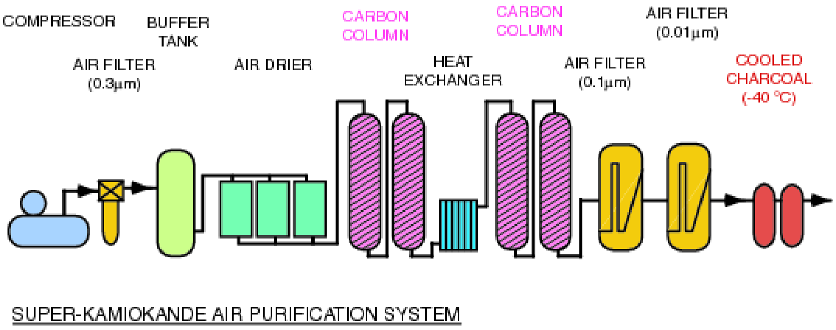

Figure 2.8: The air purification system at SK.

Chapter 3

Detector Calibration

Various calibrations are needed to gauge the performance of the Super-Kamiokande detector. This chapter summarizes the calibrations relevant for the data analysis in this thesis. More details on detector calibration can be found in Ref. [90].

3.1 PMT Calibration

The PMTs need to be calibrated in order to properly interpret the charge and timing recorded by each PMT. First of all, the high voltage supply for each PMT is adjusted to obtain a near-uniform response throughout the detector. Then the PMT gain is precisely measured for each PMT to correctly convert the ADC count to photo-electrons. The relative timing of PMTs is also corrected.

3.1.1 Absolute Gain

The global absolute gain (pC to p.e. conversion factor) is measured by using a Ni-Cf light source. Since the energy of γ-rays from the Ni-Cf source is only a few MeV, the resulting PMT hits are almost all due to single photons. The absolute gain is determined from the averaged charge distribution for single photo-electrons. The pC to p.e. factor is 2.645 pC/p.e. for SK-IV.

3.1.2 Relative Gain

The relative gain is measured using a laser system with a high and a low intensity light. The charge detected by the i-th PMT ($Q_{\mathrm{obs}}(i)$) in the high intensity data obey the following relation:

$$Q_{\mathrm{obs}}(i) \propto I_{\mathrm{high}}(i) \times \mathrm{QE}(i) \times G(i), \tag{3.1}$$

where $I_{\mathrm{high}}(i)$ is the light intensity seen by the i-th PMT, $\mathrm{QE}(i)$ is the PMT quantum efficiency and $G(i)$ is the relative gain. On the other hand, the hit times of each PMT in the low intensity data scale as:

$$M_{\mathrm{hit}}(i) \propto I_{\mathrm{low}}(i) \times \mathrm{QE}(i). \tag{3.2}$$

Taking the ratio of Eqn. (3.1) and Eqn. (3.2), one finds

$$G(i) = \frac{Q_{\mathrm{obs}}(i)}{M_{\mathrm{hit}}(i)} \times \frac{I_{\mathrm{low}}(i)}{I_{\mathrm{high}}(i)}, \tag{3.3}$$

where light attenuation and geometric effects are all canceled out. The measured relative PMT gain is shown in Fig. 3.1. Both the absolute and relative gain are used to convert the ADC count to p.e. in processing real data.

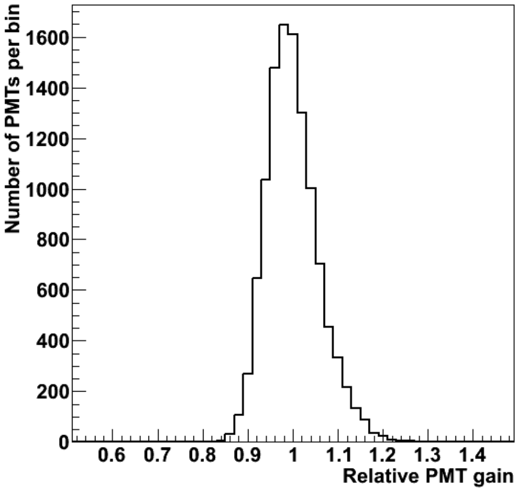

Figure 3.1: Measured relative PMT gain. The 1-σ spread is about 6%.

3.1.3 Timing

The relative timing of PMT hits is important for vertex reconstruction. The difference arises from variations in transit time and cable length of each PMT. It also depends on the observed charge due to the discriminator slewing effect.

The PMT relative timing is measured using a laser system. The N_2 laser beam is injected via an optical fiber into a diffuser ball, which is deployed at the center of the tank to produce diffuse light. The light intensity is changed using an optical filter to measure the PMT timing at various pulse heights. Fig. 3.2 shows a typical 2-D plot of PMT timing versus pulse height, which is referred to as a "TQ-map". A TQ-map is made for each PMT. With corrections according to the TQ-maps, the residual timing differences of PMT hits are used to determine the global timing resolution. This global timing resolution is an input for vertex reconstruction and Monte Carlo simulation. At single p.e. level, the timing resolution is about 3 ns.

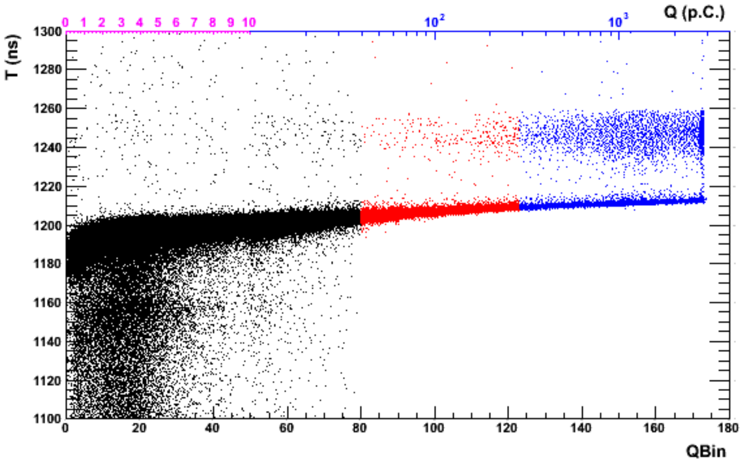

Figure 3.2: A typical 2-D plot of timing vs. charge, known as "TQ-map". The upper horizontal axis shows the PMT charge. The QBin in the lower horizontal axis is defined as: $\text{QBin} = 5 \cdot Q$ $(0 < Q < 10)$ or $\text{QBin} = 50 \cdot \log_{10} Q$ $(10 < Q < 3981)$. Hits in the lower left are due to scattered photons. Hits in the upper right are pre-pulses.

3.2 Water Transparency Measurement

Light absorption and scattering in water affect the number of Cherenkov photons that are detected by PMTs. Therefore, it's important to precisely determine the water transparency for accurate energy measurements. There are two ways to measure water transparency at SK. Firstly, the absorption and scattering parameters are separately measured using the N_2 laser. And secondly, the effective attenuation length is measured using the decay electrons from cosmic ray muons.

3.2.1 Laser Measurements

In terms of the absorption (α_{abs}) and scattering (α_{scat}) parameters, the light attenuation length is

$$L_{\text{atten}} = \frac{1}{\alpha_{\text{abs}} + \alpha_{\text{scat, sym}} + \alpha_{\text{scat, asym}}}, \tag{3.4}$$

where $\alpha_{\text{scat, sym}}$ includes Rayleigh scattering and the symmetric part of Mie scattering while $\alpha_{\text{scat, asym}}$ represents the asymmetric part of Mie scattering. A set of N_2 lasers of wavelengths 337, 375, 405, 445 and 473 nm are used to directly measure these parameters. The laser beam is vertically injected into the SK detector from the top via optical fibers. Each laser fires every 6 s during normal data taking period.

In such laser events, PMT hits at the bottom of the tank are due to direct light, while PMT hits on the barrel and the top are due to photons scattered in water or reflected by bottom PMTs and black liner sheets. The absorption and scattering parameters are studied using the total number of scattered photons and the distribution of the arrival-time of PMT hits. These parameters are tuned in the Monte Carlo so that the simulation matches the laser data. The absorption and scattering parameters determined in this way are then used to model the water property when generating physics Monte Carlo simulation. The water attenuation length calculated using Eqn. (3.4) is in agreement with the decay electron measurement described below.

3.2.2 Decay Electrons

Each day thousands of cosmic ray muons stop in the inner detector to produce decay electrons. These decay electrons can serve as a calibration sample to continuously monitor the water transparency. In order to have a pure sample of decay electrons, the following selection criteria are applied:

- The time difference ΔT between the stopping muon and the decay electron should satisfy: $3.0\mu s < \Delta T < 8.0\mu s$.
- The vertex of the electron must be reconstructed within the fiducial volume.
- The distance between the reconstructed electron vertex and the muon stopping point must be less than 250 cm.
- The number of PMT hits with residual time within 50 ns must be greater than 50.

These criteria selects ~700 $\mu - e$ decay events each day.

Using selected decay-e events, PMT hits are divided by the distance from the reconstructed decay-e vertex to each hit PMT. The water transparency is determined by fitting the number of PMT hits versus distance distribution. To remove the effects of noise hits and indirect light, only PMT hits within a corn of opening angle between $32^\circ \sim 52^\circ$ and with residual time within 50 ns are used. The amount of contribution from each PMT is corrected in the same way as that for the energy reconstruction (see section 4.3). To reduce statistical fluctuation, the water transparency given for each day is calculated using +/− one week data. The water transparency obtained by this method is shown in Fig. 3.3 for the SK-IV period. As discussed in section 4.3, this daily water transparency is an input parameter for the energy reconstruction.

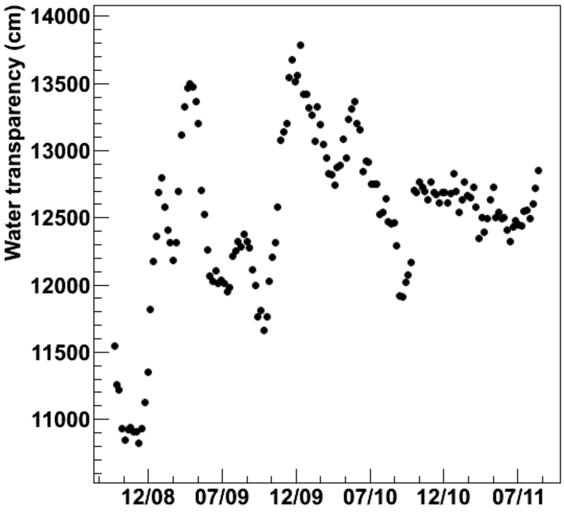

Figure 3.3: Water transparency of SK-IV measured from decay electrons.

3.3 Energy Calibration

Precise energy measurement is critical for low energy data analysis. Various techniques are used at SK to calibrate the absolute energy scale, its directional and position dependence and time variation.

3.3.1 LINAC

The absolute energy scale for low energy data analysis at SK is primarily determined by using an electron linear accelerator (LINAC). The LINAC is used to inject into the SK tank downward-going single mono-energetic electrons with energy up to ∼19 MeV. The beam energy is precisely measured to ±20 keV accuracy using a Germanium detector. The LINAC system and its performance is detailed in Ref. [91].

The LINAC data were taken in August 2009 and August 2010 during the SK-IV period. Each time data were taken at several positions and with several different energies at each position. The LINAC data are used to tune various parameters in the Monte Carlo. Fig. 3.4 shows the reconstructed energy of LINAC data with comparison to the Monte Carlo at one of the beam positions. Very good agreement is obtained for all tested beam energies.

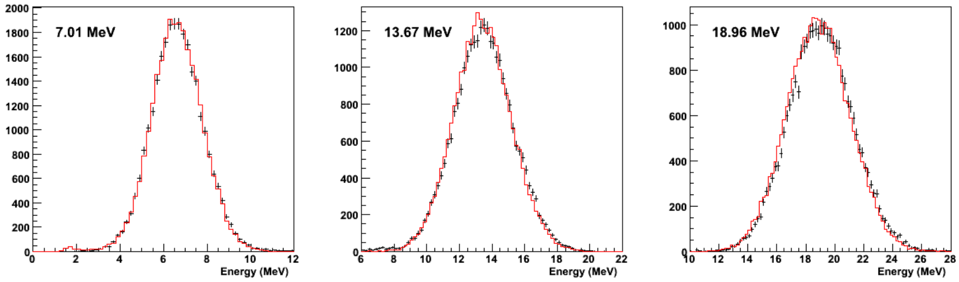

Figure 3.4: Distributions of reconstructed energy for LINAC data (cross) and MC (line) at the beam position (x,y,z)=(-388.9 cm, -70.7 cm, -6 cm). The LINAC data were taken in August 2010.

The LINAC calibration is responsible for converting the effective number of PMT hits (N_{eff}, see section 4.3) to the total energy. However, the LINAC data is only available in the downward-going direction and several fixed positions. Hence the correlation between N_{eff} and the energy can not be obtained directly from the LINAC data. Instead, the LINAC-tuned Monte Carlo is used to generate uniformly distributed events at several fixed energies. The mean value of N_{eff} is obtained for each energy by fitting the N_{eff} distribution with a Gaussian function. The correlation between N_{eff} and energy is then fit with a 4-th order polynomial function. The energy conversion function obtained in this way sets the absolute energy scale of the detector. The accuracy of the absolute energy scale is better than 1% as determined from LINAC data.

In addition to set the absolute energy scale, the LINAC data are also used to study the energy resolution, vertex resolution and angular resolution because LINAC events have known energy, position and direction. Details of these resolutions and their systematic uncertainties can be found in Ref. [91].

3.3.2 DT Generator

A deuterium-tritium (DT) neutron generator is used to cross check the absolute energy scale [92]. The generated neutrons are employed to create ^{16}N via the (n,p) reaction on ^{16}O in water. The decay of ^{16}N has a Q value of 10.4 MeV and is dominated by an electron, with a maximum energy of 4.3 MeV, coincident with a 6.1 MeV γ-ray. DT data is taken every a few months, and the reconstructed energy of DT events agrees with LINAC-tuned Monte Carlo better than 1%.

Since DT events are isotropic, the directional dependence of the energy scale can be checked using DT data. This directional dependence is found to be less than ±0.5%. Due to the better portability of the DT generator, DT data are taken at more positions than LINAC to study the position dependence of the energy scale. The radial and z-dependence of the energy scale is found to be less than ±0.5% and ±1%, respectively.

3.3.3 Decay Electrons

The energy of decay electrons from stopping cosmic ray muons follows the well known Michel spectrum. Therefore, decay electrons can be used to check the energy scale up to about 60 MeV. Taking into account effects due to μ^- capture by oxygen nuclei, the data can be reproduced by Monte Carlo with better than 2% accuracy.

In addition to determine the absolute energy scale, decay electrons are used to check the time variation of the energy scale. Using the same decay-e sample as that for water transparency measurement, the mean effective number of PMT hits N_{eff} is calculated for each 30 days period using the corrected water transparency. Fig. 3.5 shows the mean N_{eff} distribution for SK-IV. The energy scale is stable within ±0.5% during the operation of SK-IV.

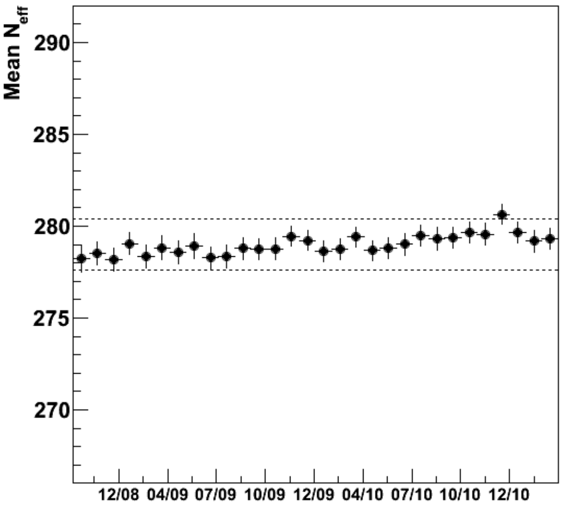

Figure 3.5: Mean N_{eff} of decay electrons. The dashed lines indicate ±0.5% deviation from the average.

Chapter 4

Event Reconstruction

All events that meet the software trigger conditions and have less than 1000 PMT hits are applied with low energy reconstruction tools. The primary reconstructed quantities are the vertex, direction and energy of the event. Events with more than 1000 photo-electrons are considered to be cosmic ray muons [1] and are reconstructed with muon track fitters. Reconstructed muons are used to identify spallation events. In order to distinguish electrons from other particles, Cherenkov angle is calculated after events passing certain selection criteria.

4.1 Vertex Reconstruction

Low energy electrons and positrons can only travel a short distance (e.g. ~20 cm at 50 MeV), and thus the Cherenkov light is considered as emitted from a point source. Since for low energy events at Super-Kamiokande, most PMT signals are due to single photon hits, little information about the distance from PMT hits to the source can be extracted from PMT charge. Therefore, the reconstruction of vertex for low energy events relies entirely on the timing of PMT hits. Among the several existing vertex fitters, BONSAI [93] has the best vertex resolution and lowest misfit rate and is used for vertex reconstruction in this thesis.

The BONSAI is a maximum likelihood fit to the timing residuals of the hit PMTs. The timing residual is defined as:

$$\Delta t = t - \mathrm{tof}(\vec{v}) - t_0, \tag{4.1}$$

where t is the PMT hit timing, $\vec{v}$ and t_0 are the vertex and Cherenkov light emission time under testing and tof is the time-of-flight (TOF) from the

---

[1] The atmospheric neutrino event rate is about 10 events per day.

testing vertex to the hit PMT. The signal probability density function of Δt used in the fit is taken from LINAC calibration data and the PMT dark noise is assumed to be flat. The likelihood constructed from the Δt distribution is then maximized to give the reconstructed vertex. The BONSAI vertex resolution is ~70 cm for 10 MeV electrons. BONSAI also returns a goodness value which can be used to evaluate the quality of the fit.

4.2 Direction Reconstruction

The direction of an electron can be reconstructed utilizing the Cherenkov ring pattern. This is accomplished by maximizing the following likelihood function:

$$L(\vec{d}) = \sum_{i}^{N_{20}} \log(f(\cos\theta_{\text{dir},E})_i) \times \frac{\cos\theta_i}{a(\theta_i)}, \tag{4.2}$$

where N_{20} is the number of PMT hits within a 20 ns window around $\Delta t = 0$ while $f(\cos\theta_{\text{dir},E})$ is the expected distribution of the opening angle between the particle direction $\vec{d}$ and the vector from the reconstructed vertex to the hit PMT. The distribution of $f(\cos\theta_{\text{dir},E})$ is obtained from MC for various energies. It peaks around 42 degree but expands a wide range because of the multiple scattering. The factor $\cos\theta_i/a(\theta_i)$ corrects for the PMT acceptance, where θ_i is the opening angle between the vector from the reconstructed vertex to the i-th hit PMT and the vector normal to the PMT surface. Enq. (4.2) is maximized by scanning various directions. The best solution that gives the maximum likelihood is chosen as the reconstructed direction. For a 10 MeV electron, the angular resolution is about 25 degree.

4.3 Energy Reconstruction

The basic idea behind the energy reconstruction is that the energy deposited by a charged particle is approximately proportional to the number of generated Cherenkov photons. For low energy events, it is also proportional to the number of PMT hits since in such case most PMTs are hit by single photons. Before converting the number of PMT hits to the energy, several corrections should be applied to get an effective number of hits, which is defined as:

$$N_{\text{eff}} = \sum_{i=1}^{N_{50}} \left\{ (X_i - \epsilon_{\text{tail}} - \epsilon_{\text{dark}}) \times \frac{N_{\text{all}}}{N_{\text{norm}}} \times \frac{R_{\text{cover}}}{S(\theta_i, \phi_i)} \times \exp(\frac{r_i}{\lambda(\text{run})}) \times G_i(t) \right\} \tag{4.3}$$

where N_{50} is the number of PMT hits with residual time within a 50 ns window. Most dark noise is filtered out by using this narrow time window. The quntities in Eqn. (4.3) are explained as follows:

- **Occupancy**
  The assumption of single photon per PMT breaks down at higher energies. If a PMT detects multiple photons, it is likely that many PMTs surrounding this PMT are also hited. X_i is an occupancy used to estimate the effect of multiple photo-electrons for the i-th PMT and is defined as:
  $$X_i = \begin{cases} \frac{\log \frac{1}{1-x_i}}{x_i}, & x_i < 1 \\ 3.0, & x_i = 1 \end{cases} \tag{4.4}$$
  where x_i is the ratio of the number of hit PMTs to the total number of PMTs in a 3×3 patch around the i-th hit PMT.

- **Late hits**
  Some Cherenkov photons can be scattered or reflected, and thus fall outside the 50 ns window. This effect is corrected by the term ϵ_{tail}.

- **Dark noise**
  The contribution of dark noise ϵ_{dark} is estimated from the total number of operating PMTs and dark rate of each PMT, and is subtracted from occupancy.

- **Bad PMTs**
  The second factor in Eqn. (4.3) corrects for bad PMTs, where N_{all} is the number of total PMTs and is 11129 in SK-IV, an N_{norm} is the number of properly operating PMTs.

- **Photo-cathode coverage**
  The third factor accounts for the effective photo coverage, which is dependent on the incident angle of the photon to the PMT.

- **Water transparency**
  The fourth factor corrects for water transparency variation, where r_i is the distance from the reconstructed vertex to the i-th hit PMT, and λ is the measured water transparency.

- **PMT gain**
  The last factor corrects time dependent PMT gain at the single photon level.

Finally, the total energy of an event is calculated as a function of N_{eff}. As discussed in section 3.3.1, the energy conversion is precisely calibrated using the LINAC data and the accuracy of the absolute energy scale is better than 1%. The energy resolution is about 14% for 10 MeV electrons. It should be noted that the energy reconstruction described here always assumes the particle is either an electron or a positron. This energy reconstruction algorithm does not apply to other particles. For example, a muon with momentum $p = 200\,\mathrm{MeV}/c$ can be reconstructed as if it was a 25 MeV electron. So unless otherwise stated, all energy values quoted in this thesis refer to total electron equivalent energy.

4.4 Muon Fitting

Most low energy events above 8 MeV observed in SK are spallation products induced by cosmic ray muons. Such events can be rejected by searching for spatial and temporal correlations with proceeding muons. Therefore, it's critical to precisely reconstruct the muon tracks.

Muboy

All events with more than 1000 photo-electrons are fitted using a software called Muboy. Muboy can fit not only a single muon track but also multiple muon tracks (assumed to have parallel track directions). Muons successfully fit by Muboy are classified into the following categories: single through-going muons, stopping muons, multiple muons and corner clippers. For multiple muons, up to 10 tracks can be fit; there may have only one track if too few hits are left after removing the hits closely associated with the first track (but classification is still multiple muons). Muboy also returns a goodness value to evaluate the quality of fit. The muon type classification and fit goodness are very useful in determining spallation (see section 9.3). Detailed descriptions of the algorithm and performance of Muboy can be found in Refs. [94, 95].

SK-IV events have a wide width. When an incident muon happens to be within the time window of another triggered event (except SLE only event), it will not register a trigger. There are a few hundreds of such untagged muons per day in SK-IV data. It is important to identify these untagged muons so that decay electrons and spallations resulting from these muons can be correctly identified. To locate untagged muons offline, the software trigger is applied again to each event to search for a muon candidate (with HE and OD trigger). The untagged muons are then extracted for processing with Muboy.

BFF

In rare cases, the Muboy fit result is not reliable as indicated by the poor goodness value. An alternative muon fitter is developed to refit the single through-going muons for which Muboy reports a bad goodness (< 0.4). This new fitter is called Brute Force Fitter (BFF). It simply performs a grid search for the entry and exit points in the inner surface of the detector, and hence is rather slow. BFF can improve the power of the spallation cut by correctly refitting ~75% of the muons that poorly fit by Muboy. More details about BFF can be found in Ref. [96].

dE/dx

After muon tracks are fit, Cherenkov light emission per unit track length, dE/dx, is also calculated. This is done by matching the light seen by each PMT to a location along the muon track using timing information. The dE/dx of the muon track is histogrammed in 50 cm bins. It is found that muons tend to have a peak in the dE/dx distribution at where the spallation occurred.

4.5 Cherenkov Angle Reconstruction

For the low energy analysis at SK, particle identification (PID) is mainly done by studying the opening angle of the Cherenkov ring caused by a charged particle. Electrons (or positrons) above the analysis threshold are ultra-relativistic particles and have a Cherenkov opening angle around 42°. Heavier particles such as muons and pions are not ultra-relativistic and would have a smaller opening angle as determined by Eqn. (2.3). In addition, PMT hits induced by mutiple γ-rays tend to appear isotropically in the detector, where no clear Cherenkov ring can be identified. The reconstructed Cherenkov angle can be used to reject muons, pions and γ-rays.

The Cherenkov opening angle is reconstructed using 3-hit combinations. Each set of 3 PMT hits uniquely defines a cone with a particular opening angle. The resulting distribution of opening angles evaluated from all combinations should peak at the opening angle of the Cherenkov cone. In order to minimize the effects of noise hits, only PMT hits with residual time within a 15 ns window are considered. A typical opening angle distribution for an electron is shown in Fig. 4.1 in black line. The peak of this distribution is taken as the Cherenkov angle of the event. The opening angle distributions do not have a well defined shape and it's impractical to apply a fit for all events. Instead, the peak is located using a sliding 7-bin. The Cherenkov opening angle is determined to be 45.9° for this event. Fig. 4.2 shows the event display for this electron, where the big circle shows the expected Cherenkov ring assuming an opening angle of 42° (unless otherwise stated, rings appear in displays are shown under this assumption). It can be seen that the actual PMT hit pattern matches the expected Cherenkov ring quite well.

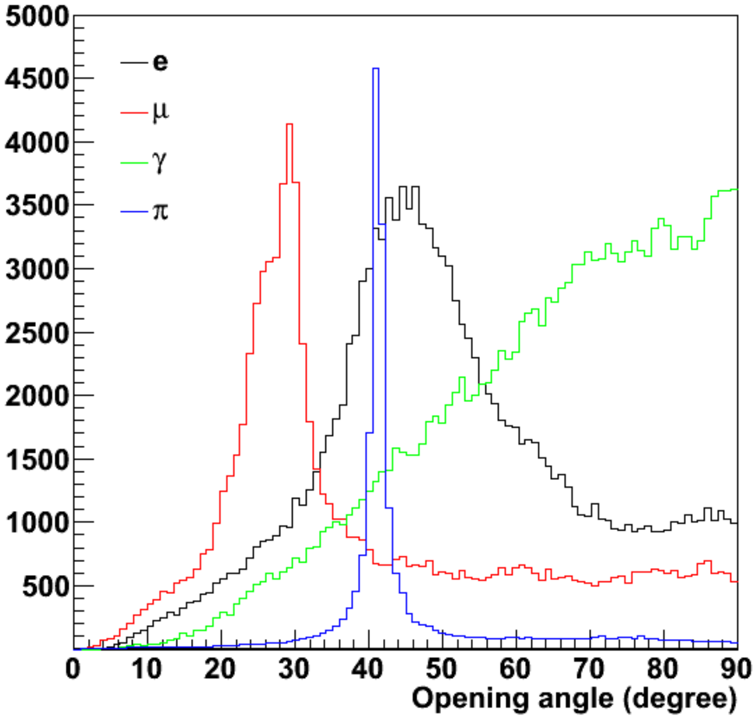

Figure 4.1: Example of distributions of opening angle from 3-hit combinations for various particles. Bin entries of the red and blue histograms are shrinked by a factor of 2 and 10, respectively, for better visualization. Event displays are shown for these events in Fig. 4.2–4.5.

A typical opening angle distribution for a muon is shown in Fig. 4.1 in red line. The Cherenkov opening angle determined for this event is 27.9°. Event display for this muon is shown in Fig. 4.3, which exhibits a significant deviation from an electron ring. A typical opening angle distribution for a γ-ray event is shown in Fig. 4.1 in green line. The Cherenkov opening angle determined for this event is 87.3°. Such events tend to have isotropic PMT hits, as shown in Fig. 4.4.

The reconstructed Cherenkov opening angle value is used to reject muons and pions with relatively low momentum and γ-rays, see section 9.6. In addition, the width of the opening angle distribution can be used to reject another type of event: pions with higher momentum. In some cases, atmospheric neutrino induced pions are absorbed by oxygen nuclei after emitting some Cherenkov light and can be reconstructed as a low energy event. If the momentum of the pion is high enough, the reconstructed Cherenkov angle is close to 42° and hence can not be distinguished from an electron. However, unlike the fuzzy rings caused by electrons, pion rings are in general very sharp (see Fig. 4.5). A sharper ring corresponds to a narrower peak in the opening angle distribution. A typical opening angle distribution for such a pion is shown in Fig. 4.1 in blue line. Although its peak value is similar to an electron, the width of the peak is much smaller than that of an electron. To quantify this characteristic, a pion likelihood is calculated as the following:

$$\pi_{\text{like}} = \frac{\#\text{entries} \pm 3^\circ \text{ from peak}}{\#\text{entries} \pm 10^\circ - \#\text{entries} \pm 3^\circ}. \tag{4.5}$$

Events with large π_{like} value are considered to be pion events, see section 9.8.

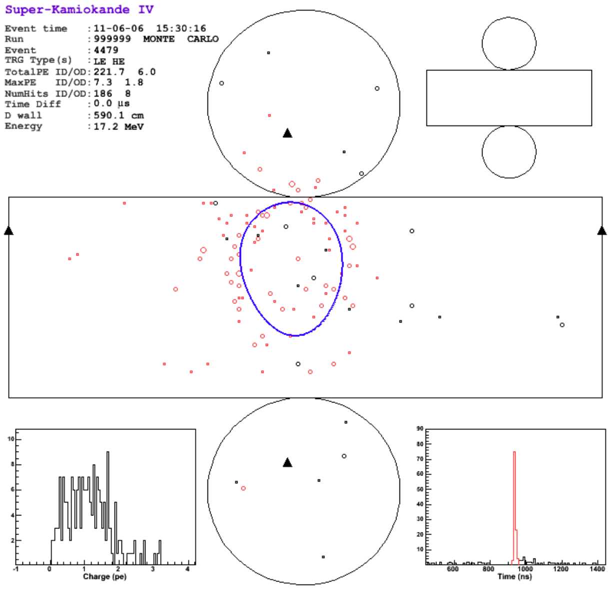

```
Super-Kamiokande IV
Event time     :11-06-06  15:30:16
Run            :999999  MONTE  CARLO
Event          :4479
TRG Type(s)    :LE HE
TotalPE ID/OD:221.7  6.0
MaxPE   ID/OD:7.3  1.8
NumHits ID/OD:186  8
Time Diff      :0.0 µs
D wall         :590.1 cm
Energy         :17.2 MeV
```

Figure 4.2: A typical electron MC event. The reconstructed energy is 17.2 MeV. The circle shows the expected Cherenkov ring for a ultra-relativistic particle.

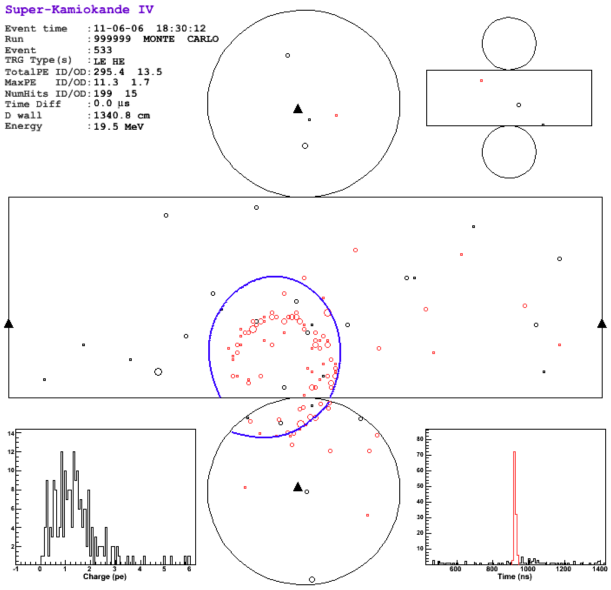

Figure 4.3: A typical muon MC event. The muon momentum is 185.8 MeV/c and the reconstructed energy is 19.5 MeV.

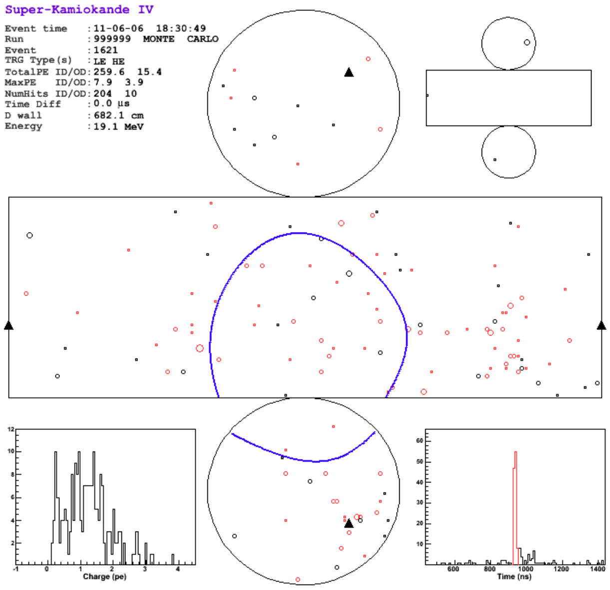

Figure 4.4: A typical isotropic MC event. The reconstructed energy is 19.1 MeV.

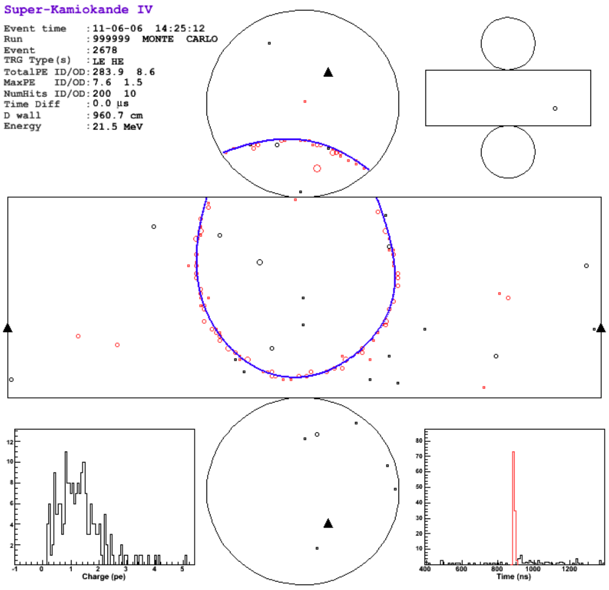

Figure 4.5: A typical pion MC event. The pion momentum is 402.9 MeV/c and the reconstructed energy is 21.5 MeV. This pion is absorbed by an oxygen nucleus before depositing all of the energy.

Chapter 5

Event Simulation

Monte Carlo simulated samples are used to evaluate the data reduction efficiency and to understand the energy spectra of signal events. In addition, the simulated samples can be used to precisely predict the expected number of events at SK, including the detector response.

5.1 Detector Simulation

The Super-Kamiokande detector simulation package, SKDETSIM, is based on GEANT 3.21. SKDETSIM models the emission of Cherenkov photons, the propagation of these photons in water and the detector response. In SKDETSIM, some parameters such as the water attenuation length and PMT timing resolutions are specifically tuned to reproduce the calibration data [97, 98].

5.2 Neutrino Interaction Simulation

The inverse beta decay reaction chain has been theoretically studied in details for its special importance in low energy neutrino experiments. In this thesis, we adopt Strumia and Vissani's calculation for $\bar{\nu}_e p \rightarrow e^+ n$ cross-section [99]. In the simulation, we also take into account the angular distribution of the outgoing positron, which is in particular relevant for the solar $\bar{\nu}_e$ search. Vogel and Beacom's first order approximation [100], which is accurate in the energy range of interest, is used for the angular distribution. Fig. 5.1 shows the angular distributions for various incident neutrino energies.

The outgoing positron energy is strongly correlated with the $\bar{\nu}_e$ energy. At zeroth order in $1/M$ (M is the average nucleon mass), the positron energy

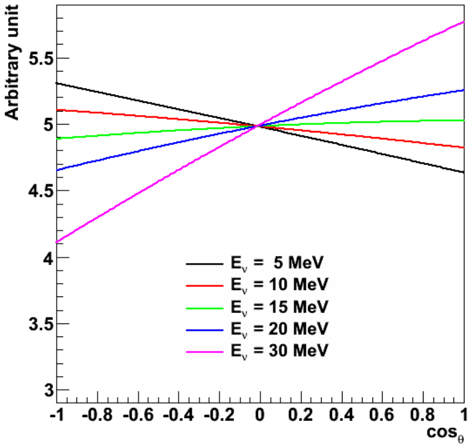

Figure 5.1: Distribution of the positron scattering angle in the inverse beta decay reaction.

is

$$E_e^{(0)} = E_\nu - \Delta, \tag{5.1}$$

where $\Delta = M_n - M_p \approx 1.293$ MeV. This simple relation is used in previous SK SRN searches. In this thesis, we use Vogel and Beacom's first order approximation because it's more accurate at relatively high energies ($E_\nu \gtrsim 20$ MeV). At the first order in $1/M$, the positron energy has a weak dependence on the scattering angle and is

$$E_e^{(1)} = E_e^{(0)} \left[1 - \frac{E_\nu}{M}(1 - v_e^{(0)} \cos\theta)\right] - \frac{y^2}{M}, \tag{5.2}$$

where $v_e^{(0)} = p_e^{(0)}/E_e^{(0)}$ is the velocity of the positron, and $y^2 = (\Delta^2 - m_e^2)/2$ [100]. Eqn. (5.2) is accurate to ~1% at $E_\nu = 60$ MeV.

To simuilate inverse beta decay, we first use the flux and IBD cross-section to give the interaction rate spectrum

$$dN_{\mathrm{IBD}} = N_{p,\,\mathrm{full}} \times \tau_{1\mathrm{y}} \times f(E_\nu) \times \sigma(E_\nu) dE_\nu, \tag{5.3}$$

where N_{IBD} is the number of inverse beta decay events, $N_{p,\,\mathrm{full}}$ is the number of free protons in the SK full inner volume, $\tau_{1\mathrm{y}}$ is the time of one year, $f(E_\nu)$ is the differential flux and $\sigma(E_\nu)$ is the IBD cross-section. The total number of events in the SK full inner volume in one year is given by

$$N_0 = \int_0^\infty dN_{\mathrm{IBD}} \tag{5.4}$$

Then the generation of IBD MC events proceeds as follows:

1. Generate E_ν according to Eqn. (5.3).
2. Generate the scattering angle of the outgoing positron. For a given E_ν, make angular distribution $d\sigma/d\cos(\theta)$ according to the first order approximation formula of Vogel and Beacom [100]. Then randomly generate a $\cos(\theta)$ according to the distribution of $d\sigma/d\cos(\theta)$.
3. Calculate the positron energy using Eqn. (5.2).
4. Generate a vertex randomly distributed in the SK full inner volume.
5. Generate the event direction according to the Sun position and $\cos(\theta)$. This direction is only relevant for the solar $\bar{\nu}_e$ search.
6. Attach time information to this event to take into account the time variation of water transparency.
7. Feed the event information into SKDETSIM to simulate the detector response.

The simulated data are reconstructed with the same tools that are applied to the real data. Let N_1 be the total number of generated MC events, and N_2 be the number of events that are reconstructed in the fiducial volume and with an energy between $E_{\rm low}$ and $E_{\rm up}$. Then the expected number of signal events from the total flux $F(\ F = \int_0^\infty f(E_\nu)dE_\nu)$ is

$$N_{\rm exp} = \frac{N_0}{N_1} \times N_2 \ / \ 22.5\,{\rm kton} \ / \ {\rm year} \ (E_{\rm low} < E_{e^+} < E_{\rm up}). \tag{5.5}$$

Eqn. (5.5) can be used to predict the expected number of events at SK, or to convert the number of events back to flux.

5.2.1 Supernova Relic Neutrinos

For the purpose of evaluation, we consider the Ando LMA model and HBD 6 MeV model. The predicted event rate from these models are shown in Fig. 5.2.

Fig. 5.3 shows the generated and reconstructed positron energy spectrum for the Ando LMA model. The expected annual number of events in the energy range 12 MeV $< E_{e^+} <$ 30 MeV (see chapter 9) is calculated from Eqn. (5.5) and is shown is Table 5.1.

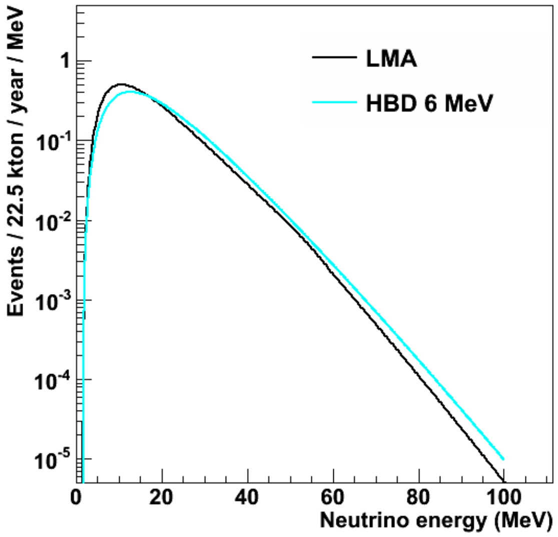

Figure 5.2: SRN $\bar{\nu}_e$ induced event rate for the theoretical models.

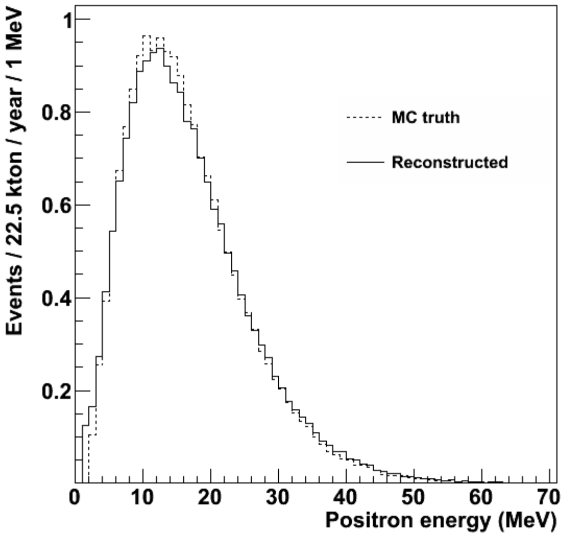

Figure 5.3: Positron energy spectrum predicted by the LMA model.

Table 5.1: Expected number of SRN events in 22.5 kton·year.

SRN model	Total flux (/cm^2/sec)	12 MeV $< E_{e^+} <$ 30 MeV
LMA	28.8	4.15
HBD 6 MeV	21.8	4.36

5.2.2 Solar Anti-neutrinos

For solar $\bar{\nu}_e$'s, we assume an undistorted ^{8}B neutrino energy spectrum. The total ^{8}B neutrino flux is taken from BP04 predictions [67]. The ^{8}B neutrino energy spectrum is adopted from the Winter06 measurement [101]. Assuming 1% $\nu_e \rightarrow \bar{\nu}_e$ conversion probability, the expected annual event rate in SK full inner volume is shown in Fig. 5.4.

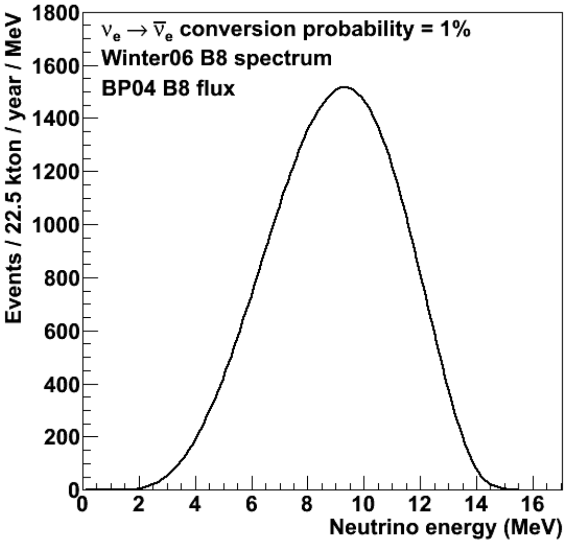

Figure 5.4: Annual event rate for possible solar $\bar{\nu}_e$ in SK full inner volume, assuming 1% $\nu_e \rightarrow \bar{\nu}_e$ conversion probability.

Fig. 5.5 shows the generated and reconstructed positron energy spectrum. Note the significant modification of the energy tail by the detector response. The expected annual number of events in the energy range 12 MeV $< E_{e^+} <$ 20 MeV is calculated from Eqn. (5.5) and is shown is table 5.2.

Table 5.2: Expected number of solar $\bar{\nu}_e$ events in 22.5 kton·year, assuming $\nu_e \rightarrow \bar{\nu}_e$ conversion probability is 1%.

SSM	Total flux (/cm^2/sec)	12 MeV $< E_{e^+} <$ 20 MeV
BP04	5.79×10^6	503

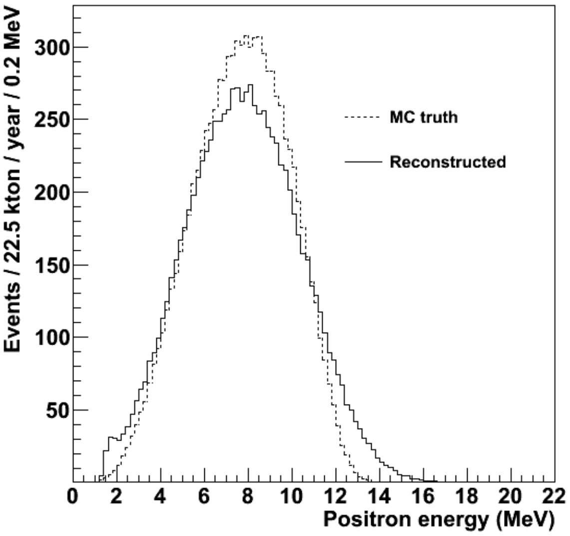

Figure 5.5: Positron energy spectrum induced by the hypothetical solar $\bar{\nu}_e$'s.

Chapter 6

Selection of Neutron Capture Events

This chapter introduces cuts used to select neutron capture events. Since neutron capture on free proton emits a monoenergetic 2.2 MeV γ, this is effectively a search of 2.2 MeV γ's. To study the signal efficiency, 1.6 million of 2.2 MeV γ MC events are generated uniformly in the fiducial volume. The background probability is evaluated using SK-IV random trigger data. Validation of the signal efficiency with an artificial neutron source will be discussed in the next chapter.

6.1 Characteristics of 2.2 MeV γ Events

The 2.2 MeV γ fires on average ∼7 PMT hits in the SK detector. Fig. 6.1 shows the total number of PMT hits generated by a 2.2 MeV γ with the vertex randomly distributed in the fiducial volume. The TOF-subtracted timing distribution is shown in Fig. 6.2, where the solid line histogram uses the true vertex, while the dashed histogram includes the effect of vertex resolution of the primary events. Fig. 6.3 shows the distribution of the number of photoelectrons for each PMT hit. This is very similar to the PMT noise, indicating that the charge information is not useful in searching the 2.2 MeV γ.

6.1.1 Vertex Resolution of the Primary Event

The search of 2.2 MeV γ relies on the primary event vertex for the TOF correction. So the accuracy of primary event vertex reconstruction is of crucial importance. In general the vertex resolution decreases as the event

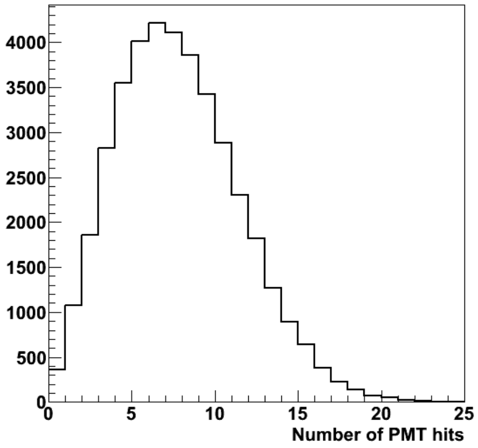

Figure 6.1: Distribution of the total number of PMT hits generated by a 2.2 MeV γ at SK.

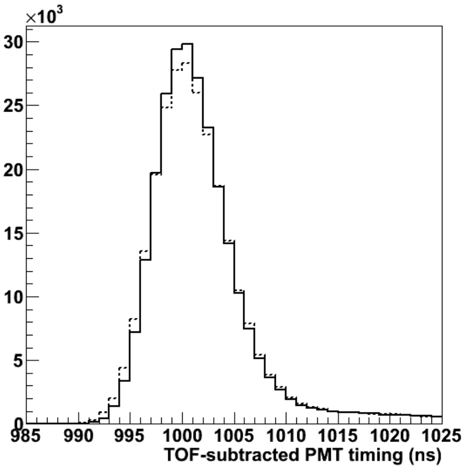

Figure 6.2: Distribution of TOF-subtracted timing for 2.2 MeV γ events. Solid line is for the true vertex. Dashed line includes the vertex resolution effect of the primary event.

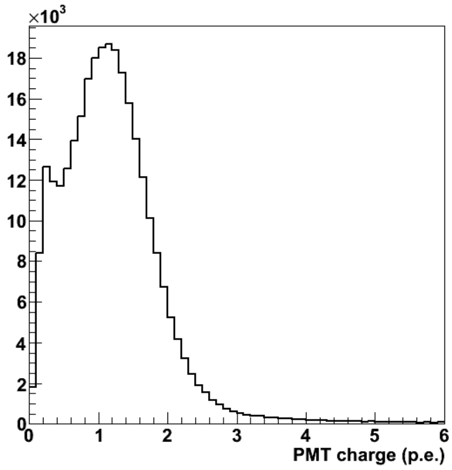

Figure 6.3: Charge distribution of 2.2 MeV γ events.

energy increases. For a 15 MeV electron, the resolution is ~50 cm [102]. The effect of vertex resolution is included by smearing the true MC vertex of the 2.2 MeV γ. The smearing parameter is obtained by studying the vertex resolution of monoenergetic 18 MeV electrons generated by LINAC. Fig. 6.4 shows the distribution of distance from the reconstructed vertex to the true vertex for 18 MeV electrons. This is used as a reference histogram to smear MC vertex. As a result, 2.2 MeV γ's timing peak spreads slightly wider, as shown by the dashed histogram in Fig. 6.2.

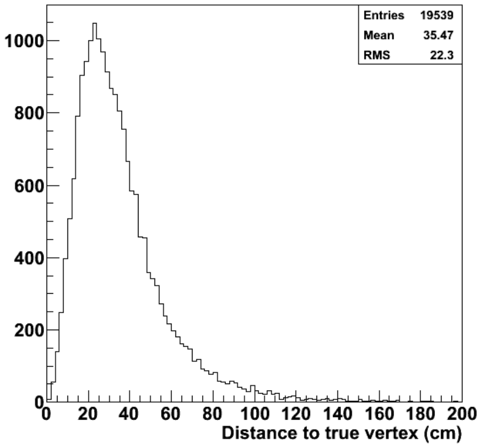

Figure 6.4: Distance from the reconstructed vertex to the true vertex for 18 MeV electrons.

6.2 Pre-selection

To select the 2.2 MeV γ event following a primary event, the first step is to do the TOF subtraction using the primary event vertex. And then sort the PMT timings in increasing order and search the timing peaks with a sliding time window. Backgrounds to the 2.2 MeV γ events include PMT noise, radioactivities from the surrounding rock, radon contamination in water and PMT FRP case, etc.

The background level depends on the size of data that is being searched after each primary event. Unless otherwise stated, in the following background is referring to the number of fake 2.2 MeV γ peaks in a 500μs data pack. Since these fake peaks have no time correlation with the primary event, background can be easily scaled if a different size of data is searched.

N10

The sliding time window used to search a 2.2 MeV γ peak is 10 ns. The background level increases dramatically if the timing window is widened. On the other hand, more signal PMT hits are uncovered if the timing window is smaller, as can be seen from Fig. 6.2. Fig. 6.5 shows the distribution of the maximum number of PMT hits in a 10 ns window (N10). From this figure, one can see on average there are 11 peaks with N10=6 in a 500μs data pack, much higher than signal. We require N10>7 to reject majority of backgrounds.

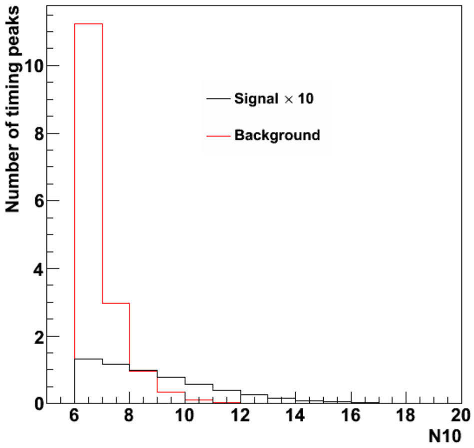

Figure 6.5: Distributions of N10 for signal (black) and background (red). Note that the signal distribution is scaled up by a factor of 10.

Ncluster

It's found that most remaining backgrounds have cluster structures in PMT hits. These backgrounds most likely originate near the detector wall (e.g. radioactivities from PMT glasses and FRP cases) and hence the PMT hits have both tight spatial and temporal correlation. After the TOF subtraction, the hit timing peak remains and can thus pass the N10 cut. Fig. 6.6 (a) shows the distribution of cosα, where α is the angle between any two hit vector combinations. Background's cosα strongly peaks at 1, suggesting many PMT hits are very close to each other. This feature, however, does not show up in the 2.2 MeV γ events.

A search of hit clusters is performed for the PMT hits within the 10 ns window. Starting with a certain hit, the search looks for the next hit whose hit vector is closest. If the angle between these two PMT hits is less than 14.1° (driven by the cosα distribution), these two hits are considered to form a cluster candidate, and therefore are put into a group. Then the third PMT hit that is closest to any PMT hit in the group is determined. If the angle between the third hit and any hit in the group is less than 14.1°, this hit is added into the group. This algorithm continues until all PMT hits in the 10 ns window have been examined. Multiple clusters in the 10 ns time window is possible. The total number of PMT hits that are in clusters is called Ncluster.

As shown in Fig. 6.7 (a), 86% background peaks have cluster structures, while only 26% signals are found to have clusters. The actual quantity used as a cut is N10 − Ncluster, which is shown in Fig. 6.7 (b). This is better because N10 spectrum of signal is harder than background's (see Fig. 6.5) and using N10 − Ncluster instead of Ncluster can keep most of signals that are found to have clusters. Events with $\mathrm{N10} - \mathrm{Ncluster} < 6$ are rejected. Fig 6.6 (b) shows the distribution of cosα after the cluster cut. The strong peak on background disappears.

Nback

This cut is designed to remove the background due to the PMT noise. The Cherenkov light generated by charged particles in water has a cone structure. For the 2.2 MeV γ events, this cone structure is smeared because the electron scattered by the 2.2 MeV γ is subjected to multiple scattering. Nevertheless, PMT hits generated by a 2.2 MeV γ concentrate in the forward hemisphere. Noise hits, on the other hand, are more uniformly distributed in the detector. To employ this difference in the hit pattern between signal and background, we calculate the angle θ between each hit vector and the estimated direction

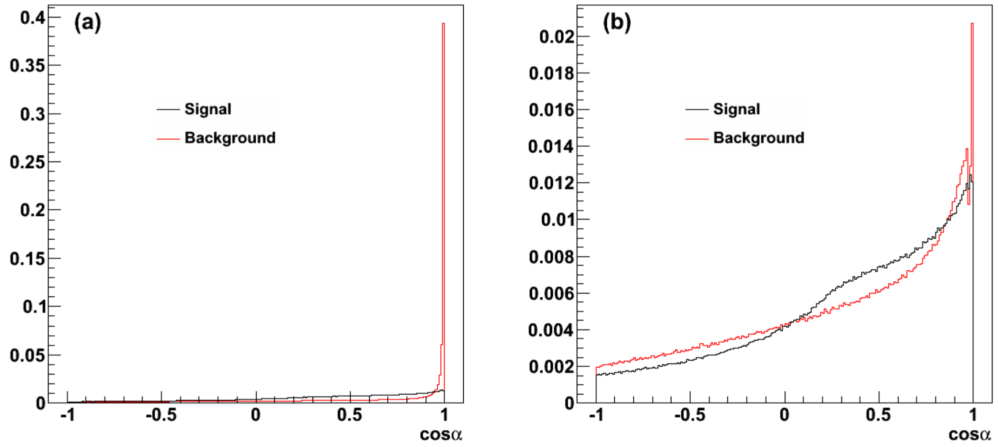

Figure 6.6: Distribution of cosα before (a) and after (b) the cluster cut. Here α is the angle between any two hit vector combinations.

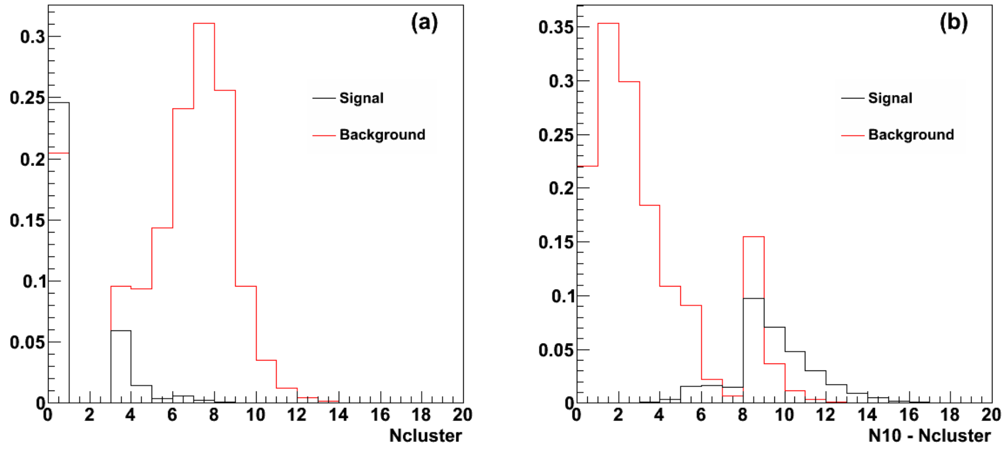

Figure 6.7: Distribution of Ncluster (a) and N10 − Ncluster (b). Definition of Ncluster is given in the text.

(i.e. sum of all the hit vectors). The number of hits with $\theta > 90°$ is called Nback.

For the same reason as using N10 − Ncluster instead of Ncluster, we use N10 − Nback to form a cut, which is shown in Fig. 6.8. Events with N10 − Ncluster < 7 are rejected. Furthermore, those backward going hits are excluded for remain events in calculating other discriminating variables such as $\mathrm{T}_{\mathrm{rms}}$, ϕ_{rms} and θ_{mean}, which will be introduced in the next section. Because some noise hits may happen in coincidence with the signal peak and some Cherenkov photons may be scattered away when propagating in water, excluding the backward going hits help to make cleaner distributions for signals.

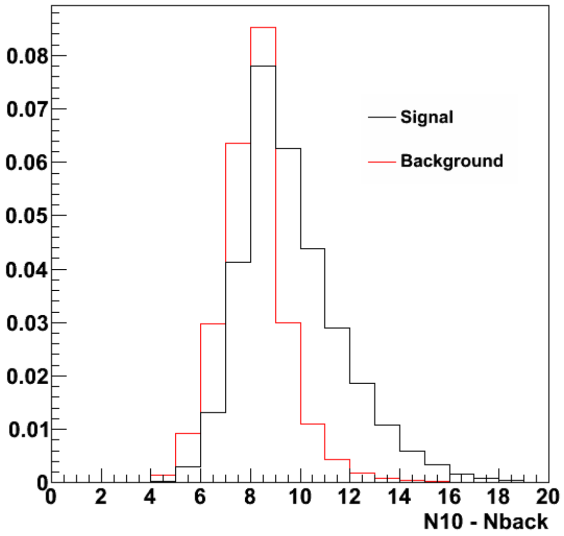

Figure 6.8: Distribution of N10 − Nback.

Nlow

This cut is devised based on the consideration that some PMTs are more likely to be hit than others for a given vertex position. As illustrated in Fig. 6.9, the hit probability for the i-th PMT is

$$\text{hit prob.} \propto \frac{(\cos\theta_i)_{eff}}{R_i^2} e^{-R_i/L} \tag{6.1}$$

where R_i is the distance from the vertex to i-th PMT, θ_i is the incident angle, $(\cos\theta_i)_{eff}$ includes the angular dependence of PMT response, while

L is the attenuation length of Cherenkov light in water, which is taken as 90 m. Formula (6.1) defines the effective acceptance area for the i-th PMT up to an irrelevant normalization constant for Cherenkov photons emitted at the given vertex. When the vertex of the primary event is given, we know that some PMTs (e.g. large θ and/or small R) have larger hit probability than the others (e.g. small θ and/or large R). Noise hits or low energy backgrounds originated in other positions, however, do not follow this law. In particular, noise hits can happen anywhere in the detector with similar probability (assuming PMTs have a similar dark noise rate).

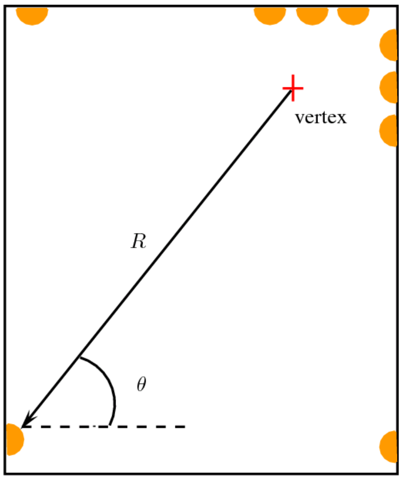

Figure 6.9: Illustration of the idea using Nlow. For a given vertex, hit probability is not equivalent for different PMTs.

Nlow is calculated in the following way. First calculate the effective acceptance area for each PMT for a given vertex according to formula (6.1) and then sort them in decreasing order. Select PMTs that have the largest acceptance area which make up, say, 70% of the total acceptance. The rest PMTs are said to have low hit probability. The number of hits with a low hit probability is called Nlow. Note that for the same fraction of acceptance (e.g. 70%), the number of low hit probability PMTs is not the same for different positions. For example, this number is 4972 for (0, 0, 0) m and 10132 for (14, 0, 15) m. So this cut is tighter near the detector wall, which is desirable because it is observed that background level is much higher near wall than at the center.

Left figure in Fig. 6.10 shows N10−Nlow distribution with acceptance=70% for zone I ($0\,\mathrm{m}^2 < R^2 < 40\,\mathrm{m}^2$, $0\,\mathrm{m} < |Z| < 3\,\mathrm{m}$), middle figure for zone II ($140\,\mathrm{m}^2 < R^2 < 180\,\mathrm{m}^2$, $12\,\mathrm{m} < |Z| < 15\,\mathrm{m}$) and right figure includes all events. We reject events with $\mathrm{N10} - \mathrm{Nlow} < 5$. It is clear from Fig. 6.10

that a larger fraction of background is rejected for events near the wall than at center. However, the background level is still higher near the wall if using the same acceptance for the whole detector. To make the background level flat through the entire detector, we use position dependent acceptance, the choice of which is shown in Fig. 6.11.

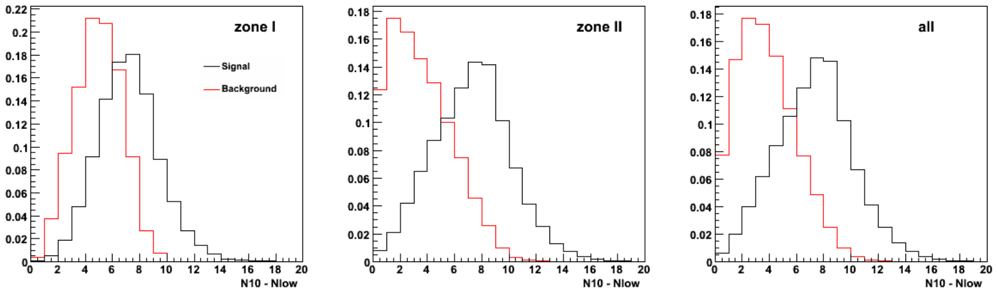

Figure 6.10: The distribution of N10 − Nlow for events in zone I (left), zone II (middle) and all events (right). The definition of zone I and zone II is given in the text.

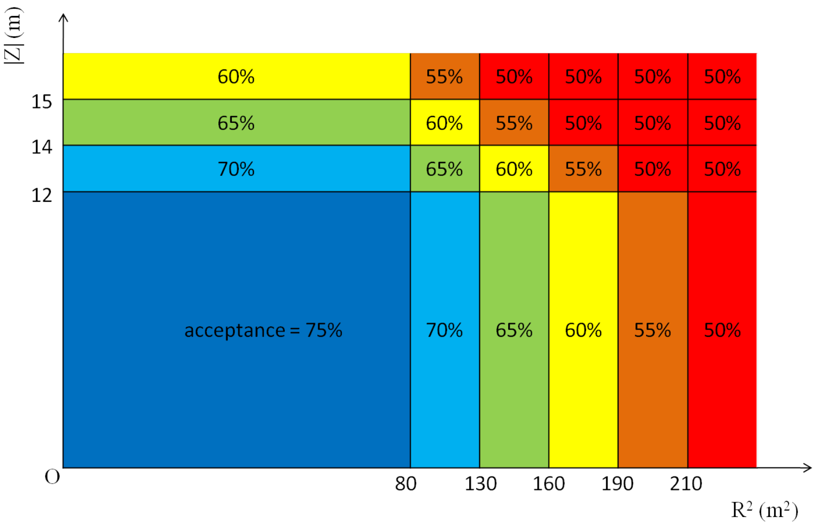

Figure 6.11: The choice of position dependent acceptance used in calculating Nlow.

6.3 Further Reduction

The hard cuts used in the pre-selection eliminates the bulk of backgrounds. There are four more variables that can be used to further separate signal from background.

N300

The 2.2 MeV γ event should be an isolated small timing peak sitting on the PMT dark noises, as illustrated in Fig. 6.12 (a). Fig. 6.12 (b) shows another type of background. The 10 ns window picks up a peak which is part of hit timings of some low energy event. In this case, there must be more hits than expected dark noise around the N10 peak. We use N300 – N10 to look for excess of PMT hits around the N10 peak. The distribution is shown in Fig. 6.13 (a).

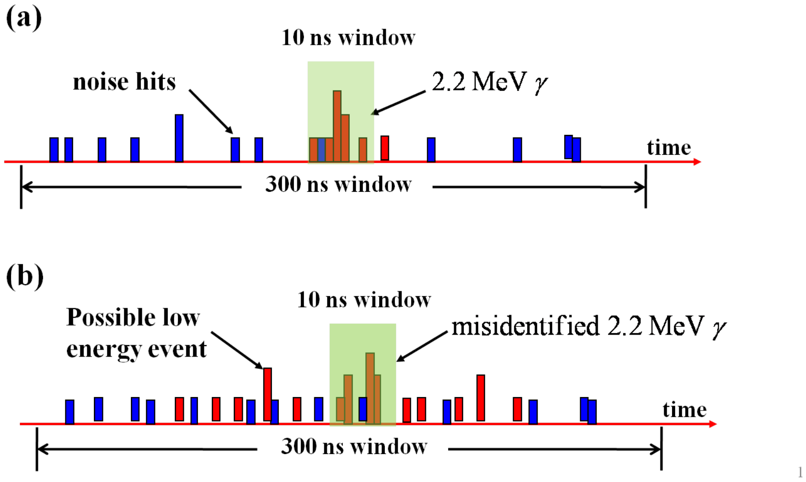

Figure 6.12: Illustration of the definition of N300.

T_{rms}

T_{rms} is the root mean square (RMS) of PMT hit timings. For 2.2 MeV γ events, the spread of hit timings is mainly driven by the PMT time resolution. The distribution of T_{rms} is shown in Fig. 6.13 (b).

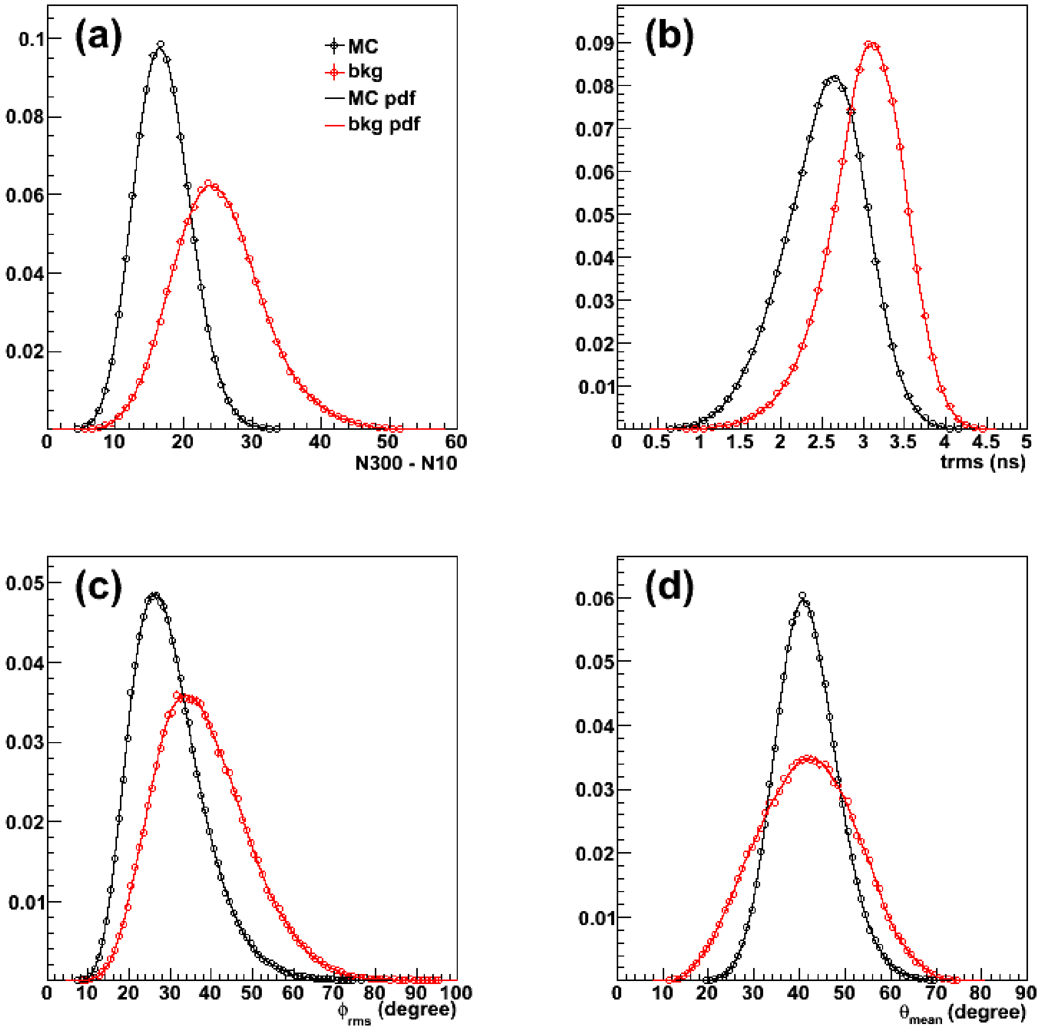

Figure 6.13: The distributions of N300−N10 (a), T_{rms} (b), ϕ_{rms} (c), θ_{mean} (d). The points represent signal (black) and background (red) histograms and the lines indicate the corresponding PDF's.

$\phi_{\mathbf{rms}}$

$\phi_{\rm rms}$ is the RMS of azimuth angle of hit vectors, measuring the azimuth uniformity of hits. It's distribution is shown in Fig. 6.13 (c).

$\theta_{\mathbf{mean}}$

$\theta_{\rm mean}$ is the mean angle between the hit vector and the estimated direction. Fig. 6.13 (d) shows the distribution of $\theta_{\rm mean}$.

These four discriminating variables have weak correlation and little position dependence. Hence a global likelihood function can be formulated. The PDF for each variable is obtained by a nonparametric histogram fitting using the TMVA [103] package. All PDF's are also shown in Fig. 6.13. The likelihood ratio $r_L(i)$ for event i is defined by

$$r_L(i) = \frac{L_S(i)}{L_S(i) + L_B(i)} \tag{6.2}$$

where

$$L_{S(B)}(i) = \prod_{k=1}^{4} p_{S(B),k}(x_k(i)) \tag{6.3}$$

and $p_{S(B),k}$ is the signal (background) PDF for the kth input variable x_k. Fig. 6.14 shows the distribution of the likelihood ratio. Events with $r_L < 0.35$ are rejected.

6.4 Summary of 2.2 MeV γ Cut Efficiency

Table 6.1 summarizes the cut efficiency after each cut, where all quoted numbers for signal assumes true vertex. If the vertex is smeared according to the scheme described in Sec. 6.1.1, the efficiency for signal after all cuts is 19.3%.

The efficiency variation in the detector is studied by dividing the detector volume into 10×11 cells. As shown in Fig. 6.15, after the tuning of Nlow cut, both the signal efficiency and background probability are quite uniform in the entire detector volume. The 1-σ uncertainty is 1.0% and 0.1% for signal efficiency and background probability, respectively.

The accuracy of the background probability is very important when applying the neutron tagging to data analysis. Time variation of the background probability is checked using availible random trigger data. Fig. 6.16

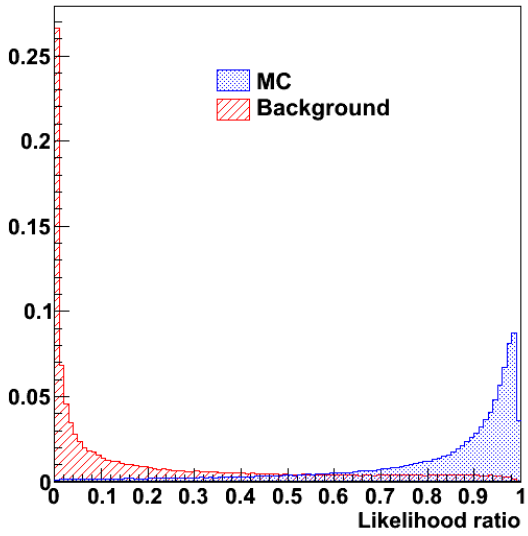

Figure 6.14: Distribution of the likelihood ratio.

Table 6.1: Summary of efficiency after each cut step.

Cut	Signal (MC)	Background (500 μs)
N10 > 7	33.3%	150.1%
N10 − Ncluster > 5	31.3%	23.8%
N10 − Nback > 6	29.6%	19.7%
N10 − Nlow > 4	21.2%	3.9%
likelihood ratio > 3.5	19.8%	1.0%

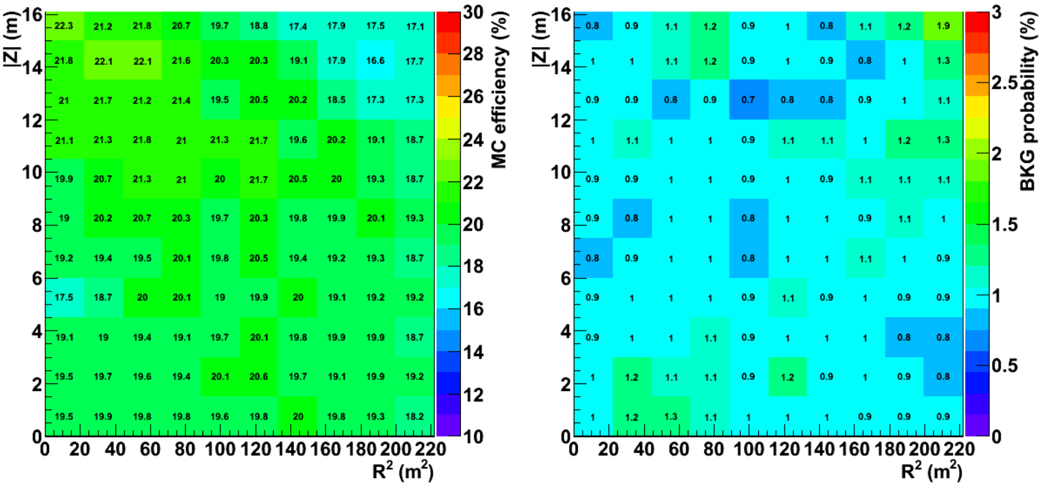

Figure 6.15: Efficiency variations in the detector for signal (left) and background (right). The statistical uncertainty in each cell is 0.4% and 0.1% for signal and background, respectively.

shows the background probability thoughout the SK-IV period, where the background probability is (1.00±0.02)%.

Both the signal efficiency and background probability are evaluated using a large sample and hence have a small statistical uncertainty, which is 0.04% and 0.01%, respectively. In sum, the selection efficiency for the 2.2 MeV γ is (19.3 ± 0.04(stat.) ± 1.0(sys.))%. And the background probability for 500 μs data is (1.0 ± 0.01(stat.) ± 0.1(sys.))%.

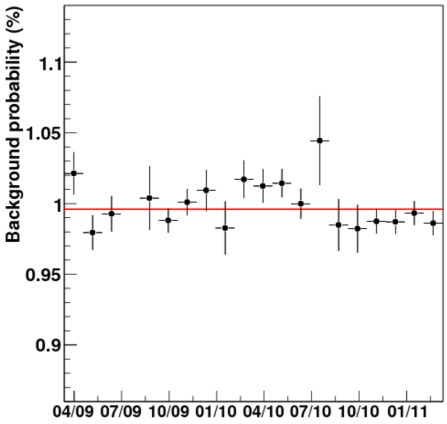

Figure 6.16: Time variation of the background probability from random trigger data. The horizontal line indicates the average value.

Chapter 7

Validating Neutron Tagging Efficiency Using an Am/Be Source

The neutron tagging efficiency evaluated with the MC sample in the previous chapter will be verified in this chapter. An Am/Be radioactive source is used to mimic the inverse beta decay reaction chain and to confirm the neutron tagging efficiency. Such a test was firstly conducted in SK-III [77]. In that test, however, due to the limitation of old electronics, only ∼120 μs data could be taken after the prompt event, resulting in that the neutron tagging efficiency can not be determined precisely. The same experiment is repeated in SK-IV, dring which the AFT trigger (see section 2.4.3) gate width is temporarily enlarged to 800 μs, in order to obtain a more complete neutron capture time spectrum.

7.1 Experimental Setup

The Am/Be source is embedded in a bismuth germanate oxide (BGO) scintillator cube. The detailed configuration of this apparatus is shown in Fig. 7.1. The prompt and delayed event-pair is generated via

$$\begin{aligned} \alpha + {}^{9}\mathrm{Be} &\rightarrow {}^{12}\mathrm{C}^{*} + n \\ {}^{12}\mathrm{C}^{*} &\rightarrow {}^{12}\mathrm{C} + \gamma \qquad \text{(prompt)} \\ n + p &\rightarrow d + \gamma \qquad \text{(delayed).} \end{aligned} \tag{7.1}$$

Note that the reaction to the ground state of ^{12}C also exists, where no 4.43 MeV deexcitation γ is emitted. The intensity of the source is 97 μCi, leading to 87 Hz of 4.43 MeV γ emittion and 76 Hz of ground state transition [77]. The neutrons emitted in the ground transition have no associated prompt signal, and thus appearing as a flat background to the prompt and delayed event pair search. The BGO crystal is used to compensate the disadvantage of low Cherenkov light generation for the 4.43 MeV γ in water. The observed scintillation light is typically ~1000 p.e.'s (see Sec. 7.2.1), which is capable of issuing a SHE trigger.

The experimental apparatus was firstly deployed at the center (35.3, -70.7, 0.) cm (A) of the tank. To estimate the source related background (e.g. ground transition neutron), a 10 Hz of 800 μs random data was also taken without a trigger threshold. Additional data was taken with the source located at (35.3, -1201.9, 0.) cm (B) and (35.3, -70.7, 1500) cm (C), but for a shorter time and without random trigger. Dummy data without the source was also taken to evaluate accidental background.

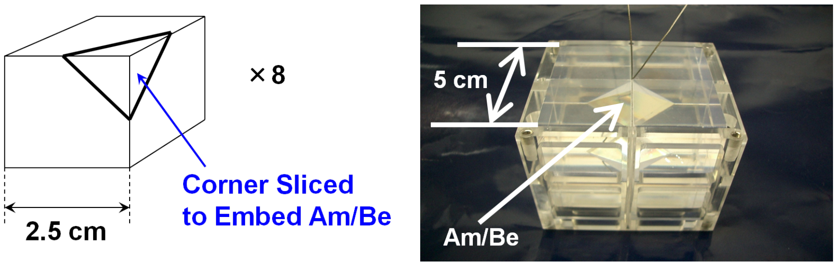

Figure 7.1: Configuration of the experimental apparatus. The Am/Be source is embedded in the center of 8-piece BGO crystal, which is held together with an acrylic case.

7.2 Data Analysis

7.2.1 Selection of Prompt Scintillation Events

The prompt event of interest is that generated by the 4.43 MeV γ. Fig. 7.2 shows the totle p.e. distribution of prompt scintillation events that have SHE trigger for the source at A (a), B (b) and C (c). The peak around ~1000 p.e. corresponds to the 4.43 MeV γ. Only events around this peak are selected for the analysis. To avoid the neutrons coming from the previous scintillation events, a good prompt event should have sufficient large time difference to the previous event. Finally, there should be no overlapping scintillation events. A sliding 200 ns window is used to search possible major timing peaks after the prompt event. In sum, the selection criteria for prompt events are:

1. $750 <$ totle p.e. < 1050 for source at A, $850 <$ totle p.e. < 1150 for B and $900 <$ totle p.e. < 1150 for C.
2. Time difference to the previous event $> 1.5\,\text{ms}$.
3. N200 (after the prompt event) < 50.

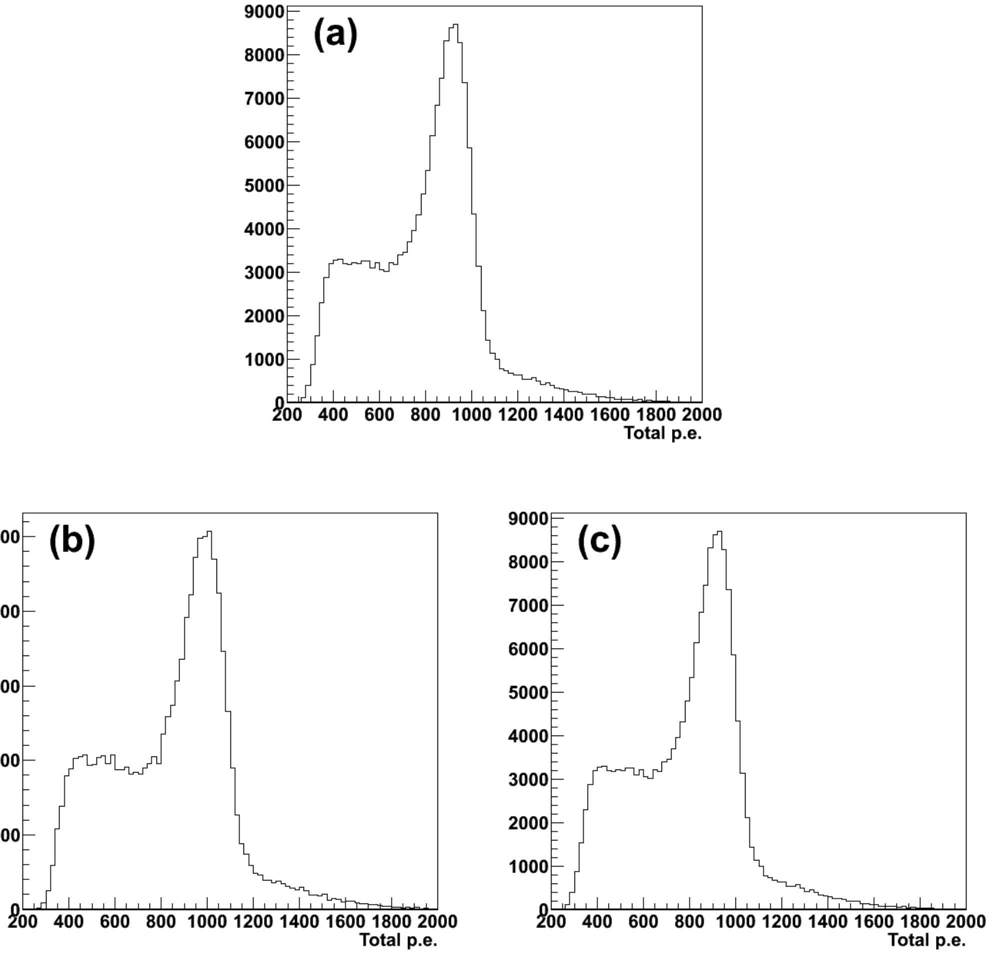

Figure 7.2: Total p.e. of the primary scintillation events for the source at A (a), B (b) and C (c).

7.2.2 Selection of Neutron Capture Events

The cuts introduced in the previous chapter are applied to select the delayed neutron capture signal. Here we explain the details using data taken at A as an example. The application to data taken at the other two locations is in a similar fashion.

Pre-selection

Fig. 7.3 shows the N10 distribution after the pre-selection (see section 6.2). Note that the delayed events associated with the prompt scintillation events have a tail on the right. This significantly deviates from the expectation for a 2.2 MeV γ signal. Similar structure is also seen in the random trigger data but not in dummy data. So there's another apparatus related background besides that arised from the ground state transition . In total, there are three types of backgrounds:

- neutrons emitted in ground state transition.
- unknown source related background having larger N10.
- accidental background.

The time difference between the delayed event and the prompt event (ΔT) for all the backgrounds is flat (see Fig. 7.6 (a)), as opposed to the signal which is exponential (Fig. 7.6 (b)). Hence the signal events can be extracted by fitting the ΔT spectrum. Actually, the identical backgrounds also present in the random trigger data and can be easily estimated for the case of source at the center. The difference between the scintillation correlated and the random triggered delayed events gives the pure signal and can be compared with MC directly.

Further Reduction

Fig. 7.4 shows a comparison between data and MC for discriminating variables used in the further reduction, where all backgrounds are subtracted using the random trigger data. A likelihood cut described in section 6.3 is then applied and the distribution of final N10 is shown in Fig. 7.5. Simulation of the 2.2 MeV γ is justified by the good agreement between data and MC.

7.3 Results

As mentioned above, the ΔT distribution of backgrounds is flat (Fig. 7.6 (a)) and signal fraction can be extracted by fitting the ΔT spectrum. An

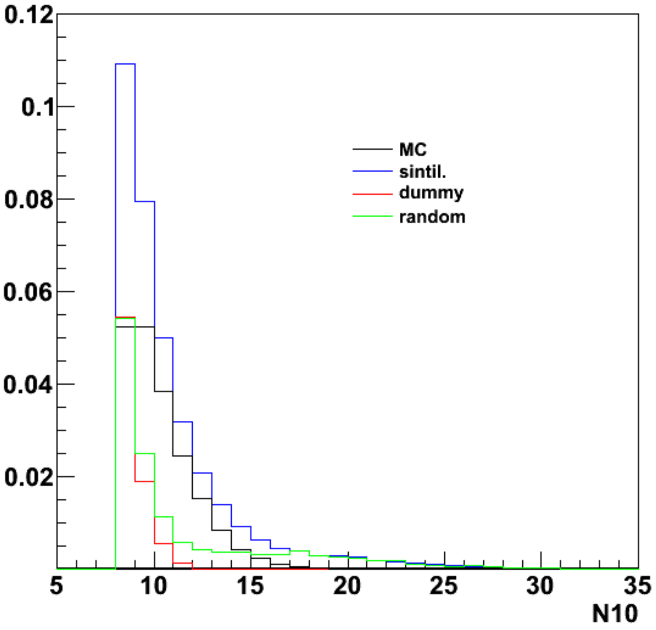

Figure 7.3: N10 of the Am/Be data after the pre-selection. Histrogram in black represents MC, the blue line indicates the delayed signal that have the prompt scintillation event, the green line shows the events in the random trigger data and the red line represent the accidental background from the dummy data.

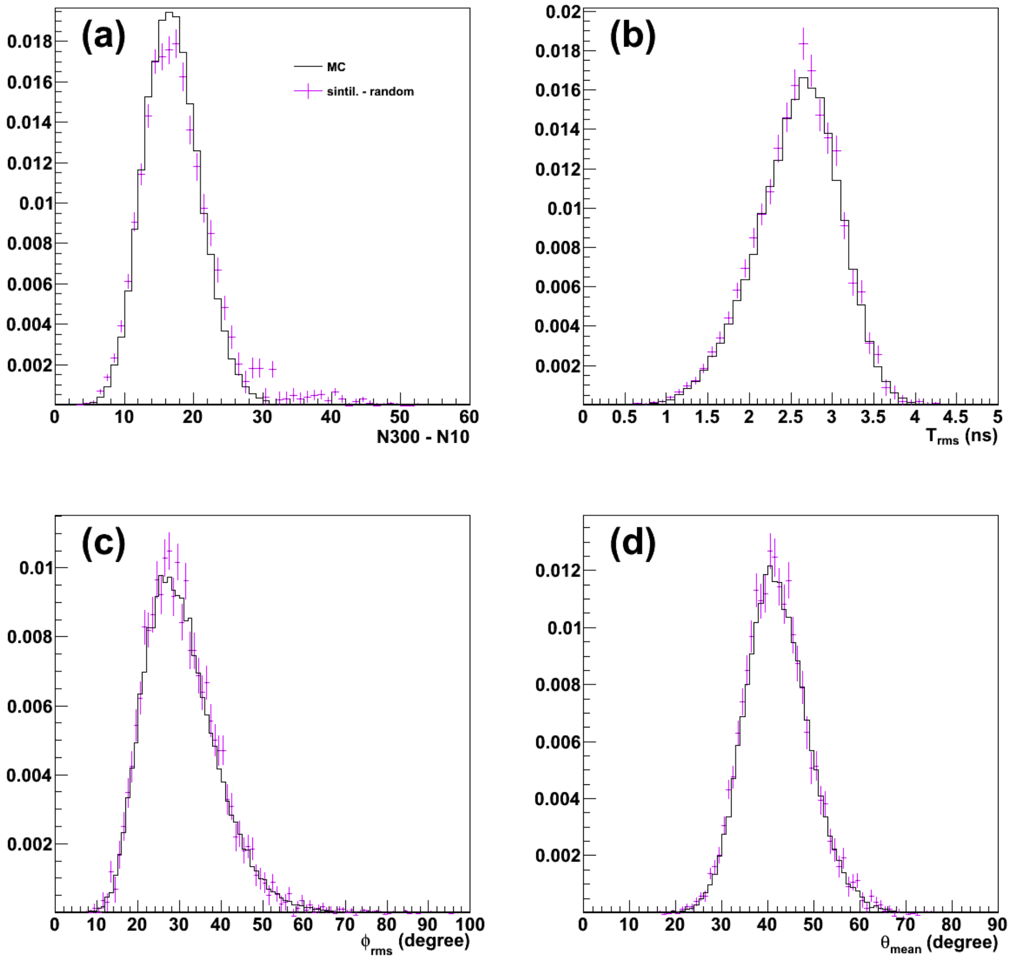

Figure 7.4: Comparison of Am/Be data and MC for N300−N10 (a), $\mathrm{T}_{\mathrm{rms}}$ (b), ϕ_{rms} (c), θ_{mean} (d). Solid histograms represent MC and dots indicate the Am/Be data.

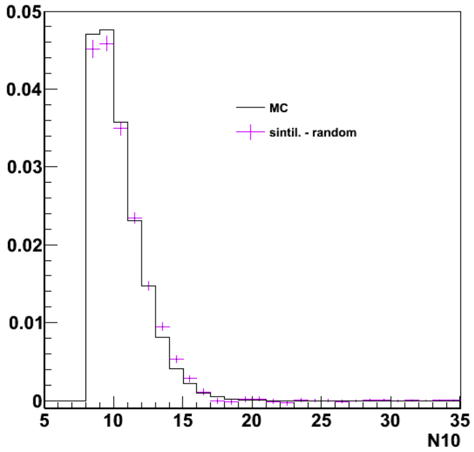

Figure 7.5: Comparison of N10 between the Am/Be data and MC after all cuts applied.

unbinned maximum likelihood fit is performed using the following function:

$$f = c_s f_s e^{-\frac{t}{\tau}} + c_b(1 - f_s) \tag{7.2}$$

where f_s is the signal fraction, τ is the mean neutron capture time in water and, c_s, c_b are the normalization constant for signal and background, respectively. Since neutron is first thermalized before being captured, ΔT is the sum of thermalization time and capture time. And hence the ΔT distribution of signal is not simply exponential. But it can be shown that neutron capture ΔT is well approximated by an exponential function when ignoring the first few ten's of μs data. In our fit, the starting point is 75 μs.

The fitting result for source at A is shown in Fig. 7.6 (b). As previously stated, in this case, the signal fraction can be estimated using the random trigger data, resulting in one less parameter to fit. A fit fixing the signal fraction is shown in Fig. 7.6 (c), where the uncertainty on the neutron capture time is reduced. Fig. 7.7 shows the fitting result for source at B (left) and C (right), respectively.

The neutron tagging efficiencies in the Am/Be data are summarized in Table 7.1. Data is in good agreement with MC. Table 7.2 lists the thermal neutron lifetime in water for the three locations, which give the combined result:

$$\tau = (203.7 \pm 2.8)\mu\text{s}. \tag{7.3}$$

This agrees with the previous works (see e.g. [104]).

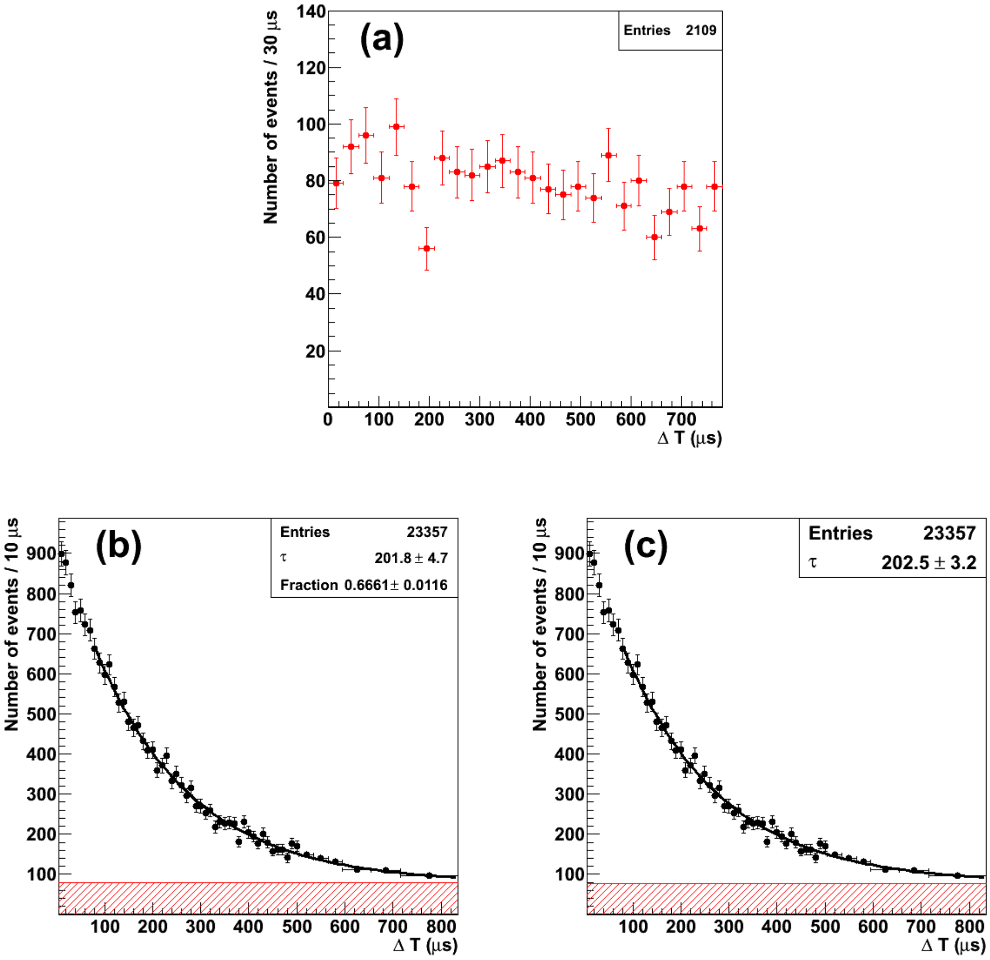

Figure 7.6: (a) ΔT of backgrounds in the random trigger data. (b) Unbinned maximum likelihood fit with the signal fraction as a free parameter. (c) Unbinned maximum likelihood fit with the signal fraction fixed. Shaded area in (b) and (c) represent the fitted and estimated background, respectively.

Table 7.1: Tagging efficiency of neutrons generated by the Am/Be source.

Source	MC (%)	ML fit (%)	Estimated using random data (%)
A	19.2±0.1	19.0±0.3	19.0±0.2
B	20.3±0.1	19.3±0.6	-
C	22.4±0.1	22.2±0.7	-

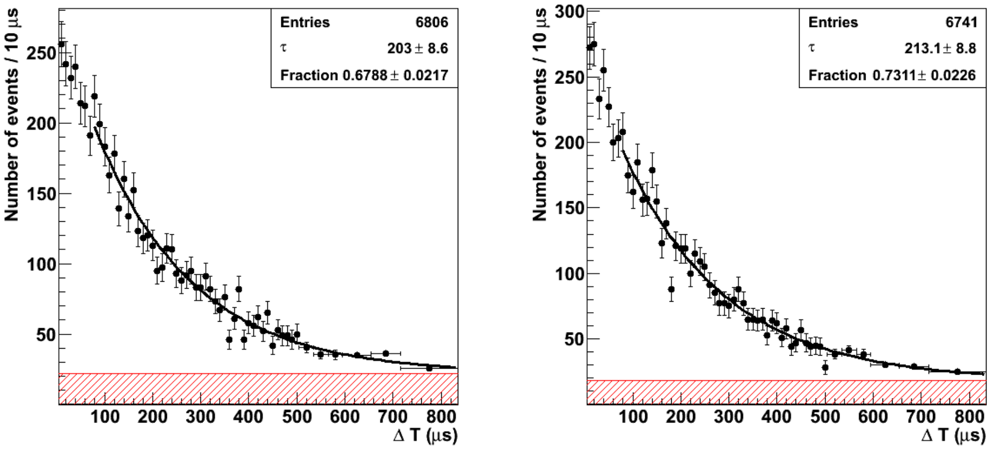

Figure 7.7: Unbinned maximum likelihood fit for the source at B (left) and C (right).

Table 7.2: Fitted thermal neutron lifetime in water.

Source	ML fit (μs)	Comment
A	201.8±4.7	bkg. free
A	202.5±3.2	bkg. fixed
B	203.0±8.6	-
C	213.1±8.8	-

7.4 Conclusion

Given the good agreement between data and MC in various comparisons, we conclude that the neutron tagging efficiency obtained by the 2.2 MeV γ MC is well reproduced by the Am/Be source data.

Chapter 8

Tagging Neutrons in Atmospheric Neutrino Data

A detailed description of SK atmospheric neutrino data can be found elsewhere [105]. Here we only mention some jargons that will be used in our discussion. Atmospheric neutrino events in SK are classified as fully contained (FC) if all of the energy is deposited in ID, partially contained (PC) if a high energy muon exits ID and upward going muon (UPMU) which originated in the surrounding rock. In this chapter, we will focus on searching the neutrons associated with the FC neutrino events.

For atmospheric neutrino events in SK, neutrons can be produced in the following ways:

1. Direct production in neutrino interaction with water, e.g. inverse beta decay.
2. Nucleon and pion interactions in oxygen before exiting.
3. Nucleon ejection in π/Δ absorption in oxygen.
4. Secondary interactions with water.

The simulated SK atmospheric neutrino events are generated using NEUT (see [105] and references therein). Because neutrons were previously undetectable at SK, the production of the neutron was not fully simulated. Item 1 and 2 are already implemented in the current simulation in SK, item 4 is partially implemented and item 3 has not been included yet.

8.1 Observation of Neutrons in FC Data

8.1.1 Selection of Primary FC Neutrino Events

In this analysis, we use only data since when the AFT gate was changed to 500 μs to present. Events that have no associated AFT trigger are also not included. Finally, events with visible energy below 100 MeV are excluded. The vertex resolution is estimated to be 30 cm for the single-ring events [105].

8.1.2 Searching Neutrons Associated with FC Events

Due to the complicated production mechanism, the yield of neutron capture signal is unknown as a priori. The background probability, on the other hand, is known to be ∼1% (see section 6.4). Fig. 8.1 shows the distributions of discriminating variables after the pre-selection. The solid histograms show the expected spectra obtained via:

$$h_i = (1 - f_b)h_{s,i} + f_b h_{b,i} \tag{8.1}$$

where $h_{s(b),i}$ is the normalized reference histogram for the ith variable for signal (background), while f_b is the fraction of background, determined by

$$f_b = \frac{N_{\text{primary}} \times P_b}{N_n}, \tag{8.2}$$

where N_{primary} is the number of primary events, P_b is the background probability and N_n is the total number of the neutron candidates after pre-selection. The reference histogram $h_{s,i}$ is from the 2.2 MeV γ MC and $h_{b,i}$ from the random trigger data, same as that presented in chapter 6. The composite histogram h_i is normalized to the data indicated by the dots in Fig. 8.1.

The final N10 after the likelihood cut is shown in Fig. 8.2. The expected spectra are reproduced by data fairly well. Fig. 8.3 shows the ΔT distribution together with the fitted neutron lifetime, which is consistent with the measurements using the Am/Be source. These distributions collectively demonstrate, for the first time, a clear observation of neutrons produced in neutrino interactions in a water Cherenkov detector.

8.1.3 Results and Discussions

Fig. 8.4 shows the neutron yield (number of neutrons in one event) as a function of the visible energy of atmospheric neutrino events, where the data has already been corrected by the neutron tagging efficiency. Similar energy

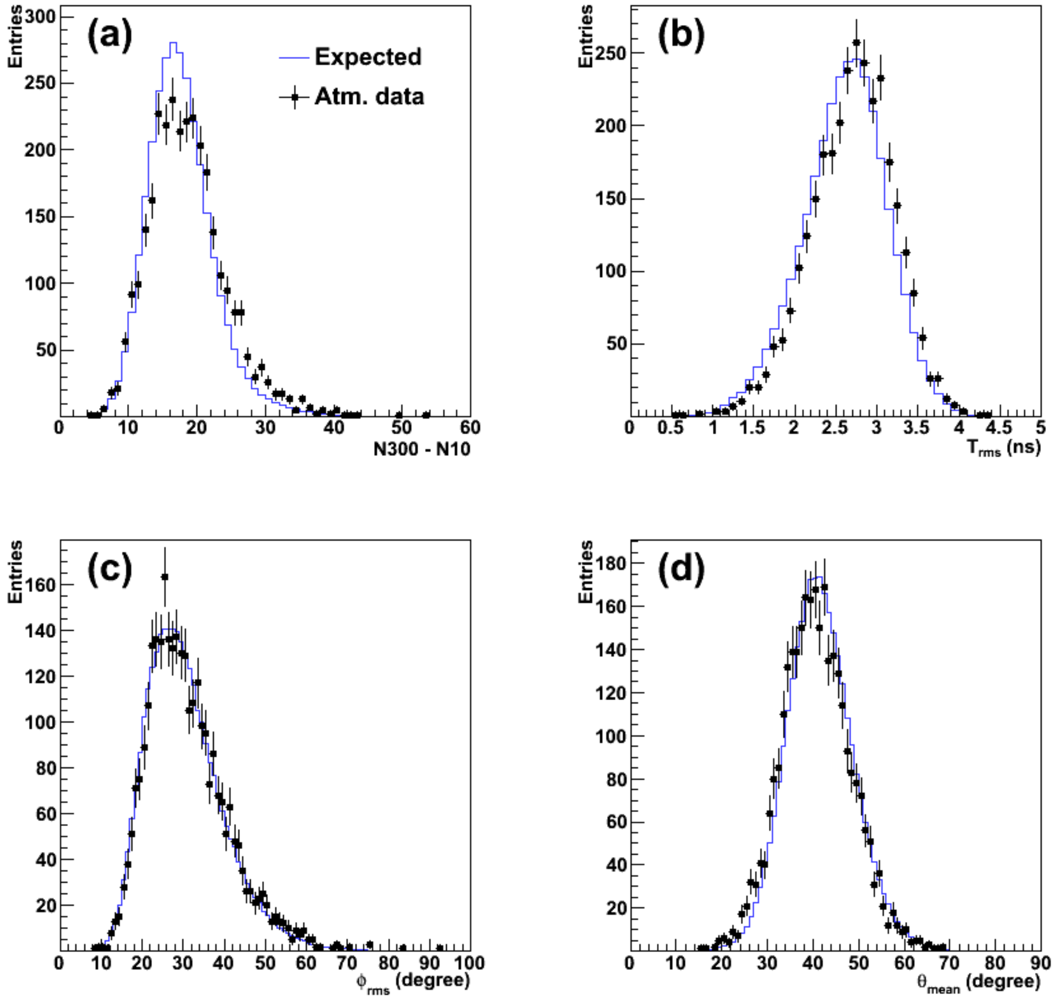

Figure 8.1: Distribution of N300 − N10 (a), T_{rms} (b), ϕ_{rms} (c) and θ_{mean} (d) after the pre-selection. The dots represent the neutron candidates in FC neutrino data and the solid histograms indicate the expected spectra which is normalized to the data.

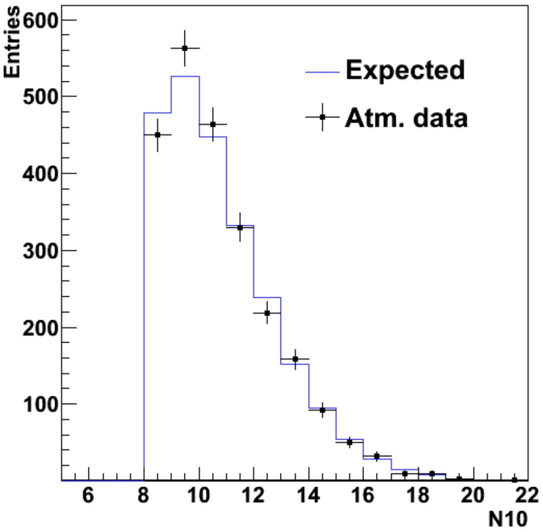

Figure 8.2: Final N10 of the neutron candidates in the atmospheric FC data. The solid histogram represents the expected distribution which is normalized to the data as indicated by the dots.

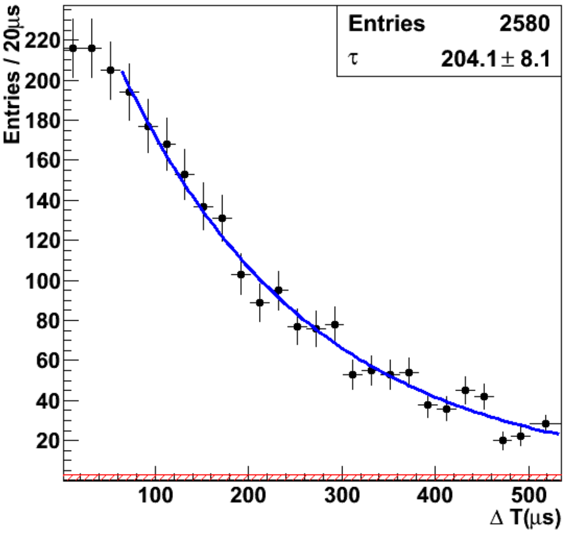

Figure 8.3: Distribution of ΔT of the neutron candidates in the atmospheric neutrino data . The dots are for the data, the curve shows the fitted lifetime and the shaded histogram shows the expected accidental background.

dependence is seen in both MC and data. The deficit in MC is understood to be due to that the neutron production in SK is not fully simulated in MC. More information is carried by the multiplicity of neutrons, which is shown in Fig. 8.5.

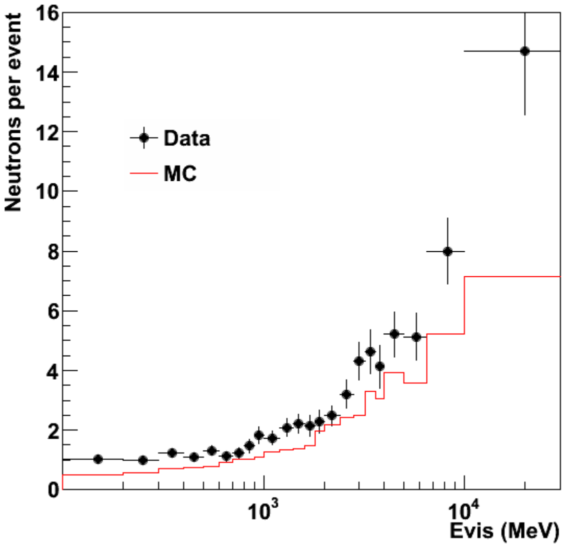

Figure 8.4: The efficiency-corrected neutron yield as a function of visible energy. Solid histogram and dots are for the MC and data, respectively.

8.2 Background Rejection for Proton Decay Searches

Backgrounds in the proton decay searches at SK arise mainly from the atmospheric neutrino interactions. The estimated background is $0.3 \pm 0.04 \pm 0.11$ events for SK-I [5], which is not a big problem for SK-scale detector. However, the background becomes serious when going to the next generation megaton-scale detectors. According to Ref. [5], the background rate is estimated to be $2.1 \pm 0.3 \pm 0.8$ events/megaton·year. The sensitivity of proton decay searches could be significantly improved if backgrounds can be further reduced.

It turns out that the neutron tagging could reject a large fraction of remain background for the proton decay searches. No neutron is expected in the final state of proton decay, while many background processes are accom-

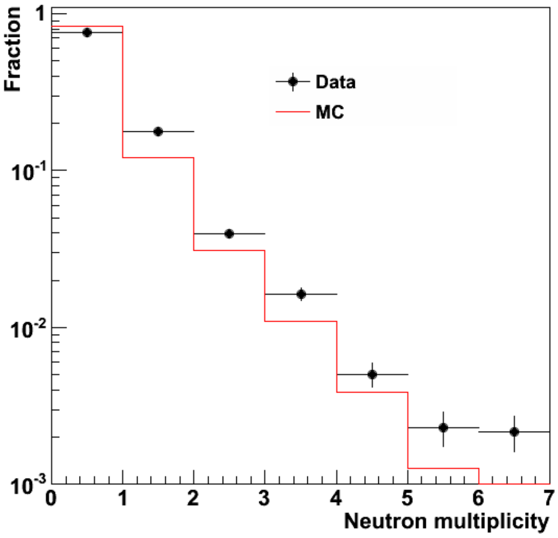

Figure 8.5: Neutron multiplicity in one event. Solid histogram and points represent MC and data, respectively.

panied with neutrons. Here we take $p \to e\pi^0$ as an example, some background processes are:

(a) $\nu_e + p \to e^- + p + \pi^+$, π^+ induce π^0 through charge exchange

(b) $\nu_e + n \to e^- + p + \pi^0$

(c) $\nu_e + n \to e^- + n + \pi^+$, π^+ induce π^0 through charge exchange

(d) $\nu_e + n \to e^- + p + \pi^0$, p interacts in ^{16}O to give one neutron

Neutrons can be produced directly (c) or indirectly (d). Process (a) and (b) do not have neutrons in the final state and remains irreducible. Process (c) and (d) can be rejected if neutrons in the final stated can be identified.

We use the atmospheric neutrino MC to estimate the neutron production in background processes for the proton decay searches. Fig. 8.6 shows the distribution of the invariant proton mass versus the total momentum for the events passed all the proton decay search criteria, except for the momentum cut and the invariant mass cut. The proton decay signal region is defined as: total momentum < 250 MeV/c, 800 MeV/c^2 $<$ total invariant mass < 1050 MeV/c^2. Since there are not sufficient statistics inside the signal box, we use an enlarged area (indicated by the outer box in Fig. 8.6) to estimate the neutron production assuming those events having a similar profile as that in the signal region (inner box in Fig. 8.6). The neutron yield in these events is listed in Table 8.1, from which one can estimate how much background can be reduced by tagging neutrons in the final state. For example, ∼23% backgrounds can be rejected by tagging neutrons in pure water. In case of a Gd-loaded detector, ∼56% backgrounds can be rejected assuming neutron tagging efficiency is 67.7% [77].

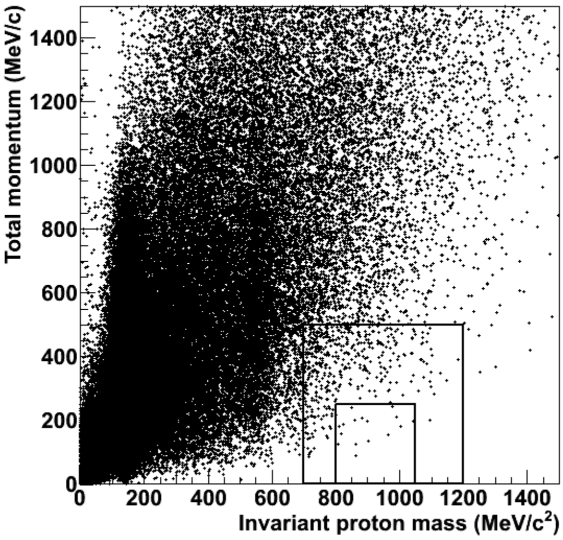

Figure 8.6: The total momentum versus the total invariant mass for 500 year-equivalent atmospheric MC. The inner box indicates the proton decay signal region. The outer box represent the area that is used for an estimation of neutron production.

Table 8.1: Neutron production in proton decay backgrounds.

# of neutrons in one event	Fraction (%)
0	31.5
1	30.1
2	18.2
3	9.2
4	5.2
>=5	5.8

8.3 Reconstructing 2.2 MeV γ's

The low energy reconstruction tool BONSAI can not be directly applied to the 500 μs data pack. However, once the 2.2 MeV γ peak is located using the method described in chapter 6, it is possible to apply BONSAI to the 1 μs data around the 2.2 MeV γ peak. We use the 2.2 MeV γ sample selected in the atmospheric neutrino data to check the performance of the reconstruction. Fig. 8.7 shows the reconstructed energy for the 2.2 MeV γ candidates selected from atmospheric neutrino data and the 2.2 MeV γ MC. Note that the reconstructed energy is larger than 2.2 MeV due to the N10 $>$ 7 selection. Distance between the reconstructed the 2.2 MeV γ vertex to the primary event vertex is shown in Fig. 8.8. About half of the 2.2 MeV γ candidates are reconstructed within 300 cm to the primary event vertex. The correlation of the primary event vertex and the 2.2 MeV γ vertex is clearly seen. On the other hand, the accidental background events do not have such a tight correlation, as shown in Fig. 8.9. In principle, using the distance as a cut can improve the signal-to-noise ratio for the 2.2 MeV γ selection. But no significant improvement is found for the $\bar{\nu}_e$ analysis (see chapter 10) by requiring the distance less than 300 cm, because the distance cut reduce the signal efficiency by a factor of two. The reconstruction of the 2.2 MeV γ's is mainly for cross-checking the analysis method presented in chapter 6.

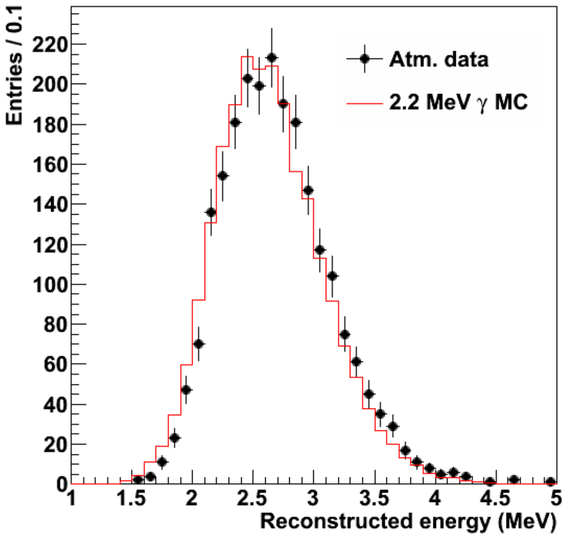

Figure 8.7: Reconstructed energy for the 2.2 MeV γ's selected from atmospheric neutrino data (dots) and the 2.2 MeV γ MC (line).

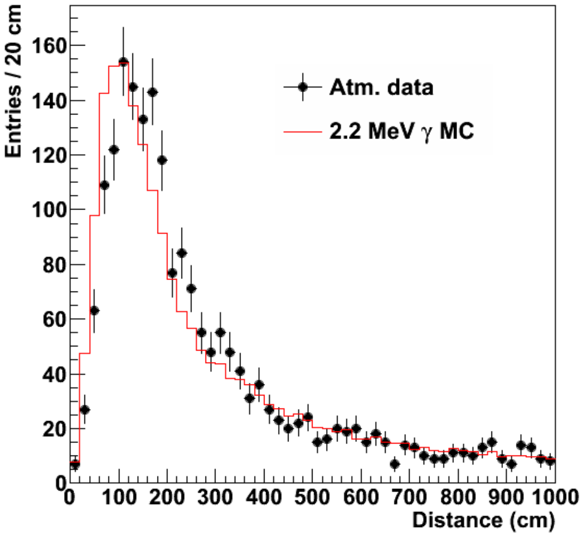

Figure 8.8: Distance between the reconstructed 2.2 MeV γ vertex to the primary event vertex for atmospheric neutrino data (dots) and the 2.2 MeV γ MC (line).

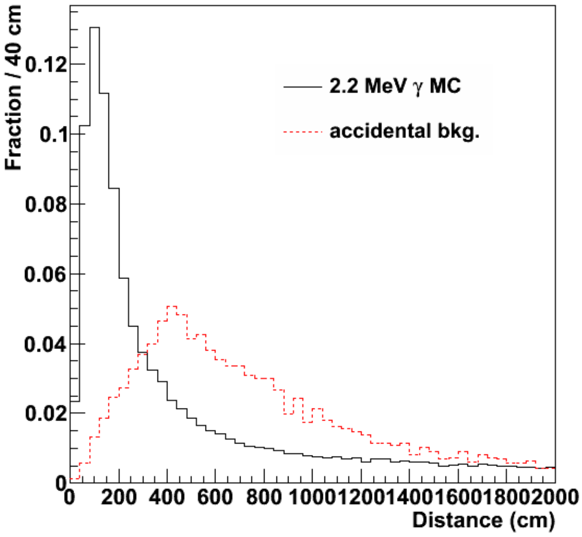

Figure 8.9: Distance between the reconstructed 2.2 MeV γ vertex to the primary event vertex for MC (solid) and accidental background (dashed).

Chapter 9

Data Reduction

The primary goal of this analysis is to search for $\bar{\nu}_e$ signal, i.e. a prompt e^+ and a delayed 2.2 MeV γ. This chapter introduces reduction steps that aim at making a final sample of e^+ candidates. The search of 2.2 MeV γ is only conducted to the AFT events that follows a SHE event in this e^+ sample and will be discussed in the next chapter.

The $\bar{\nu}_e$'s are searched in the energy range of 12–30 MeV. Below 12 MeV, there are too many spallation events even after the spallation cut, resulting in too large an accidental background. Above 30 MeV, the atmospheric neutrino background becomes dominant. Unless explicitly stated, distributions shown in this chapter are for events with energy below 30 MeV.

9.1 Data Sets and Run Selection

Super-Kamiokande data are collected in a unit of "run". Each run has a maximum duration of 24 hours and is divided into subruns that each lasts approximately for one minute. The whole data sets are classified into the normal run, test run and various calibration run category. Only the normal runs are used for physics analysis. At the beginning of SK-IV data taking, the gate width of AFT events was tentatively set to 350 μs and then changed to 500 μs after 28 November 2008 to improve the detection efficiency for neutron capture events. The data used in this analysis span from 28 November 2008 to 27 December 2011, corresponding to a live time of 960 days after removing bad runs or subruns that are described below.

All the normal runs are carefully checked offline and a list of bad runs/subruns is complied. Such bad runs/subruns are removed in data analysis. Firstly, runs with less than 5 minutes long data and subruns with less than 30 seconds long data are rejected. Secondly, runs with hardware or software trouble are removed. Thirdly, runs or subruns with event clusters or strange trigger rates are regarded as bad and thus removed. The remaining data are then processed by the reduction steps discussed in the rest of this chapter.

9.2 First Reduction

The first reduction consists of a number of loose cuts to eliminate the apparent non-e^+ events. The main criteria for the first reduction are the following:

Calibration event cut: Calibration (e.g. LED, laser) and pedestal data are taken regularly even during the normal data taking. These events are indicated by special trigger flags and are removed.

OD cut: Events resulting from the $\bar{\nu}_e$ interactions in FV should have no OD trigger. An OD trigger indicates a charged particle enters the detector from outside. Hence, events with an OD trigger are removed. In addition, events with more than 19 OD hits are also rejected, regardless of whether the OD trigger is present. Such events can occur if the OD DAQ has a trouble.

Time difference cut: It is required that an event should occur at least 50 μs after the previous LE triggered event. This time difference cut is mainly to remove the decay electrons from cosmic ray muons and "ringing" noise events that typically follow the very energetic muons. For the SK-IV data analysis, the untagged muons (see section 4.4) are also taken into account when calculating the time difference to the previous event.

Noise event cut: PMT hits induced by electric noise tend to have a small charge. To characterize the noise events, a noise ratio is defined as the fraction of PMT hits with $|Q| < 0.5$ p.e.. Events with a noise ratio greater than 0.55 are rejected.

Fiducial volume cut: Many low energy events are reconstructed close to the ID wall. Most of these events originate from the detector material and the surrounding rock. To remove this background, a fiducial volume cut is applied to reject events that are reconstructed less than 200 cm from the ID wall. The fiducial volume defined by this cut is 22.5 kton.

Goodness cut: The goodness value G_V returned by BONSAI indicates the quality of the vertex reconstruction. The calculation of G_V is based on the PMT hit timings. Another goodness quantity, DirKS, evaluates the PMT hit pattern in space. The DirKS measures the azimuthal uniformity in the Cherenkov ring pattern. These two goodness values are combined to form a cut called ovaQ (One dimensional variable of Vertex and Angular reconstruction Quality) [98], which is defined as:

$$\mathrm{ovaQ} = G_V^2 - \mathrm{DirKS}^2. \tag{9.1}$$

Events with a ovaQ less than 0.25 are removed.

9.3 Spallation Cut

The remaining events after the first reduction are dominated by the comic ray muon induced spallation products. When energetic muons pass through the detector, they can spall oxygen nuclei, producing unstable isotopes. Table 9.1 lists possible radioactive isotopes induced by cosmic ray muons at SK. The β decay products from these isotopes can be reconstructed as e^+ candidates. In particular, some isotopes have a β-n decay mode, which can mimic an anti-neutrino signal. The maximum kinetic energy of spallation events is 20.6 MeV. Considering the energy resolution effects, all events reconstructed below 24 MeV are applied with the spallation cut.

Removing the spallation background is perhaps the most difficult task in the data reduction. The basic idea to determine spallation is to look for correlations between the e^+ candidate and the proceeding muon tracks. There are four variables used in searching for the spallation activity:

dt: The first variable, dt, is the time difference between the e^+ candidate and the proceeding muon, which is very powerful in identifying short-lived spallation products. The smaller the dt, the greater the likelihood that an event being spallation.

$\mathbf{L_{tran}}$: The second variable, $\mathrm{L_{tran}}$, is the transverse distance from the e^+ candidate to the muon track. The isotopes are created along the muon track and in general cannot travel far before decaying. A short $\mathrm{L_{tran}}$ indicates spallation.

$\mathbf{L_{long}}$: The third variable, $\mathrm{L_{long}}$, is the distance from the dE/dx peak to where the e^+ candidate lies on the muon track (see Fig. 9.1). As mentioned in section 4.4, spallation causing muons tend to peak at the spallation occurring location in their dE/dx plot. Spallation events tend to have a smaller $\mathrm{L_{long}}$.

Table 9.1: Possible radioactive isotopes induced by cosmic ray muons at SK.

Isotope	$\tau_{1/2}$	Decay mode	Kinetic energy (MeV)
${}^{11}_{3}$Li	0.0085	β^- $\beta^- + n$	20.62 $\sim$16
${}^{13}_{8}$O	0.0090	$\beta^+ + p$	8$\sim$14
${}^{12}_{7}$N	0.0110	β^+	16.38
${}^{14}_{5}$B	0.0138	β^-	14.55+6.09(γ)
${}^{13}_{5}$B	0.0174	β^-	13.44
${}^{12}_{5}$B	0.0202	β^-	13.37
${}^{12}_{4}$Be	0.0236	β^-	11.71
${}^{8}_{2}$He	0.119	β^- $\beta^- + n$	9.67+0.98(γ)
${}^{9}_{6}$C	0.127	$\beta^+ + p$	3$\sim$15
${}^{9}_{3}$Li	0.178	β^- $\beta^- + n$	13.6 $\sim$10
${}^{16}_{6}$C	0.747	$\beta^- + n$	$\sim$4
${}^{8}_{5}$B	0.77	β^+	$\sim$13.9
${}^{8}_{3}$Li	0.84	β^-	$\sim$13.0
${}^{15}_{6}$C	2.449	β^- β^-	9.77 4.51+5.30(γ)
${}^{16}_{7}$N	7.134	β^- β^-	10.44 4.27+6.13(γ)
${}^{11}_{4}$Be	13.8	β^- β^-	11.51 9.41+2.1(γ)

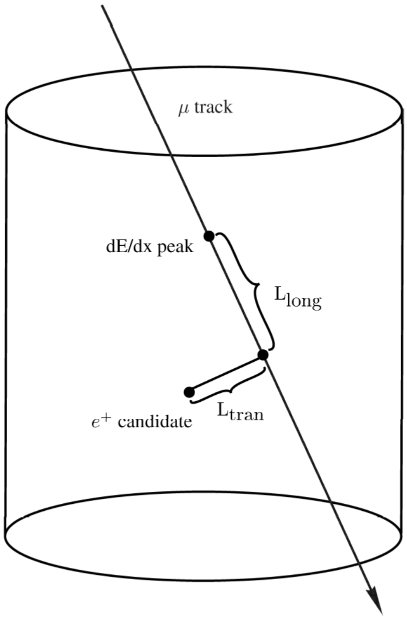

Figure 9.1: Illustration of the definition of L_{tran} and L_{long} for a spallation activity induced by a cosmic ray muon.

Q_{peak}: The last variable, Q_{peak}, is the amount of light deposited around the dE/dx peak. Strong peaks in the dE/dx plot usually indicate spallation.

9.3.1 The Spallation Likelihood

The primary method to identify a spallation activity is to use a likelihood constructed from the four variables described above. Muons are divided into categories according to the Muboy fit results: single-through going, stopping, multiple muons with a single track and multiple muons with more than one tracks. Likelihood functions are provided for each muon type.

All proceeding muons within 30 seconds of the event time of the e^+ candidate are checked for correlations. The muons occuring before the candidate event is used as the spallation sample. And the muons occuring within 30 seconds after the candidate event which are used to evaluate the random correlation is used as the random sample. Distributions of the four variables, dt, L_{tran}, L_{long}, and Q_{peak}, are first made separately for the spallation sample and random sample. Distributions obtained from the random sample represent the random correlations. Spallation correlations are obtained by subtracting the random sample distributions from the spallation sample distributions.

Fig. 9.2 shows both the spallation correlations and the random correlations for the single through-going muons.

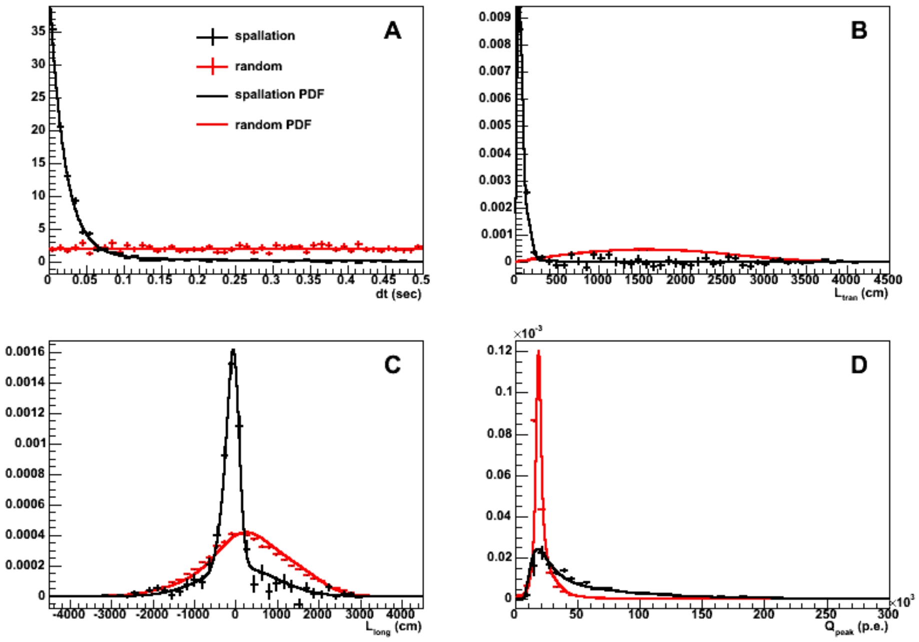

Figure 9.2: Distributions of the spallation likelihood variables dt (A), L_{tran} (B), L_{long} (C), and Q_{peak} (D) for the single through-going muons.

Both the spallation and random correlations are then parameterized by analytic functions, which are used as PDFs to make the spallation likelihood. The PDFs for the single through-going muons are also shown in Fig. 9.2. For each muon that to be checked, an initial full likelihood is calculated as:

$$L = \sum_i \log \frac{\mathrm{PDF}^i_{\mathrm{spall}}}{\mathrm{PDF}^i_{\mathrm{random}}}, \tag{9.2}$$

where i runs over dt, L_{tran}, L_{long}, and Q_{peak}. Fig. 9.3 shows the distributions of the spallation likelihood for the single through-going muons.

In addition to the standard likelihood utilizing all the four variables, other likelihood functions are also used for special cases. For example, if the dE/dx profile is found to have a bad quality, then the dE/dx information is not used. In this case, a likelihood function constructed from only dt and L_{tran} will be used. For the multiple muons with more than one tracks, each track will be examined.

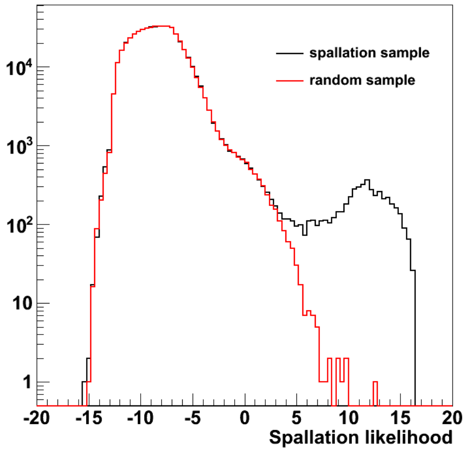

Figure 9.3: Distributions of the spallation likelihood for the single through-going muons.

9.3.2 Applying the Spallation Cut

Spallation events are rejected primarily using the spallation likelihood value. A likelihood threshold is determined for each muon type. In addition, some cuts on specific quantities are also present. For example, if the goodness of both Muboy and BFF fit for a single through-going muon is poor, the detector is vetoed for 2 seconds. The spallation cuts are tighter for e^+ candidate below 18 MeV than that above 18 MeV, as there are more longer lived spallation products at lower energies. A detailed description of the spallation likelihoods and the cut criteria can be found in Ref. [96].

The spallation cut was originally tuned for the SRN analysis using SK-I/III data. It is confirmed that SK-IV distributions are very similar to SK-I/III data, so the same likelihood and cut criteria are adopted for this analysis. Fig. 9.4 shows the correlations after applying the spallation cut, where no statistically significant spallation events can be seen in the remaining data[1].

To evaluate the inefficiency of the spallation cut, a position dependent inefficiency map is made using data. The overall inefficiency is obtained using the inefficiency map and the MC vertex distribution. The efficiencies

---

[1] The spallation cut was initially optimized in attempting to completely eliminate spallation events above 16 MeV. It's impractical to remove all spallation events at lower energies because of the long lived isotopes. But it is expected that the performance of the spallation cut can be somewhat improved for analysis below 16 MeV and worth further investigation.

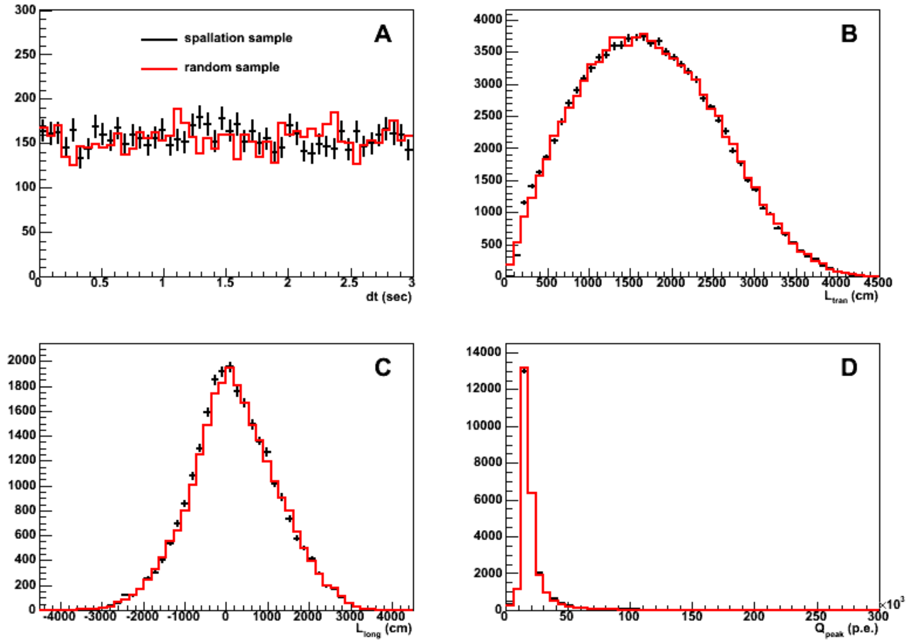

Figure 9.4: Distributions of the spallation likelihood variables dt (A), L_{tran} (B), L_{long} (C), and Q_{peak} (D) for the single through-going muons after applying the spallation cuts. No discernible spallation events remain.

for events below and above 18 MeV is 82.6% and 91.3%, respectively.

9.4 External Event Cut

External gamma rays and radioactivity from the detector material can be reconstructed inside the FV. This background can be recognized by the inward going direction. To reject this background, an effective distance from the wall, d_{eff}, is calculated using the reconstructed vertex and direction (see Fig. 9.5). Small d_{eff} indicates that an event comes from outside of the FV. The distribution of d_{eff} is shown in Fig. 9.6. All events with $d_{\text{eff}} < 300$ cm are rejected. For events below 22 MeV, a tighter cut $d_{\text{eff}} > 450$ is applied.

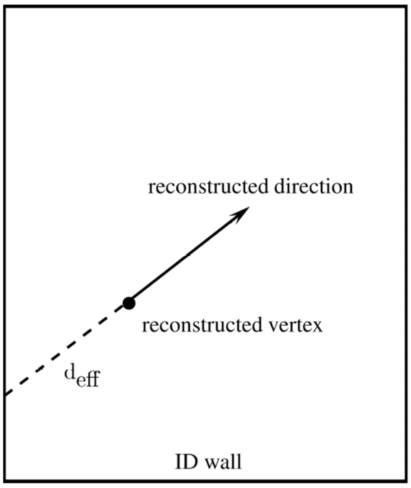

Figure 9.5: Illustration of the definition of d_{eff}.

9.5 Solar Cut

Electrons elastically scattered by solar ν_e's are a background to this analysis. The distinctive feature of solar ν_e events is that they carry the direction information of the incident ν_e's. To reject solar ν_e events, we can utilize the angle, θ_{sun}, between the reconstructed event direction and the expected ν_e direction calculated from the position of the Sun at the event time. Although solar ^{8}B ν_e's have an energy less than 16 MeV (the endpoint of *hep* neutrino spectrum is 18.77 MeV), the scattered electrons can be reconstructed up to 20 MeV due to the energy resolution effects. Therefore, all the events reconstructed below 20 MeV are applied with this solar cut. Fig. 9.7 shows

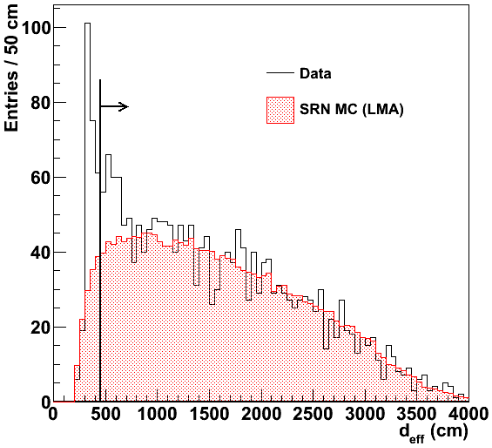

Figure 9.6: The distribution of d_{eff}. Solid histogram indicates data, while shaded histogram represents the MC of SRN (LMA model).

the distribution of $\cos\theta_{\mathrm{sun}}$ for the events below 20 MeV. The strong peak near $\cos\theta_{\mathrm{sun}} = 1$ indicates elastic scattering solar ν_e events. Events that have $\cos\theta_{\mathrm{sun}} > 0.9$ are rejected. There are still some solar events remain in the data sample, as can be seen from the $\cos\theta_{\mathrm{sun}}$ distribution. But this is not a problem in searching for $\bar{\nu}_e$, since solar ν_e events do not have a delayed 2.2 MeV γ.

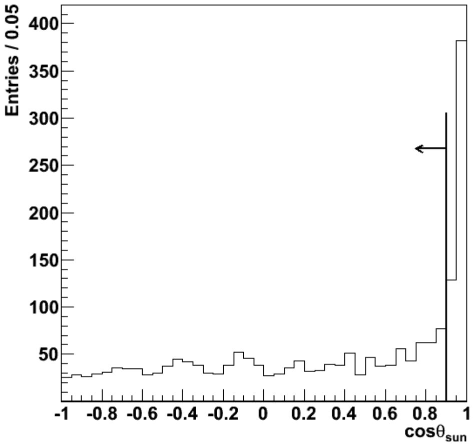

Figure 9.7: Distribution of $\cos\theta_{\mathrm{sun}}$ for events below 20 MeV.

9.6 Cherenkov Angle Cut

Low momentum heavy particles (mainly muons) created by atmospheric neutrinos can be reconstructed in the relevant energy region. Fig. 9.8 shows the muon momentum versus the electron equivalent energy reconstructed by BONSAI. Such muons are not ultra-relativistic particles, and hence should have a smaller Cherenkov angle (see section 4.5) than that of the electrons ($\sim 42°$). Fig. 9.9 shows the Cherenkov angle versus the reconstructed energy for muons using the atmospheric neutrino Monte Carlo sample.

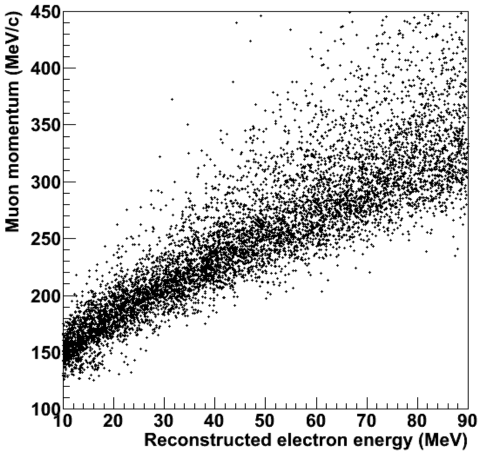

Figure 9.8: A 2-D plot of the muon momentum versus the reconstructed electron energy. The sample is from the atmospheric neutrino Monte Carlo.

The Cherenkov angle cut also rejects multiple γ-ray events induced by neutral current atmospheric neutrino interactions. Events caused by the multiple γ-rays tend to have a larger Cherenkov angle (see section 4.5). In addition, events consist of an electron and a γ exhibit a similar hit pattern. Therefore, the Cherenkov angle cut is also useful in further removing spallation events that are due to a beta decay plus a γ emission (see Table 9.1).

Fig. 9.10 shows the Cherenkov angle distribution for data and SRN MC. Muons, electrons, and gammas are clearly separated. Events with the Cherenkov angle less than 38 degree or larger than 50 degree are eliminated.

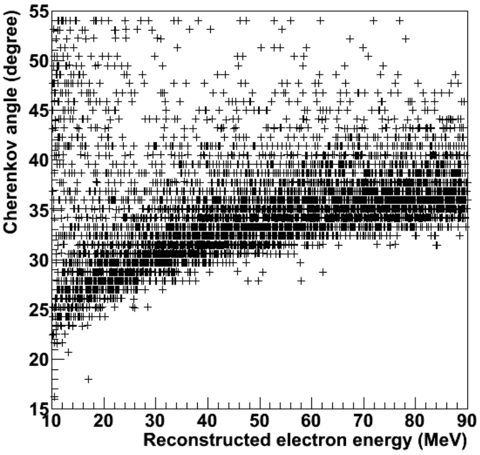

Figure 9.9: A 2-D plot of the Cherenkov angle versus the reconstructed electron energy for muons using the atmospheric neutrino Monte Carlo. Due to the kinematics constrains, the Cherenkov angle of the muons should be less than 38 degree. Some muons are reconstructed with a larger Cherenkov angle in the following cases:1) The number of PMT hits is too small to reconstruct the Cherenkov angle correctly; 2) A de-excitation γ is emitted in the interaction of a muon with an oxygen nucleus; 3) The muon is too close to the detector wall.

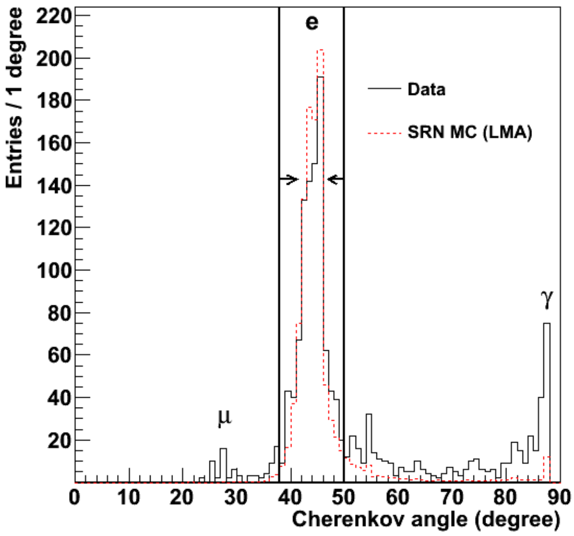

Figure 9.10: Distributions of the Cherenkov angle for data (solid) and SRN MC (dashed). From left to right, the three peaks correspond to muons, electrons and gammas.

9.7 Pre-/post Activity Cut

The candidate event should have a single timing peak, if we ignore the 2.2 MeV γ for the moment. Events with interactions closely before or after the main timing peak identified by BONSAI should be removed. We use a 15 ns sliding window to search for a possible second timing peak in the residual time distribution. If the number of hits in the 15 ns window (N_{15}) exceeds the threshold, the event is rejected. This cut mainly removes events induced by atmospheric muon neutrinos.

Most muons are removed by the Cherenkov angle cut. But if the muon and the decay electron are close in time and the muon generates less hits than the electron does, BONSAI may fit the electron timing peak. In this case, the Cherenkov angle is reconstructed for the decay electron and will survive from the Cherenkov angle cut. Such events can be recognized by looking for a muon timing peak before the electron timing peak. Fig. 9.11 shows the event display for such an event. In addition, in rare cases the Cherenkov angle of the muon can be misreconstructed above 38 degree. Such events can be rejected by looking for an electron timing peak after the muon timing peak.

A muon with an energy below the Cherenkov threshold emits no light

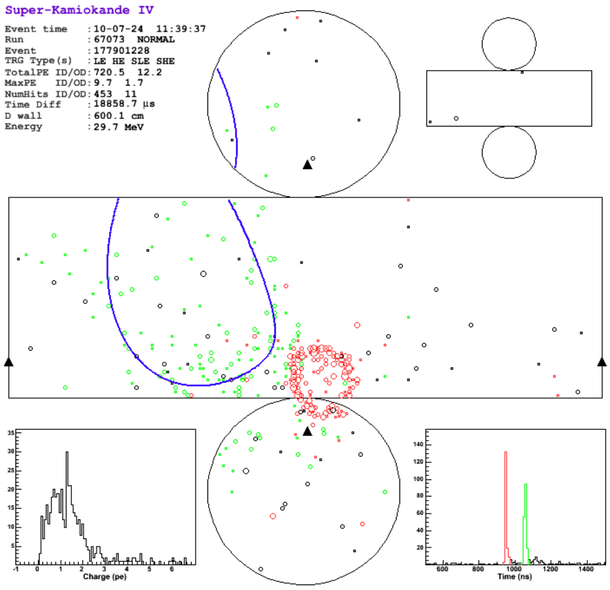

Figure 9.11: Event display for a typical μ-e decay event. The two timing peaks correspond to the parent muon and the decay electron, respectively. The decay electron is reconstructed by BONSAI.

and hence is invisible to the detector. The decay electrons from invisible muons are the major background in the previous SRN searches [83]. Such decay electrons can still be traced if a prompt γ is emitted after the muon neutrino interacts with the oxygen nucleus. Since the lifetime of the muon is 2.2 μs, a prompt γ may exist previous to the decay electron within a few μs. Fig. 9.12 shows the event display for a typical event of this type.

The wider event gate in SK-IV makes it ideal to catch possible pre-/post activities. The 5 μs data before the main timing peak cover ~90% of the prompt γ's. The 35 μs data after the main timing peak contain all the decay electrons. The entire 40 μs data pack is searched for a second timing peak. Fig. 9.13 shows the N_{15} distribution before (left) and after (right) the main timing peak. Events with N_{15} greater than 11 (19) before (after) the main timing peak are rejected. The post-activity cut is looser for three reasons: first, the size of the data after the main timing peak is larger and hence the maximum N_{15} has a larger chance to fluctuate to a higher value; second, the decay electron is expected to generate a larger amount of hits than the prompt γ does; third, a 2.2 MeV γ may exist after the main timing peak.

The inefficiency of the pre-post activity cut is evaluated using the dummy data and is 0.2%.

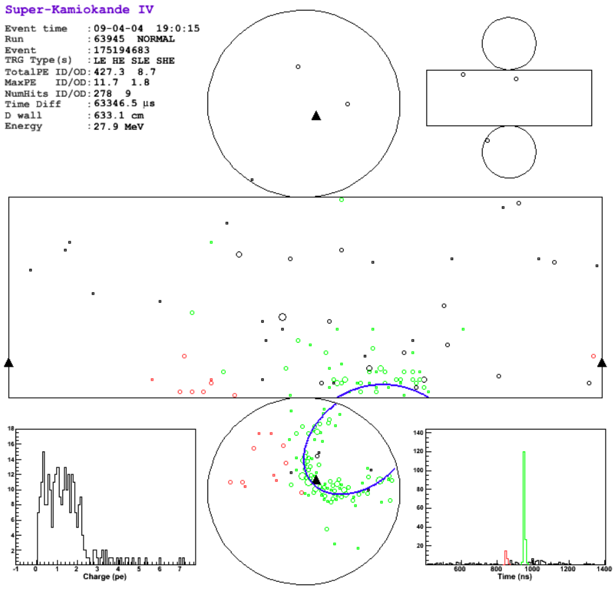

Super-Kamiokande IV

Event time : 09-04-04 19:0:15
Run : 63945 NORMAL
Event : 175194683
TRG Type(s) : LE HE SLE SHE
TotalPE ID/OD: 427.3 8.7
MaxPE ID/OD: 11.7 1.8
NumHits ID/OD: 278 9
Time Diff : 63346.5 µs
D wall : 633.1 cm
Energy : 27.9 MeV

Figure 9.12: Event display for a decay electron, the parent muon of which is invisible. The small timing peak before the electron corresponds to the de-excitation γ-ray.

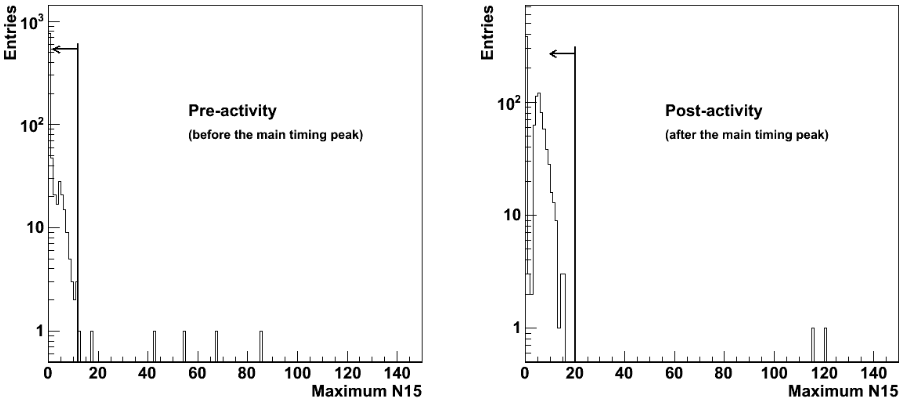

Figure 9.13: Distributions of the maximum N_{15} before (left) and after (right) the main timing peak.

9.8 Pion Cut

Some events in the data sample are atmospheric neutrino induced pions with higher momentum than those rejected by the Cherenkov angle cut (see section 4.5). The pion likelihood π_{like} described in section 4.5 is used to reject such pion events. Fig. 9.14 shows the distribution of π_{like} for data and SRN MC. Events with $\pi_{\mathrm{like}} > 0.58$ are rejected.

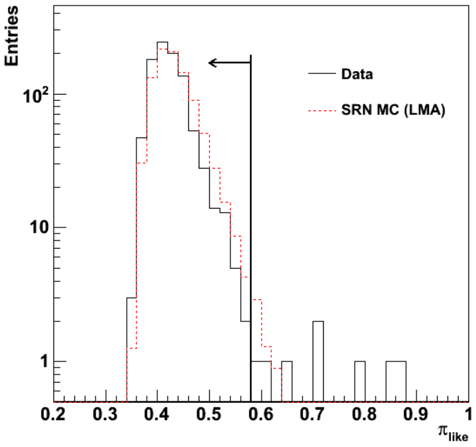

Figure 9.14: Distribution of π_{like}.

9.9 Multi-ring Cut

Atmospheric neutrino interactions with water may create multiple charged particles at the same time. Such events will survive from the pre-/post activity cuts since all the particles share a common timing peak. This background can be eliminated by looking for multiple Cherenkov rings. To that end, we adopt the same ring counting tools as that are used in the ATMPD analysis [106], which return the number of rings and the direction of each ring. Sometimes a fuzzy electron ring can be mis-treated as two distinctive rings, especially for the low energy events. In such case, the directions of the two rings are typically very close to each other. To reduce inefficiency due to a ring miscounting, we calculate the opening angle, θ_{ring}, between the directions of the two rings. Only events with $\theta_{\mathrm{ring}} > 60°$ are removed.

9.10 μ/π Cut

It has been known that there are still a small amount of muons and pions ($\sim$ 2 events per year between 10–90 MeV) remaining in the data sample even with all the above cuts applied. Prior to this work, these leftover μ/π's were regarded as an irreducible background [96]. It is observed in this analysis that these μ/π events can be differentiated from electrons using the charge information. We calculate the total charge of an event using the PMT hits with residual time within a 50 ns window (Q50) and define the average hit p.e. as the ratio of Q50 and N50. Fig. 9.15 shows a 2-D plot of Q50/N50 versus the reconstructed electron energy for μ, π and e using the atmospheric neutrino Monte Carlo. It is clear that the Q50/N50 of μ/π events are significantly larger than that of the electron. Events with Q50/N50 greater than 2.2 are removed. Fig. 9.16 shows the event display of a typical μ/π event rejected by this cut.

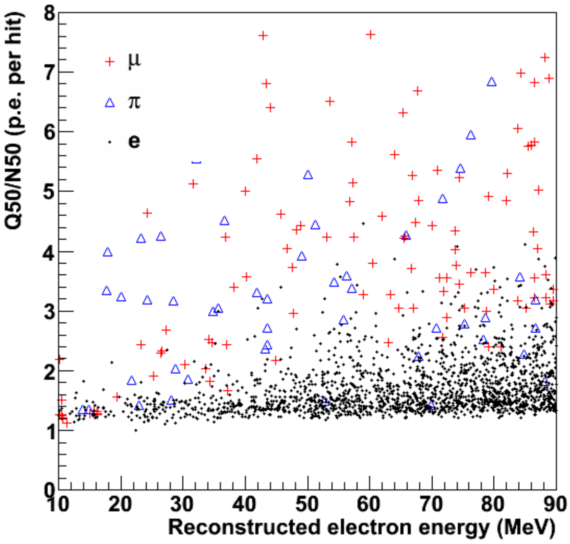

Figure 9.15: Distribution of Q50/N50 versus reconstructed electron energy for μ (cross), π (triangle) and e (dot) from the atmospheric neutrino Monte Carlo.

9.11 Reduction Summary

The final energy spectrum of e^+ candidates is shown in Fig. 9.17. After all reductions, the data sample still consists of a lot of spallation events and

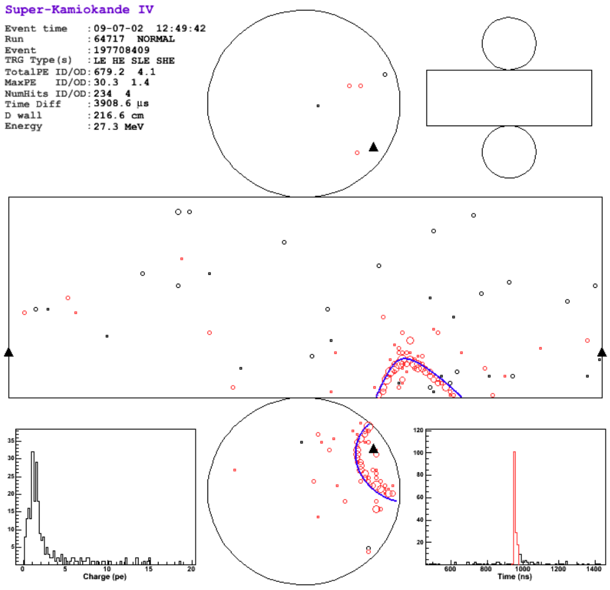

Figure 9.16: Event display of a typical μ/π event. The Q50/N50 value of this event is 3.5.

solar neutrino events. Since no neutrons are produced in these events[2], they do not pose a serious problem for the $\bar{\nu}_e$ search.

On the other hand, atmospheric neutrino events should be removed as much as possible, especially muons and pions, because such events are likely to be accompanied by neutrons (see section 10.2). Unfortunately, there are at least three types of atmospheric neutrino backgrounds remaining in the data sample: NC γ-rays, decay-e from invisible muons and $\nu_e/\bar{\nu}_e$ CC events. A detailed description of the atmospheric neutrino background can be found in Ref. [96].

Most cut efficiencies are evaluated using the Monte Carlo. The efficiency of the spallation cut is calculated using the inefficiency map, which is made from the data, and the vertex distribution of the Monte Carlo. The efficiency of the pre-/post activity cut is calculated using the dummy data. Table 9.2 show the number of events after each cut and the efficiency of that cut. For the SRN analysis, the energy range is 12–30 MeV, while for the solar $\bar{\nu}_e$ analysis, the energy range is 12–20 MeV.

---

[2] There are a few isotopes that have βn decay modes (see Table 9.1), which can mimic the inverse beta decay reaction chain. However, most such spallation events either are removed by the spallation cut due to the short lifetime of the parent isotope or have a too low energy to contaminate the final data sample.

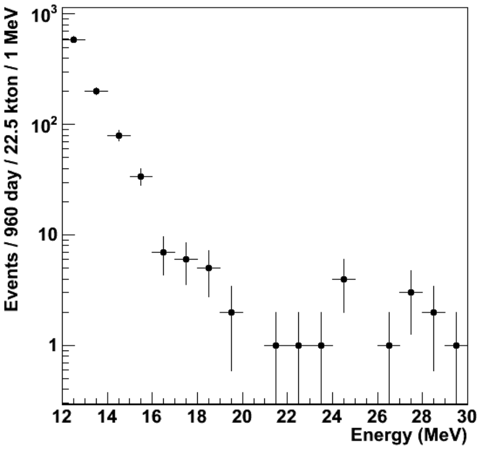

Figure 9.17: Energy spectrum of e^+ candidates after all reductions.

Table 9.2: Summary of reductions steps. The number of events after each cut and the efficiency of that cut are listed.

	SRN (12–30 MeV)		Solar (12–20 MeV)	
Reduction step	# of events	Efficiency	# of events	Efficiency
First reduction	49288	>99%	49082	>99%
Spallation cut	2417	86.7%	2249	82.6%
External event cut	2148	94.6%	1987	92.6%
Solar cut	1625	95.0%	1476	94.5%
Chenrekov angle cut	983	91.6%	939	87.0%
Pre-/post activity cut	951	99.8%	933	99.8%
$\pi_{\rm like}$ cut	940	99.2%	925	99.6%
Multi-ring cut	935	99.3%	920	99.7%
μ/π cut	934	99.8%	920	100.0%
Total efficiency	-	70%	-	62%

Chapter 10

Data Analysis and Results

This chapter presents an analysis of the neutron production in the low energy data and the searches of supernova relic neutrinos and solar $\bar{\nu}_e$'s.

10.1 Efficiencies and Systematic Uncertainties

To identify $\bar{\nu}_e$'s via the inverse beta decay reaction, a search of the 2.2 MeV γ is conducted after each e^+ candidate in the final sample obtained in the previous chapter. The first 2 μs data following the prompt e^+ are excluded to avoid overlapping with the e^+ event. Therefore, the data size used for the 2.2 MeV γ search is 535 μs, covering $\sim$92% of all the neutron captures. The neutron tagging efficiency presented in section 6.4 should be corrected by a factor of $\sim$92%, resulting in an efficiency of $\epsilon_n = 17.8\%$ to observe the 2.2 MeV γ in the time window $2 - 535$ μs.

The dominant contribution to the systematic uncertainty on ϵ_n comes from the position dependence. Since the inverse beta decay events are rare, any possible non-uniformity of the neutron tagging efficiency must be taken into account. The position dependence of ϵ_n is evaluated by dividing the FV into 10×11 cells (see section 6.4). The 1-σ uncertainty is found to be 1%.

The 1% accidental background probability shown in section 6.4 is for 500 μs data, which can be scaled to calculate a different size of data since the background probability is flat in time. So the accidental background probability for 535 μs data is $P_b = 1.07\%$. The position dependence and the time variation can induce a (relative) 10% uncertainty on the background probability. The primary events are uniformly distributed in the FV and in the operation period. Therefore, the systematic uncertainty on the background probability is negligible. To be conservative, we assign a (relative)

10% uncertainty to the background probability.

The efficiency of the primary event (ϵ_{e^+}) is given in Table 9.2. Systematic uncertainties on ϵ_{e^+} originate from the fiducial volume (1%), the live time calculation (0.1%), the inverse beta decay cross section (1%) and the data reduction (3.1%). The uncertainty on data reduction is quoted from the previous SRN study [96] since the cuts used are very similar. Individual contributions are added in quadrature and the total uncertainty on ϵ_{e^+} is rounded to 4%. The total efficiency of observing an inverse beta decay signal ($\epsilon_{\text{tot}} = \epsilon_{e^+} \cdot \epsilon_n$) and its systematic uncertainty are listed in Table 10.1.

Table 10.1: Total efficiency of observing an inverse beta decay signal.

Signal	ϵ_{tot}	Sys. uncertainty
SRN	0.125	0.011
Solar	0.110	0.010

10.2 Neutron Production in Low Energy Data

This section provides a general description of neutron production in the low energy data at SK. The event signature of the IBD reaction is very clear, so we will focus on the non-IBD events, i.e. events in the side bands. Since the neutron production in the side bands are much more complicated and difficult to quantify, our discussion is rather qualitative.

We first examine two types of events rejected by the Cherenkov angle cut: the μ-like events (Cherenkov angle $< 38°$) and the isotropic events (Cherenkov angle $> 50°$). Table 10.2 lists the number of primary events, the expected accidental background and the number of observed neutrons for both types of events. Fig. 10.1 (10.2) shows the number of observed neutrons as a function of the reconstructed electron energy of the primary μ-like (isotropic) event. A clear excess of neutron candidates is observed in both types of events. Fig. 10.3 shows the time difference between the delayed event and the primary event (ΔT), which is fit by an exponential distribution with $\tau = (195.4 \pm 47.8)\mu$s. The exponential structure of ΔT confirms that the delayed signal is indeed the 2.2 MeV γ released in neutron captures.

Obviously, muon anti-neutrinos can produce neutrons through

$$\bar{\nu}_\mu + p \rightarrow \mu^+ + n. \tag{10.1}$$

Among all μ-like events, μ^+ (created by $\bar{\nu}_\mu$) accounts for about 30%. Therefore, ∼40 neutrons are produced via reaction (10.1). But reaction (10.1) is

Table 10.2: Number of neutrons observed in the side bands.

Event type	Primary events	Accidental bkg.	Observed neutrons
μ-like	140	1.48	21
Isotropic	487	5.14	46

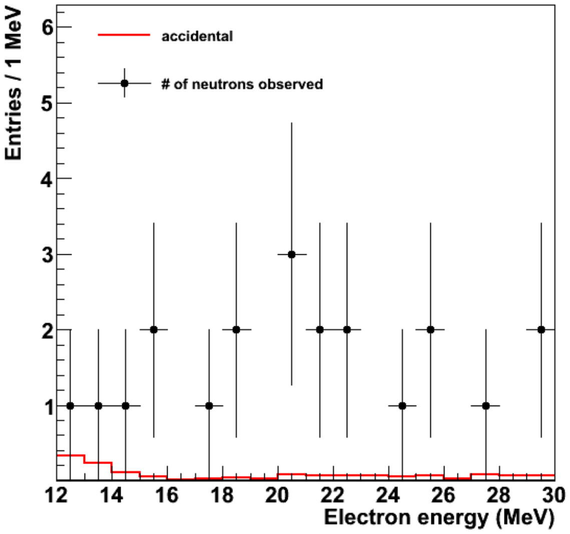

Figure 10.1: Neutrons observed in the μ-like events as a function of the reconstructed electron energy.

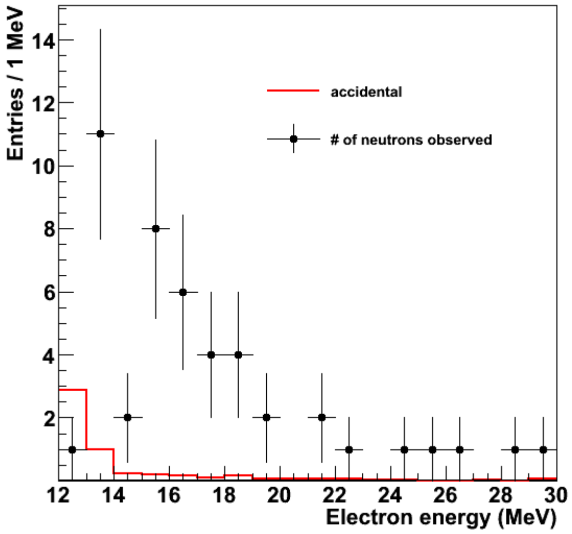

Figure 10.2: Neutrons observed in the isotropic events as a function of the reconstructed electron energy.

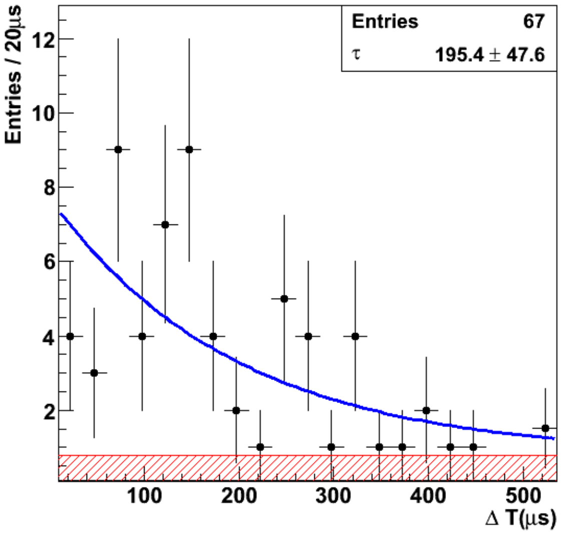

Figure 10.3: Distribution of neutron capture time observed in the μ-like events and the isotropic events. Shaded histogram indicates the expected accidental background. Curve shows the unbinned maximum likelihood fit to data.

not the only source of neutrons in the μ-like events. Taking into account the neutron tagging efficiency, there should be about 110±25 neutrons produced in the 140 μ-like events. Therefore some other processes must contribute to the neutron production. The incident muon neutrino may undergo the following interactions:

$$\bar{\nu}_\mu + {}^{16}O \rightarrow \mu^+ + {}^{16}O + \pi^-, \tag{10.2}$$

$$\nu_\mu + {}^{16}O \rightarrow \mu^- + {}^{16}O + \pi^+. \tag{10.3}$$

If the pions produced in these reactions are absorbed in the oxygen, protons and neutrons might be ejected out of the oxygen. Furthermore, pions are likely to produce neutrons when propagating in water. When a μ^- gets captured, neutrons can be produced via the following reaction chain:

$$\mu^- + {}^{16}O \rightarrow \nu_\mu + {}^{16}N^*, \tag{10.4}$$

$${}^{16}N^* \rightarrow {}^{15}N({}^{14}N) + n(2n). \tag{10.5}$$

Also π^- capture on ${}^{16}O$ can result in neutron production.

The isotropic events with energy below 14 MeV are dominated by spallation products (see section 9.6). If we consider events above 14 MeV only, the data suggests that 184±33 neutrons are produced in the 122 isotropic events. The isotropic events mainly originate from the NC neutrino interactions. The most important process is the NC elastic scattering:

$$\nu + n \rightarrow \nu + n, \tag{10.6}$$

Gamma-rays and secondary neutrons can be produced when the energetic outgoing neutron interacts with water. Here the γ-rays serve as the primary event.

Besides the μ-like events and the isotropic events, neutrons are also found in the events rejected by the pre-/post activity cut, the π_{like} cut, the multi-ring cut and the μ/π cut. Since none of these cuts are 100% effective, a small leakage of the atmospheric neutrino events in the signal region may cause a problem when applying neutron tagging to search for $\bar{\nu}_e$'s. The known major background components in the final sample are: decay-e from the invisible muon(created in $\nu_\mu/\bar{\nu}_\mu$ CC), $\nu_e/\bar{\nu}_e$ CCQE and NC elastic process. A quantitative treatment of neutron yield in these backgrounds requires an accurate simulation of neutron production and propagation in water. Unfortunately, some relevant processes are omitted in the current SK Monte Carlo, because the 2.2 MeV γ was previously not observable at SK. A complete simulation regarding the neutron production and propagation in water is eagerly awaited.

Even with the qualitative discussions presented above, two important conclusions can be drawn. First, the neutron correlated CC backgrounds are not limited to the $\bar{\nu}_e$ and $\bar{\nu}_\mu$ CCQE processes. Neutrons can be produced in other CC reactions and both the neutrino and the anti-neutrino may contribute. Second, the NC elastic events are a very important background with a high neutron yield. The NC elastic background is particularly dangerous because they lie in the energy region where the SRN interactions most likely to occur.

As a closing remark to this section, we emphasize that there are some important differences between the atmospheric neutrino backgrounds and the true inverse beta decay signal. The signal of interest is $\bar{\nu}_e$'s with energy $\lesssim$30 MeV, which interact primarily with free protons. The outgoing neutron has a very low momentum and will be captured within $\sim$20 cm. The neutrons produced in the atmospheric neutrino backgrounds, on the other hand, typically have a momentum of a few hundreds of MeV/c, which can travel a significant larger distance before being captured. Therefore, if the vertex of the neutron capture event can be precisely reconstructed, the displacement of the neutron capture vertex can be used to differentiate atmospheric neutrino backgrounds from the true inverse beta decay signal. Furthermore, atmospheric neutrino backgrounds, especially the NC background, are often accompanied by multiple neutrons. Hence, atmospheric neutrino backgrounds can be further rejected if all the produced neutrons are detected.

10.3 Search for Low Energy $\bar{\nu}_e$'s

In the e^+ candidate sample obtained in the previous chapter, 14 neutrons are observed out of 12 events. Fig. 10.4 shows the energy distribution for the 12 primary events with neutron(s) tagged, which is consistent with the expected accidental background. In absence of a $\bar{\nu}_e$ signal, the upper limits will be set at the 90% confidence level.

As discussed in the previous section, there are also atmospheric neutrino induced backgrounds. Such backgrounds are difficult to quantify and will be neglected in this analysis. Only the accidental background is considered for setting the upper limits, rendering the results conservative.

Due to the limited statistics, there is no way to model a reliable PDF for the accidental background. So a spectral fitting is impractical in this case. Instead, we adopt a simple counting method and set the upper limits based on Poisson statistics. The number of primary e^+ candidates (N_{e^+}, see Table 9.2), the number of expected accidental background ($n_{\mathrm{bkg}} = N_{e^+} \times P_b$) and the number of observed delayed signal (n_{obs}) are shown in Table 10.3.

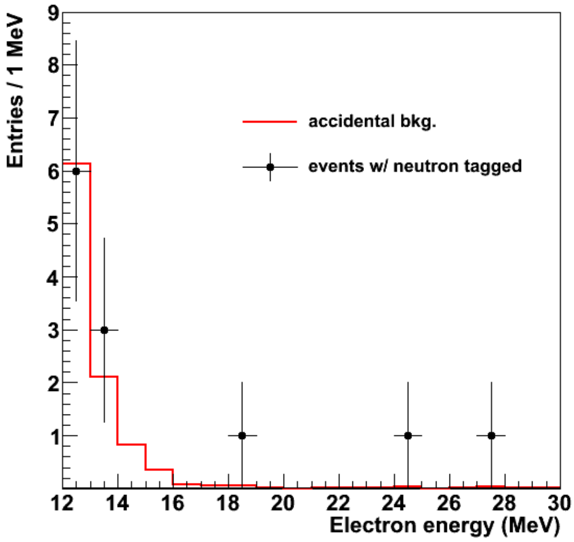

Figure 10.4: Energy distribution of the candidates. Dots show the observed events with at least one neutron tagged. The histogram represents the expected accidental background.

The upper limits are computed using the Rolke method [107], which uses the profile likelihood to handle uncertainties on the background expectation and the efficiency. Specifically, the limit is calculated using TRolke[1], which takes as inputs n_{obs}, n_{bkg}, uncertainty on n_{bkg} (our generous 10% uncertainty increases the limit by only ∼2%), ϵ_{tot} and uncertainty on ϵ_{tot}.

Table 10.3: Number of observed candidates and expected background.

	N_{e^+}	n_{bkg}	n_{obs}
SRN (12–30 MeV)	934	10.0	12
Solar (12–20 MeV)	920	9.8	10

10.3.1 Supernova Relic Neutrinos

The efficiency-corrected 90% C.L. upper limit is calculated to be $N_{90} = 71.5$ events for the SRN $\bar{\nu}_e$ signal. This can be translated into a limit on the annual event rate:

$$N'_{90} = N_{90} \times \frac{365\,\text{days}}{\text{live time}} = 27.2\,\text{events} \,/\, 22.5\,\text{kton} \cdot \text{year}, \tag{10.7}$$

---

[1] A tool available in ROOT [108].

where the live time is 960 days.

The upper limit on the SRN flux F_{90} can be derived from $N_{90}^{'}$ using the following simple relation:

$$\frac{F_{90}}{F_{\rm model}} = \frac{N_{90}^{'}}{N_{\rm prediction}}, \tag{10.8}$$

where $F_{\rm model}$ is the total flux of a certain model and $N_{\rm prediction}$ is the predicted annual event rate in the energy range of 12 MeV $< E_{e^+} <$ 30 MeV. From Table 5.1, the annual event rate predicted by the LMA model and the HBD 6 MeV model is 4.15 and 4.36 events/22.5 kton · year, respectively. Therefore,

$$F_{90} = \frac{27.2}{4.15} \times F_{\rm LMA} = 6.5 \times F_{\rm LMA}, \tag{10.9}$$

or

$$F_{90} = \frac{27.2}{4.36} \times F_{\rm HBD\ 6\ MeV} = 6.2 \times F_{\rm HBD\ 6\ MeV}. \tag{10.10}$$

This limit is 2.2 times smaller than that obtained by KamLAND [79][2], the largest operating low energy anti-neutrino detector.

The current most stringent limit on the SRN flux is obtained from the SK-I/II/III data by searching for e^+ singles above 16 MeV. The combined limit is only ∼2 times of the model prediction [96]. Although our limit is less stringent, this is the first time at SK that the analysis goes below 16 MeV using a coincident detection technique.

10.3.2 Solar $\bar{\nu}_e$

For solar $\bar{\nu}_e$, the upper limit on the annual event rate is

$$N_{90}^{'} = 22.7\,\text{events} \,/\, 22.5\,\text{kton} \cdot \text{year}. \tag{10.11}$$

From Table 5.2, the expected annual event rate is 503 events/22.5 kton · year assuming 1% $\nu_e \to \bar{\nu}_e$ conversion probability. The $\bar{\nu}_e$ flux upper limit is

$$F_{90} = \frac{22.7}{503} \times 10^{-2} \times F_{\rm BP04} = 4.5 \times 10^{-4} \times F_{\rm BP04}, \tag{10.12}$$

where $F_{\rm BP04}$ is the solar ν_e flux predicted by BP04 SSM. Due to the powerful background reduction by neutron tagging, this limit is about 20 times more stringent than the SK-I result [85]. However, our limit is less strict than KamLAND's. This is mainly because of our high analysis threshold.

---

[2] The KamLAND limit is 36 times the LMA model. However, the old flux for the LMA model is used in that calculation. The author of the LMA model increased the flux prediction by a factor of 2.56 due to the change in the star formation rate [109]. Therefore, the KamLAND limit corresponds to 14 times of the revised LMA prediction.

10.3.3 Model Independent $\bar{\nu}_e$ Flux Limit

Both searches of the supernova relic neutrino and the solar $\bar{\nu}_e$ described above are model dependent. We also calculate model independent upper limits for $\bar{\nu}_e$ flux with 1 MeV energy bins. Here we approximate the $\bar{\nu}_e$ energy by $E_{\bar{\nu}_e} \simeq E_{e^+} + 1.3$ MeV. The 90% C.L. upper limits on the number of events are calculated for each bin and the corresponding flux upper limits are computed by

$$\phi_{90} = \frac{N_{90}}{T \cdot N_p \cdot \bar{\sigma} \cdot \epsilon} \, \mathrm{cm}^{-2}\mathrm{s}^{-1}, \tag{10.13}$$

where T is the live time in seconds, N_p is the number of free protons, $\bar{\sigma}$ is the inverse beta decay cross section at the center of the energy bin and ϵ is the efficiency to detect both the primary signal and the delayed 2.2 MeV γ. Fig. 10.5 shows the upper limits for $\bar{\nu}_e$ energy in the 13.3 – 21.3 MeV range (e^+ energy 12 – 20 MeV). Results from SK-I and KamLAND are also shown for comparasions. SK-IV limits are almost two orders of magnitude better than SK-I owning to the powerful background reduction by neutron tagging. SK-IV limits are already comparable to (or better than) KamLAND's with only ∼40% of KamLAND's live time. We conclude that in the positron energy range of 12 – 20 MeV, SK is operating as a competitive $\bar{\nu}_e$ detector.

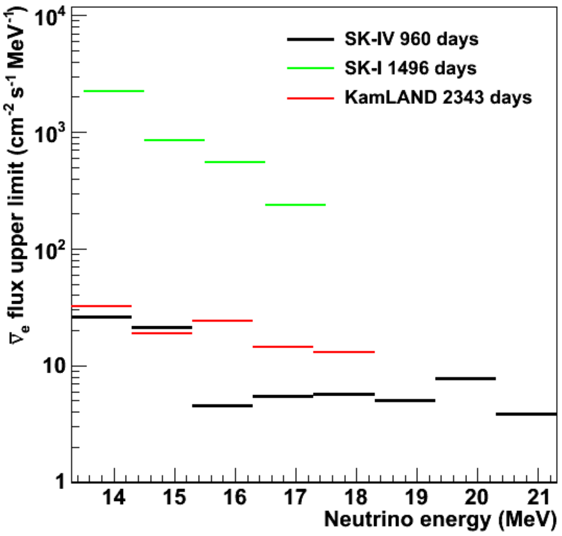

Figure 10.5: Model independent 90% C.L. upper limits on $\bar{\nu}_e$ flux from SK-IV (black line). Limits from SK-I (green line) and KamLAND (red line) are also shown for comparasions.

Chapter 11

Summary and Outlook

11.1 Summary

This thesis presents the first study of neutron tagging in a water Cherenkov detector and a search of low energy electron anti-neutrinos of extraterrestrial origin using this newly established technique.

Neutron Tagging in Pure Water

The 2.2 MeV γ released in neutron capture on free protons is previously unobservable at SK. A forced trigger scheme has been implemented at SK-IV to take 500 μs data after each primary trigger, covering ~92% of all neutron captures. The most challenging work is to extract the faint 2.2 MeV γ signal from the 500 μs data pack. A set of selection criteria are devised, yielding a 19.3% efficiency at 1%/500 μs accidental background level. The signal efficiency is derived from Monte Carlo, while the background probability is evaluated using real data.

An Am/Be neutron source is used to verify the delayed coincidence detection concept and the neutron tagging efficiency in SK. Distributions of the discriminating variables are compared between the Am/Be data and the Monte Carlo and good agreements are found in all cases. We have observed the exponential neutron capture time distribution with fitted lifetime $\tau = (203.7 \pm 2.8)\mu$s. The neutron tagging efficiency from Am/Be data is found to be in good agreement with Monte Carlo. Therefore, we conclude, for the first time, that neutrons can be observed in a large water Cherenkov detector.

Shortly after the start of SK-IV, neutrons produced in atmospheric neutrino interactions were observed for the first time in a water Cherenkov detector. As of this writing, a high statistics of neutron signal has been accumulated. This data sample is used to further validate the 2.2 MeV γ Monte Carlo and the neutron tagging data analysis. In addition, this observation provides the first data to study background reduction for proton decay searches using neutron tagging.

Study of Low Energy Electron Anti-neutrinos

A number of new physics topics can be studied at SK once the neutron tagging is in place. This thesis focuses on searching for supernova relic neutrinos and $\bar{\nu}_e$ from the Sun. Some other interesting topics worth investigation are outlined in section 11.2.1.

The supernova relic neutrinos are believed to lie just below SK's reach. Previously, SK's sensitivity is limited by the spallation products and the atmospheric neutrino backgrounds. The most promising way to improve SK's sensitivity is to use neutron tagging to identify $\bar{\nu}_e$. As the first attempt in this direction, we applied neutron tagging to search for $\bar{\nu}_e$'s in the energy range of 12–30 MeV. No appreciable signal events are observed. So we set upper limits on the flux for supernova relic neutrinos and solar $\bar{\nu}_e$. The 90% C.L. flux upper limit for SRN is about 6 times the model predictions. The 90% C.L. flux upper limit for solar $\bar{\nu}_e$ is 4.4×10^{-4} times the solar ν_e flux.

We also presented model independent upper limits on $\bar{\nu}_e$ flux for 13.3 MeV $< E_{\bar{\nu}_e} <$ 21.3 MeV, which provide the most sensitive result in the world.

In addition, neutron correlated low energy background for the SRN search has been intensively studied by means of a side band method, which enhances various background sources on purpose. By counting neutrons produced in μ-like events and isotropic events, we found the background level to the SRN search is higher than previously expected. The background can be better quantified with more upcoming SK-IV data. This will provide useful information for designing future experiments.

11.2 Outlook

Neutron tagging in water Cherenkov detectors is a relatively new idea. Work presented in this thesis is the first comprehensive study on this subject. Prospects of neutron tagging and its application to physics in water Cherenkov detectors are briefly outlined below.

11.2.1 SK-IV

Note that the predicted SRN event rate in the energy range of 12–30 MeV is only 4.15 events/22.5 kton · year. So the expected number of SRN events is ~ 5 after all reductions (including neutron tagging) for 10 years of operation of SK. On the other hand, the accidental background is about 38 for 10 years. If we consider the energy range of 14–30 MeV, the expected signal and accidental background are 4 and 6 events, respectively, for 10 years. There are also at least a few atmospheric neutrino background events. Therefore, in any case, it is unlikely to detect the supernova relic neutrino at SK with neutron tagging in pure water in near future.

Nevertheless, SK-IV provides the only available data for neutron tagging study in water Cherenkov detectors. The SK-IV data can be used but not restricted to study the following topics.

Background study for future SRN search

The background analysis presented in section 10.2 should be expanded when more data is available. A complete simulation of neutron production at SK is highly desirable. A good understanding of atmospheric neutrino background to the $\bar{\nu}_e$ signal is very important to the GADZOOKS! project (see section 11.2.2).

The cosmic ray muons can produce ^{9}Li. The β-n decay of ^{9}Li is an important background to the inverse beta decay reaction. The contamination of ^{9}Li below 12 MeV is no longer negligible. Little is known about the ^{9}Li yield at SK, because currently there is no existing data about ^{9}Li production in water. SK-IV data could provide useful information regarding ^{9}Li. If the ^{9}Li yield is large, it can be measured at SK. Otherwise, the ^{9}Li may be neglected for $\bar{\nu}_e$ analysis. A preliminary study has been carried out, where no evidence of ^{9}Li is found. It should be noted that the ^{9}Li yield in water is much smaller than in liquid scintillator [110].

Muon induced neutrons

Cosmic-ray muon induced neutrons have significant impact on underground low energy experiments. Accurate prediction of this background using Monte Carlo has not been achieved yet, see e.g. Ref. [111]. Currently all available data come from liquid scintillation detectors (see e.g. Ref. [110]) and significant discrepancies exists between data and Monte Carlo. It is possible to make a first measurement of muon induced neutrons in water at SK-IV.

Actually the muon induced neutrons have already been observed at SK-IV. There's no 500 μs data taken right after the muon event. However, the 500 μs data are taken after spallation events as long as the β decay electron has sufficient energy to issue the SHE trigger. If a spallation event happens close enough to the muon (< 1 ms), muon induced neutrons can be catched in the 500 μs data that follows the spallation events. Although muon induced neutrons can be observed in this way, its difficult to precisely calculate the neutron yield. It is necessary to change the trigger condition to take data right after the muon to cover all neutrons induced by muons. It is also needed to change the 2.2 MeV γ search method in order to identify all neutrons produced along the muon track.

Reactor $\bar{\nu}_e$

There are ~ 30 reactor $\bar{\nu}_e$'s interact at SK each day. In order to observe reactor $\bar{\nu}_e$, we need to push down the analysis threshold down to, say, 8 MeV. The accidental background will be much higher, but it is possible to see evidence of reactor neutrinos as long as there are a few hundreds reactor $\bar{\nu}_e$ events above 8 MeV each year. First observation of reactor $\bar{\nu}_e$ in a water Cherenkov detector will be certainly very interesting.

Atmospheric neutrinos

Although both high energy ν and $\bar{\nu}$ can create neutrons, there is some asymmetry between the neutron yield. Neutron tagging may help to divide the data into a ν-enhanced sample and an $\bar{\nu}$-enhanced sample to study the difference in the oscillations of neutrinos and anti-neutrinos.

Neutrons observed in the atmospheric neutrino data can be used to tune the neutron related part in the Monte Carlo. Once the neutron production in the Monte Carlo agrees with data, it can be used to predict how many backgrounds can be rejected by neutron tagging for the proton decay searches.

11.2.2 GADZOOKS!

Tagging neutrons by adding into SK 0.2% gadolinium compound (GADZOOKS! [75]) was proposed nearly a decade ago. The GADZOOKS! project is very attractive not only because the neutron tagging efficiency is ~ 4 times higher, but also because the accidental background probability is as low as 10^{-4} [77], allowing to lower the analysis threshold.

But before putting Gd into SK, several technical issues have to be settled. A dedicated prototype tank has been constructed at Kamioka Observatory for Evaluating Gadolinium's Action on Detector Systems (EGADS). Key issues being addressed include: effects of Gd on water transparency and detector components, how to dissolve and remove Gd, and how to modify the water circulation system to remove other impurities while keeping Gd in the detector. Based on the performance of EGADS, a decision on the future of GADZOOKS! will be made in the year of 2013.

If GADZOOKS! can be realized, SK will turn into a very effective giant $\bar{\nu}_e$ detector. All physics mentioned above can be better done in the Gd-loaded SK. In particular, first observation of the supernova relic neutrinos is highly expected.

Bibliography

[1] K. Hirata *et al.*, "Observation of a neutrino burst from the supernova SN1987A" *Phys. Rev. Lett.* **58** (1987) 1490–1493.

[2] R. M. Bionta *et al.*, "Observation of a neutrino burst in coincidence with supernova 1987A in the Large Magellanic Cloud" *Phys. Rev. Lett.* **58** (1987) 1494–1496.

[3] **Super-Kamiokande** Collaboration, Y. Fukuda *et al.*, "Evidence for oscillation of atmospheric neutrinos" *Phys. Rev. Lett.* (1998) 1562–1567.

[4] **Super-Kamiokande** Collaboration, S. Fukuda *et al.*, "Determination of solar neutrino oscillation parameters using 1496 days of Super-Kamiokande I data" *Phys.Lett.* **B539** (2002) 179–187, `arXiv:hep-ex/0205075`.

[5] **Super-Kamiokande** Collaboration, H. Nishino *et al.*, "Search for Proton Decay via $p \to e^+\pi^0$ and $p \to \mu^+\pi^0$ in a Large Water Cherenkov Detector" *Phys. Rev. Lett.* **102** no. 14, (2009) 141801.

[6] E. K. Akhmedov, "Neutrino physics" `arXiv:hep-ph/0001264`.

[7] C. Kraus *et al.*, "Final results from phase II of the Mainz neutrino mass search in tritium beta decay" *Eur.Phys.J.* **C40** (2005) 447–468, `arXiv:hep-ex/0412056`.

[8] K. Assamagan *et al.*, "Upper limit of the muon-neutrino mass and charged-pion mass from momentum analysis of a surface muon beam" *Phys. Rev. D* **53** (1996) 6065–6077.

[9] **ALEPH** Collaboration, R. Barate *et al.*, "An Upper limit on the tau-neutrino mass from three-prong and five-prong tau decays" *Eur.Phys.J.* **C2** (1998) 395–406.

[10] S. Hannestad, A. Mirizzi, G. G. Raffelt, and Y. Y. Wong, “Neutrino and axion hot dark matter bounds after WMAP-7” *JCAP* **1008** (2010) 001, `arXiv:1004.0695`.

[11] R. N. Mohapatra and P. B. Pal, *Massive Neutrinos in Physics and Astrophysics*, vol. 72 of *World Scientific Lecture Notes in Physics*. World Scientific Publishing Company, 3 ed., 2004.

[12] M. Fukugita and T. Yanagida, “Physics of neutrinos and applications to astrophysics”.

[13] C. Giunti and C. W. Kim, *Fundamentals of Neutrino Physics and Astrophysics*. Oxford University Press, 2007.

[14] M. Mohapatra *et al.*, “Theory of Neutrinos” `arXiv:hep-ph/0412099`.

[15] L. Wolfenstein, “Neutrino oscillations in matter” *Phys. Rev. D* **17** (1978) 2369–2374.

[16] S. Mikheev and A. Smirnov, “Resonance Amplification of Oscillations in Matter and Spectroscopy of Solar Neutrinos” *Sov.J.Nucl.Phys.* **42** (1985) 913–917.

[17] G. Fogli, E. Lisi, A. Marrone, A. Palazzo, and A. Rotunno, “Evidence of $\theta_{13} > 0$ from global neutrino data analysis” `arXiv:1106.6028`.

[18] T. Schwetz, M. Tortola, and J. Valle, “Where we are on θ_{13}: addendum to ’Global neutrino data and recent reactor fluxes: status of three-flavour oscillation parameters’” `arXiv:1108.1376`.

[19] **T2K** Collaboration, K. Abe *et al.*, “Indication of Electron Neutrino Appearance from an Accelerator-produced Off-axis Muon Neutrino Beam” *Phys.Rev.Lett.* **107** (2011) 041801, `arXiv:1106.2822`.

[20] **MINOS** Collaboration, P. Adamson *et al.*, “Improved search for muon-neutrino to electron-neutrino oscillations in MINOS” *Phys.Rev.Lett.* **107** (2011) 181802, `arXiv:1108.0015`.

[21] **DOUBLE-CHOOZ** Collaboration, Y. Abe *et al.*, “Indication for the disappearance of reactor electron antineutrinos in the Double Chooz experiment” `arXiv:1112.6353`.

[22] **DAYA-BAY** Collaboration, F. An *et al.*, “Observation of electron-antineutrino disappearance at Daya Bay” `arXiv:1203.1669`.

[23] B. Kayser, "Majorana neutrinos and their electromagnetic properties" *Phys. Rev. D* **26** (1982) 1662–1670.

[24] B. W. Lee and R. E. Shrock, "Natural suppression of symmetry violation in gauge theories: Muon- and electron-lepton-number nonconservation" *Phys. Rev. D* **16** (1977) 1444–1473.

[25] C. Giunti and A. Studenikin, "Neutrino electromagnetic properties" *Phys.Atom.Nucl.* **72** (2009) 2089–2125, `arXiv:0812.3646`.

[26] P. B. Pal and L. Wolfenstein, "Radiative decays of massive neutrinos" *Phys. Rev. D* **25** (1982) 766–773.

[27] J. E. Kim, "Neutrino magnetic moment" *Phys. Rev. D* **14** (1976) 3000–3002.

[28] M. A. B. Bég, W. J. Marciano, and M. Ruderman, "Properties of neutrinos in a class of gauge theories" *Phys. Rev. D* **17** (1978) 1395–1401.

[29] M. Czakon, J. Gluza, and M. Zrałek, "Neutrino magnetic moments in left-right symmetric models" *Phys. Rev. D* **59** (1998) 013010.

[30] M. Fukugita and T. Yanagida, "Particle-physics model for voloshin-vysotsky-okun solution to the solar-neutrino problem" *Phys. Rev. Lett.* **58** (1987) 1807–1809.

[31] N. F. Bell, "How Magnetic is the Neutrino?" *Int.J.Mod.Phys.* **A22** (2007) 4891–4899, `arXiv:0707.1556`.

[32] J. F. Beacom and P. Vogel, "Neutrino magnetic moments, flavor mixing, and the super-kamiokande solar data" *Phys. Rev. Lett.* **83** (1999) 5222–5225.

[33] A. Beda, V. Brudanin, V. Egorov, D. Medvedev, V. Pogosov, *et al.*, "Upper limit on the neutrino magnetic moment from three years of data from the GEMMA spectrometer" `arXiv:1005.2736`.

[34] G. G. Raffelt, "New bound on neutrino dipole moments from globular-cluster stars" *Phys. Rev. Lett.* **64** (1990) 2856–2858.

[35] G. Tammann, W. Loeffler, and A. Schroder, "The Galactic supernova rate" *Astrophys.J.Suppl.* **92** (1994) 487–493.

[36] R. Diehl *et al.*, "Radioactive Al-26 and massive stars in the galaxy" *Nature* **439** (2006) 45–47, `arXiv:astro-ph/0601015`.

[37] T. Padmanabhan, *Theoretical Astrophysics, Volume II: Stars and Stellar Systems.* Cambridge University Press, 2001.

[38] K. Kotake, K. Sato, and K. Takahashi, "Explosion mechanism, neutrino burst and gravitational wave in core-collapse supernovae" *Reports on Progress in Physics* **69** no. 4, (2006) 971–1143.

[39] H. A. Bethe, "Supernova mechanisms" *Rev. Mod. Phys.* **62** (1990) 801–866.

[40] G. Pagliaroli, F. Vissani, M. L. Costantini, and A. Ianni, "Improved analysis of SN 1987A antineutrino events" *Astrop. Phys.* **31** (2009) 163–176.

[41] T. Totani, K. Sato, H. E. Dalhed, and J. R. Wilson, "Future detection of supernova neutrino burst and explosion mechanism" *Astrophys. J.* **496** (1998) 216–225.

[42] M. T. Keil, G. G. Raffelt, and H.-T. Janka, "Monte carlo study of supernova neutrino spectra formation" *Astrophys. J.* **590** (2003) 971–991.

[43] K. Takahashi *et al.*, "Effects of neutrino oscillation on the supernova neutrino spectrum" *Phys. Rev. D* **64** (2001) 093004.

[44] M. Kaplinghat, G. Steigman, and T. P. Walker, "The supernova relic neutrino background" *Phys. Rev.* **D62** (2000) 043001, `arXiv:astro-ph/9912391`.

[45] H.-T. Janka and W. Hillebrandt, "Neutrino emission from type II supernovae: an analysis of the spectra" *Astro. Astrophys.* **224** (1989) 49–56.

[46] M. T. Keil, "Supernova neutrino spectra and applications to flavor oscillations" `arXiv:astro-ph/0308228`.

[47] J. F. Beacom, "The Diffuse Supernova Neutrino Background" *Ann. Rev. Nucl. Part. Sci.* **60** (2010) 439–462, `arXiv:1004.3311`.

[48] T. Totani and K. Sato, "Spectrum of the relic neutrino background from past supernovae and cosmological models" *Astropart. Phys.* **3** (1995) 367–376, `arXiv:astro-ph/9504015`.

[49] T. Totani, K. Sato, and Y. Yoshii, "Spectrum of the Supernova Relic Neutrino Background and Evolution of Galaxies" *Astrophys. J.* **460** (1996) 303–312, `arXiv:astro-ph/9509130`.

[50] R. A. Malaney, "Evolution of the cosmic gas and the relic supernova neutrino background" *Astropart. Phys.* **7** (1997) 125–136, `arXiv:astro-ph/9612012`.

[51] D. H. Hartmann and S. E. Woosley, "The cosmic supernova neutrino background" *Astropart. Phys.* **7** (1997) 137–146.

[52] L. E. Strigari, M. Kaplinghat, G. Steigman, and T. P. Walker, "The supernova relic neutrino backgrounds at KamLAND and Super-Kamiokande" *JCAP* **0403** (2004) 007, `arXiv:astro-ph/0312346`.

[53] S. Ando, K. Sato, and T. Totani, "Detectability of the supernova relic neutrinos and neutrino oscillation" *Astropart. Phys.* **18** (2003) 307–318, `arXiv:astro-ph/0202450`.

[54] S. Horiuchi, J. F. Beacom, and E. Dwek, "The Diffuse Supernova Neutrino Background is detectable in Super-Kamiokande" *Phys. Rev.* **D79** (2009) 083013, `arXiv:0812.3157`.

[55] M. Fukugita and M. Kawasaki, "Constraints on the star formation rate from supernova relic neutrino observations" *Mon.Not.Roy.Astron.Soc.* **340** (2003) L7, `arXiv:astro-ph/0204376`.

[56] C. Lunardini, "Diffuse neutrino flux from failed supernovae" *Phys.Rev.Lett.* **102** (2009) 231101, `arXiv:0901.0568`.

[57] S. Ando and K. Sato, "Relic neutrino background from cosmological supernovae" *New J.Phys.* **6** (2004) 170, `arXiv:astro-ph/0410061`.

[58] A. M. Hopkins and J. F. Beacom, "On the normalisation of the cosmic star formation history" *Astrophys.J.* **651** (2006) 142–154, `arXiv:astro-ph/0601463`.

[59] E. E. Salpeter, "The Luminosity function and stellar evolution" *Astrophys.J.* **121** (1955) 161–167.

[60] S. J. Smartt, "Progenitors of core-collapse supernovae" *Ann.Rev.Astron.Astrophys.* **47** (2009) 63–106, `arXiv:0908.0700`.

[61] A. Heger, C. Fryer, S. Woosley, N. Langer, and D. Hartmann, "How massive single stars end their life" *Astrophys.J.* **591** (2003) 288–300, `arXiv:astro-ph/0212469`.

[62] K. Takahashi, K. Sato, A. Burrows, and T. A. Thompson, "Supernova neutrinos, neutrino oscillations, and the mass of the progenitor star" *Phys. Rev. D* **68** (2003) 113009.

[63] A. S. Dighe and A. Y. Smirnov, "Identifying the neutrino mass spectrum from a supernova neutrino burst" *Phys. Rev. D* **62** (2000) 033007.

[64] S. Ando and K. Sato, "Supernova relic neutrinos and observational implications for neutrino oscillation" *Phys.Lett.* **B559** (2003) 113, `arXiv:astro-ph/0210502`.

[65] B. Dasgupta and A. Dighe, "Collective three-flavor oscillations of supernova neutrinos" *Phys. Rev. D* **77** (2008) 113002.

[66] B. Dasgupta, A. Dighe, G. G. Raffelt, and A. Y. Smirnov, "Multiple spectral splits of supernova neutrinos" *Phys. Rev. Lett.* **103** (2009) 051105.

[67] J. N. Bahcall and M. H. Pinsonneault, "What do we (not) know theoretically about solar neutrino fluxes?" *Phys. Rev. Lett.* **92** (2004) 121301.

[68] J. N. Bahcall, A. M. Serenelli, and S. Basu, "New solar opacities, abundances, helioseismology, and neutrino fluxes" *Astrophys.J.* **621** (2005) L85–L88, `arXiv:astro-ph/0412440`.

[69] **Borexino** Collaboration, G. Bellini *et al.*, "First evidence of *pep* solar neutrinos by direct detection in borexino" *Phys. Rev. Lett.* **108** (2012) 051302.

[70] L. Okun, M. Voloshin, and M. Vysotsky, "Neutrino Electrodynamics and Possible Effects for Solar Neutrinos" *Sov.Phys.JETP* **64** (1986) 446–452.

[71] J. Schechter and J. W. F. Valle, "Majorana neutrinos and magnetic fields" *Phys. Rev. D* **24** (1981) 1883–1889.

[72] J. Schechter and J. W. F. Valle, "Erratum: Majorana neutrinos and magnetic fields" *Phys. Rev. D* **25** (1982) 283–283.

[73] C.-S. Lim and W. J. Marciano, "Resonant spin-flavor precession of solar and supernova neutrinos" *Phys. Rev. D* **37** (1988) 1368–1373.

[74] E. K. Akhmedov and J. Pulido, "Solar neutrino oscillations and bounds on neutrino magnetic moment and solar magnetic field" *Phys.Lett.* **B553** (2003) 7–17, `arXiv:hep-ph/0209192`.

[75] J. F. Beacom and M. R. Vagins, "Antineutrino spectroscopy with large water Čerenkov detectors" *Phys. Rev. Lett.* **93** (2004) 171101.

[76] S.-M. Chen and Z. Deng, "A proposal for detecting supernova relic neutrino in Super Kamiokande" *Nucl.Phys.Proc.Suppl.* **166** (2007) 252–254.

[77] **Super-Kamiokande** Collaboration, H. Watanabe *et al.*, "First study of neutron tagging with a water Cherenkov detector" *Astrop. Phys.* **31** no. 4, (2009) 320–328.

[78] G. Fogli, E. Lisi, A. Mirizzi, and D. Montanino, "Probing supernova shock waves and neutrino flavor transitions in next-generation water-Cerenkov detectors" *JCAP* **0504** (2005) 002, `arXiv:hep-ph/0412046`.

[79] **KamLAND** Collaboration, A. Gando *et al.*, "A study of extraterrestrial antineutrino sources with the KamLAND detector" `arXiv:1105.3516`.

[80] **SNO** Collaboration, B. Aharmim *et al.*, "Electron antineutrino search at the Sudbury Neutrino Observatory" *Phys.Rev.* **D70** (2004) 093014, `arXiv:hep-ex/0407029`.

[81] **SNO** Collaboration, B. Aharmim *et al.*, "A Search for Neutrinos from the Solar hep Reaction and the Diffuse Supernova Neutrino Background with the Sudbury Neutrino Observatory" *Astrophys.J.* **653** (2006) 1545–1551, `arXiv:hep-ex/0607010`.

[82] **Borexino** Collaboration, G. Bellini *et al.*, "Study of solar and other unknown anti-neutrino fluxes with Borexino at LNGS" *Phys.Lett.* **B696** (2011) 191–196, `arXiv:1010.0029`.

[83] **Super-Kamiokande** Collaboration, M. Malek *et al.*, "Search for supernova relic neutrinos at SUPER-KAMIOKANDE" *Phys.Rev.Lett.* **90** (2003) 061101, `arXiv:hep-ex/0209028`.

[84] **Super-Kamiokande** Collaboration, K. Bays *et al.*, "Supernova relic neutrino search at super-kamiokande" *Phys. Rev. D* **85** (2012) 052007.

[85] **Super-Kamiokande** Collaboration, Y. Gando *et al.*, "Search for anti-nu(e) from the sun at Super-Kamiokande I" *Phys.Rev.Lett.* **90** (2003) 171302, `arXiv:hep-ex/0212067`.

[86] A. Suzuki *et al.*, "Improvement of 20 in. diameter photomultiplier tubes" *Nucl. Instrum. Meth. A* **329** (1993) 299–313.

[87] S. Yamada *et al.*, "Commissioning of the new electronics and online system for the super-kamiokande experiment" *Nuclear Science, IEEE Transactions on* **57** (2010) 428–432.

[88] H. Nishino *et al.*, "High-speed charge-to-time converter ASIC for the Super-Kamiokande detector" *Nucl.Instrum.Meth.A* **610** (2009) 710–717.

[89] *ATM-3 (ATLAS Muon TDC Version 3) User's Manual.*

[90] **Super-Kamiokande** Collaboration, S. Fukuda *et al.*, "The super-kamiokande detector" *Nucl. Instrum. Meth. A* **501** no. 2-3, (2003) 418–462.

[91] **Super-Kamiokande** Collaboration, M. Nakahata *et al.*, "Calibration of Super-Kamiokande using an electron LINAC" *Nucl.Instrum.Meth.A* **421** (1999) 113–129.

[92] **Super-Kamiokande** Collaboration, E. Blaufuss *et al.*, "^{16}N as a calibration source for Super-Kamiokande" *Nucl. Instrum. Meth. A* **458** (2001) 638–649.

[93] M. Smy, "Low Energy Event Reconstruction and Selection in Super-Kamiokande-III" in *Proceedings of the 30th ICRC*, vol. 5, p. 1279. 2007.

[94] Z. Conner, *A Study of Solar Neutrinos using the Super-Kamiokande Detector.* PhD thesis, University of Maryland, 1997.

[95] S. Desai, *High energy neutrino astrophysics with Super-Kamiokande.* PhD thesis, Boston University, 2004.

[96] K. Bays, *Search for the Diffuse Supernova Neutrino Background at Super-Kamiokande.* PhD thesis, University of California, Irvine, 2011.

[97] M. Malek, *A Search for Supernova Relic Neutrinos*. PhD thesis, State University of New York at Stony Brook, 2003.

[98] M. Ikeda, *Precise Measurement of Solar Neutrinos with Super-Kamiokande III*. PhD thesis, University of Tokyo, 2009.

[99] A. Strumia and F. Vissani, "Precise quasielastic neutrino/nucleon cross-section" *Physics Letters B* **564** no. 1-2, (2003) 42 – 54.

[100] P. Vogel and J. F. Beacom, "Angular distribution of neutron inverse beta decay, $\overline{\nu}_e + p \rightarrow e^+ + n$" *Phys. Rev. D* **60** (1999) 053003.

[101] W. T. Winter, S. J. Freedman, K. E. Rehm, and J. P. Schiffer, "The ^{8}B neutrino spectrum" *Phys. Rev. C* **73** (2006) 025503.

[102] **Super-Kamiokande** Collaboration, J. Hosaka *et al.*, "Solar neutrino measurements in Super-Kamiokande-I" *Phys. Rev. D* **73** no. 11, (2006) 112001.

[103] P. Speckmayer, A. Hcker, J. Stelzer, and H. Voss, "The toolkit for multivariate data analysis, TMVA 4" *J.Phys.: Conf. Ser.* **219** no. 3, (2010) 032057.

[104] R. W. Stooksberry and M. F. Crouch, "Neutron-proton capture cross section" *Phys. Rev.* **114** no. 6, (1959) 1561 – 1563.

[105] **Super-Kamiokande** Collaboration, Y. Ashie *et al.*, "Measurement of atmospheric neutrino oscillation parameters by Super-Kamiokande I" *Phys. Rev. D* **71** no. 11, (2005) 112005.

[106] M. Shiozawa, *Search for Proton Decay via $p \rightarrow e^+\pi^0$ in a Large Water Cherenkov Detector*. PhD thesis, University of Tokyo, 1999.

[107] W. A. Rolke, A. M. Lpez, and J. Conrad, "Limits and confidence intervals in the presence of nuisance parameters" *Nucl.Instrum.Meth.A* **551** no. 23, (2005) 493 – 503.

[108] http://root.cern.ch.

[109] S. Ando. talk at NNN05, France, 2005.

[110] **KamLAND Collaboration** Collaboration, S. Abe *et al.*, "Production of radioactive isotopes through cosmic muon spallation in kamland" *Phys. Rev. C* **81** (2010) 025807.

[111] Y.-F. Wang, V. Balic, G. Gratta, A. Fassò, S. Roesler, and A. Ferrari, "Predicting neutron production from cosmic-ray muons" *Phys. Rev. D* **64** (2001) 013012.